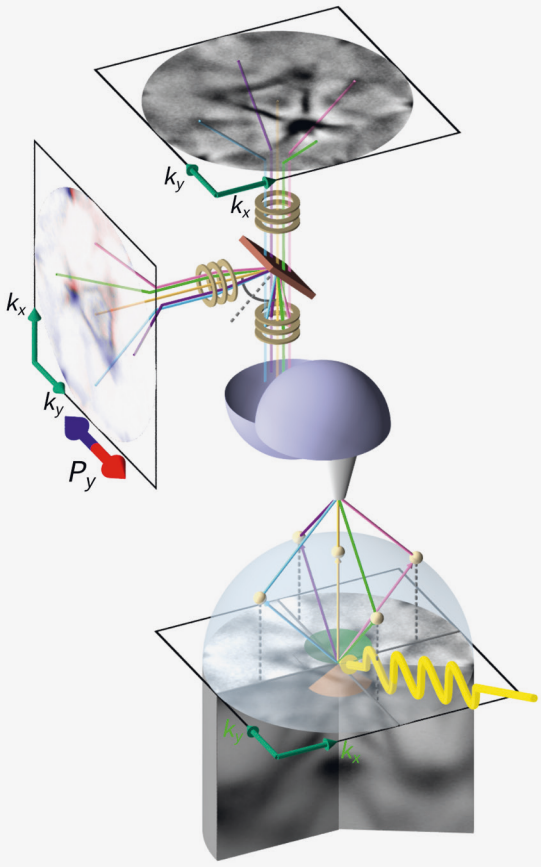

Spin- and orbital-dependent band structure of unconventional topological semimetals

Kenta Hagiwara

Schlüsseltechnologien / Key Technologies
Band / Volume 270
ISBN 978-3-95806-701-1

Mitglied der Helmholtz-Gemeinschaft

JÜLICH
Forschungszentrum

Schriften des Forschungszentrums Jülich
Reihe Schlüsseltechnologien / Key Technologies Band / Volume 270

Forschungszentrum Jülich GmbH
Peter Grünberg Institut (PGI)
Elektronische Eigenschaften (PGI-6)

Spin- and orbital-dependent band structure of unconventional topological semimetals

Kenta Hagiwara

Schriften des Forschungszentrums Jülich
Reihe Schlüsseltechnologien / Key Technologies Band / Volume 270

ISSN 1866-1807 ISBN 978-3-95806-701-1

Bibliografische Information der Deutschen Nationalbibliothek.
Die Deutsche Nationalbibliothek verzeichnet diese Publikation in der
Deutschen Nationalbibliografie; detaillierte Bibliografische Daten
sind im Internet über http://dnb.d-nb.de abrufbar.

Herausgeber und Vertrieb:	Forschungszentrum Jülich GmbH Zentralbibliothek, Verlag 52425 Jülich Tel.: +49 2461 61-5368 Fax: +49 2461 61-6103 zb-publikation@fz-juelich.de www.fz-juelich.de/zb
Umschlaggestaltung:	Grafische Medien, Forschungszentrum Jülich GmbH
Druck:	Grafische Medien, Forschungszentrum Jülich GmbH
Copyright:	Forschungszentrum Jülich 2023

Schriften des Forschungszentrums Jülich
Reihe Schlüsseltechnologien / Key Technologies, Band / Volume 270

D 464 (Diss. Duisburg-Essen, Univ., 2022)

ISSN 1866-1807
ISBN 978-3-95806-701-1

Vollständig frei verfügbar über das Publikationsportal des Forschungszentrums Jülich (JuSER)
unter www.fz-juelich.de/zb/openaccess.

Contents

Kurzzusammenfassung

Topologische Semimetalle zeichnen sich durch Fermion-Quasiteilchen mit Bandkreuzungspunkten in ihrer elektronischen Struktur aus. In Weyl Semimetallen sind diese Kreuzungspunkte durch Symmetrie und Topologie geschützt. Hier werden Fermi-Arc Oberflächenzustände gebildet, die Paare dieser Punkte mit entgegengesetzten chiralen Ladungen verbinden. In jüngster Vergangenheit sind unkonventionelle topologische Semimetalle mit im E-k-Raum stark verkippten Dirac-Zuständen, sogenannte Typ-II Dirac/Weyl-Semimetalle, aufgekommen. Außerdem können höhere topologische Ladungen in chiralen topologischen Semimetallen gebildet werden. Trotz solcher neuartigen Materialien sind die Spin-Textur und ihre Verbindung zu topologischen Eigenschaften sogar in konventionellen topologischen Semimetallen noch immer wenig ergründet. In dieser Dissertation haben wir das Typ-II Dirac Semimetall $NiTe_2$, das Typ-II Weyl Semimetall $MoTe_2$ und das chirale topologische Semimetall CoSi untersucht. Je niedriger hierbei die Kristallsymmetrie ist, umso höhere topologische Ladungen können gebildet werden. Die Inversionssymmetrie von $NiTe_2$ führt zu einer entarteten topologischen Ladung $C = 0$. Dagegen bewirkt die gebrochene Inversionssymmetrie in $MoTe_2$ eine Aufspaltung der topologischen Ladungen mit $C = \pm 1$ und chiral strukturiertes CoSi wird durch $C = \pm 2$ charakterisiert. Mittels Impulsmikroskopie zusammen mit einem bildgebenden Spinfilter haben wir Spin- und Orbital-abhängige elektronische Strukturen in Verbindung mit Symmetrie und Topologie untersucht.

Für inversionssymmetrische Materialien wie $NiTe_2$ ist eine Spin-Polarisation der Volumenzustände nicht erlaubt. Dennoch kann eine "versteckte" Spin-Polarisation der Volumen Dirac-Zustände der obersten Te-Lage einer Te-Ni-Te-Dreifachschicht beobachtet werden, wobei der entartete Dirac-Zustand in $NiTe_2$ durch eine Überlagerung von zwei Dirac-Zuständen mit entgegengesetzter Spin-Polarisation gebildet wird. Dieses Szenario finden wir sowohl für $NiTe_2$ als auch für $MoTe_2$: In beiden Fällen weist ein Paar Weyl-Zustände mit entgegengesetzter Chiralität eine umgekehrte Spin-Polarisation auf. Abhängig von der Symmetrie der jeweiligen Kristallstruktur sind die Zustände jedoch im k-Raum im Fall von inversionssymmetrischem $NiTe_2$ entartet und im Fall von $MoTe_2$, aufgrund der gebrochenen Inversionssymmetrie separiert. Dabei konnten wir zeigen, dass ein ausgeprägter Circulardichroismus mit wechselndem Vorzeichen einen Fingerabdruck für die entgegengesetzten chiralen Ladungen der Weyl-Punkte in $MoTe_2$ liefert. Die Empfindlichkeit des Circulardichroismus gegenüber der Chiralität des Systems kann darüberhinaus direkt anhand von CoSi bestätigt werden, wo der Dichroismus sein Vorzeichen zwischen chiralen Kristallen mit entgegengesetzter struktureller Händigkeit umkehrt. Der Circulardichroismus offenbarte außerdem eine komplexe Orbital-Textur der CoSi Bänder, welche ein höher geladenes Fermion mit nicht-trivialer Topologie bilden.

In dieser Arbeit haben wir eine Beziehung zwischen Spin- und Orbital-Textur, Topologie und Symmetrie aufgebaut. Über die drei hier untersuchten Materialien hinaus tragen die in dieser Arbeit dargestellten Ergebnisse erheblich zum Verständnis von unkonventionellen topologischen Semimetallen im Allgemeinen bei.

Abstract

Topological semimetals host fermion quasiparticles with band crossing points in their bulk electronic structures. In Weyl semimetals, these crossing points are protected by symmetry and topology, forming a Fermi arc at the surface, which connects pairs of these points with opposite chiral charges. Recently, unconventional topological semimetals have emerged with strongly tilted Dirac cones, termed type-II Dirac/Weyl semimetals. Additionally, higher topological charges can be formed in structurally chiral crystals, referred to as chiral topological semimetals. In spite of the emergence of such new materials, the underlying spin texture and its link to topological properties even in conventional topological semimetals have still remained elusive. In this thesis, we studied the type-II Dirac semimetal $NiTe_2$, the type-II Weyl semimetal $MoTe_2$, and the chiral topological semimetal CoSi. Here, when the symmetries of the respective crystal structures are lower, a higher topological charge can be formed. Inversion-symmetric $NiTe_2$ leads to a degenerate topological charge $C = 0$, while broken inversion symmetry in $MoTe_2$ causes the splitting of topological charges with $C = \pm 1$. Chiral structured CoSi is characterized by $C = \pm 2$. By means of momentum microscopy together with an imaging spin filter, we revealed spin- and orbital-dependent electronic structures in connection with symmetry and topology.

For inversion-symmetric materials like $NiTe_2$, a spin polarization of bulk states is not allowed. An observed "hidden" spin polarization of the bulk Dirac cone, however, originates from the top Te atom of a Te-Ni-Te trilayer. This can be understood in a concept where the degenerate Dirac cone in $NiTe_2$ is formed by a superposition of two Dirac cones with opposite spin polarizations localized at the top and bottom Te atoms of the trilayer. In particular, we found the same scenario for $NiTe_2$ and $MoTe_2$: a pair of Weyl cones with opposite chirality exhibits a reversed spin polarization. Depending on the symmetry of the crystal structure, however, the cones are degenerate in k space for inversion-symmetric $NiTe_2$ and separated for $MoTe_2$ due to broken inversion symmetry. A strong circular dichroism with reversed sign gives a fingerprint of opposite chiral charges of the Weyl points in $MoTe_2$. The sensitivity of the circular dichroism to the chirality of the system can be directly confirmed in the case of CoSi, where the dichroism reverses its sign between chiral crystals of the opposite structural handedness. The circular dichroism further revealed a different orbital texture of bands forming a higher-charge fermion in CoSi, which is attributed to their topology.

In this thesis, we established a relationship between the spin and orbital texture, topology, and symmetry. Beyond the three studied materials, the results presented in this thesis significantly contribute to the understanding of unconventional topological semimetals, in general.

1 Introduction

Dirac and Weyl fermions are fundamental particles described by relativistic quantum mechanics [1, 2]. Weyl fermions attain chirality determined by whether the directions of its spin and momentum are parallel or antiparallel, while Dirac fermions can be regarded as a superposition of a pair of Weyl fermions with opposite chirality. Though these fermions have been first predicted in high-energy physics, the signature of Weyl fermions has still not been captured in high-energy physics, whereas Dirac and Weyl fermions in condensed-matter systems have been discovered as quasiparticle excitations. The discovery of their analogues in solids has attracted great attention not only because the characterization of such fermions encountered a non-trivial topology of their band structure but also because it promises to revolutionize spintronics applications and quantum computing processing by virtue of novel quantum phenomena [3, 4]. These movements dramatically boosted the current importance of the field "topological quantum materials" in condensed-matter physics and materials science.

Dirac fermions in solids can be considered to be massless relativistic electrons described by the Dirac equation. Since the band dispersion within the electronic structure is a direct manifestation of energy eigenstates, these fermions emerge as a linear dispersion with band crossing points in the electronic structure, a so-called Dirac cone. Angle-resolved photoemission spectroscopy (ARPES) provides information of electronic structures, which has been employed for verification of topological quantum materials by observing their band structures, including Dirac cones. In general, the band structure describes the motion of electrons in a solid. Thus it is directly related to the electric transport properties of a material. For instance, graphene or topological insulators possessing Dirac cones in their electronic structures host high-speed quasiparticle states and a conductive metallic surface.

Topological quantum materials are classified according to the topology of their band structure, which is characterized by a topological invariant, e.g., the Chern number [5]. For instance, the opposite chirality of Weyl fermions in the electronic structure is encoded by a positive and negative sign of the Chern number of the band crossing points, which is also called "topological chiral charge" [4]. It is important to note that the topological invariant is related to the "phase" of the wave function and can be calculated form the bulk wave function. If a non-trivial topological order is present in the bulk with a non-zero Chern number, topologically protected surface states should be formed as a result of the bulk-boundary correspondence. Symmetries also play a crucial role to realize topological quantum materials. Their band crossing points are protected by crystal- or time-reversal-symmetries. In other words, when certain symmetries are broken, global properties of topological quantum materials change drastically.

This thesis goes far beyond topological materials classification based on the band structure. Indeed, topological information including topological chiral charges can be more directly reflected by the spin and orbital degrees of freedom of the electronic states. In general, spin-orbit coupling links the spin and orbital angular momentum. Recently, momentum microscopy combined with an imaging spin filter has overcome the low efficiency of spin-resolved measurements by simultaneously recording the electron spin in 2D (k_x, k_y) momentum space [6, 7]. By utilizing differently polarized light, one can access the orbital information of the electronic wave function. Especially, circularly-polarized light, which possesses a specific chirality itself, interacts with structural and electronic chirality [8]. Our motivation is to clarify the relationship between topological chiral charge, spin- and orbital-texture, and symmetry from the electronic-structure point of view.

In this thesis, we study the type-II Dirac semimetal $NiTe_2$, the type-II Weyl semimetal $MoTe_2$ [9], and the topological chiral semimetal CoSi [10]. Depending on the crystal structure, different topological phases, encoded by the Chern number, emerge in these materials. When more crystal symmetries are broken, a larger topological charge can be realized. Space-inversion protected $NiTe_2$ possesses $C = 0$, space-inversion broken $MoTe_2$ $C = \pm 1$, and chiral-structured CoSi $C = \pm 2$ (or ± 4). A chiral structure has no space-inversion and mirror symmetry. This leads to a concept "handedness" that an object does not coincide with its mirror image. Moreover, these materials belong to a class of "unconventional" topological semimetals, where unconventional fermions emerge which have no analogs in high-energy physics [11, 12]. This is because

	$NiTe_2$	$1T_d$-$MoTe_2$	CoSi
	Type-II Dirac semimetal	Type-II Weyl semimetal	Chiral topological semimetal
Crystal structure	Preserved space-inversion symmetry	Broken space-inversion symmetry	Chiral
Chern number	0	±1	±2 (±4)
Band structure	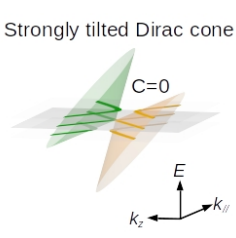	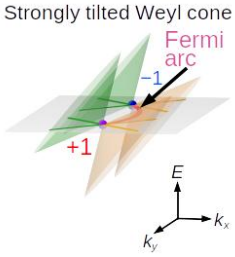	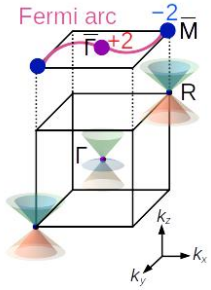

Table 1.1: Unconventional topological semimetals studied in this thesis.

fermions in condensed-matter systems are constrained by the symmetries of the crystal space group. These symmetries can be much lower than the Poincare symmetry imposed in high-energy physics, which may give rise to abundant fermions beyond conventional Dirac and Weyl fermions in solids. These unconventional topological semimetals attract great attention also because they have potential to exhibit more exotic quantum phenomena. We demonstrate that our findings for each material can be explained by unified concepts, which can be generally applied to other topological quantum materials.

In Section 2.1, we first introduce Dirac and Weyl fermions, and spin-orbit coupling based on the Dirac equation in relativistic quantum mechanics. Spin-orbit coupling plays important roles not only for realization of topological quantum materials but also for electron spin detection. In Section 2.2, we describe a general concept to classify topological quantum materials including the topological invariant for band structures, i.e., the Chern number, and a guideline for the formation of topological surface states, i.e., the bulk-boundary correspondence. We then describe topological insulators, Dirac and Weyl semimetals, and chiral topological semimetals in Secs. 2.3, 2.4, and 2.5, respectively.

In Chapter 3, we describe the experimental method employed in our work starting from the principles of photoemission spectroscopy and electron spin detection to spin-resolved momentum microscopy. Section 3.4 emphasizes how polarization-dependent measurements probe the orbital information of the wave functions and reviews their applications to topological quantum materials with regard to the spin and orbital degrees of freedom of the electron in topologically non-trivial band structures.

In Chapter 4, we visualize the 3D Fermi surface of the type-II Dirac semimetal $NiTe_2$ obtained by photon-energy dependent measurements. By performing spin-resolved momentum microscopy, we then unveil the intriguing spin texture of the surface and bulk Dirac cones. An observed "hidden" spin texture of the bulk states is, however, not expected due to the crystal symmetry of $NiTe_2$.

In Chapter 5, we reveal symmetry properties of measured band structure of the type-II Weyl semimetal $MoTe_2$, taking two different experimental geometries as examples. We probed the chiral electronic structure by means of circular dichroism and captured the chirality of the Weyl points. For the first time, we experimentally uncovered the spin texture of Weyl cones in $MoTe_2$.

In Chapter 6, we elaborate how we prepared and characterised high quality surfaces of the chiral topological semimetal CoSi. We then clarify dichroism and orbital contribution in the band structure by means of polarization-dependent measurements.

In Chapter 7, with the help of thin film band structure calculations and general symmetry arguments, we connect important results that we have obtained for these materials and describe unified concepts of the relationship between spin- and orbital-dependent band structures, symmetry, and topological chiral charges. Finally, in Chapter 8, we summarize our conclusion and give a future outlook.

2 Background

In this chapter, we introduce the basic background of topological quantum materials. We start with Dirac and Weyl fermions, and spin-orbit coupling based on the Dirac equation in relativistic quantum mechanics in Sec. 2.1. Spin-orbit coupling plays important roles not only for realization of topological quantum materials but also for electron spin detection. Dirac fermions appear as quasiparticles in topological quantum materials. Followed by an overview and a general concept for the classification of topological quantum materials in Sec. 2.2, we describe topological insulators, Dirac and Weyl semimetals, and chiral topological semimetals in Secs. 2.3, 2.4, and 2.5, respectively.

2.1 Relativistic quantum mechanics

2.1.1 Dirac and Weyl fermions

Dirac established a theory describing spin-$\frac{1}{2}$ particles in the relativistic regime [1]. We start from the relativistic energy law:

$$E^2 = c^2\boldsymbol{p}^2 + m^2c^4, \tag{2.1}$$

where E is the energy, c is the speed of light, $\boldsymbol{p}$ is the momentum, m is the rest mass. We replace $E \to i\hbar\frac{\partial}{\partial t}$ and $\boldsymbol{p} \to -i\hbar\left(\frac{\partial}{\partial x_1}, \frac{\partial}{\partial x_2}, \frac{\partial}{\partial x_3}\right)$ to change from a classical description to a quantum mechanical description. We linearize this equation with respect to the energy E and the momentum $\boldsymbol{p}$ by introducing matrix coefficients such that the equation fulfills the Lorentz invariance and we obtain the Dirac equation:

$$\left[i\hbar\frac{\partial}{\partial t} + i\hbar c\left(\gamma^1\frac{\partial}{\partial x_1} + \gamma^2\frac{\partial}{\partial x_2} + \gamma^3\frac{\partial}{\partial x_3}\right) - \gamma^0 mc^2\right]\psi = 0, \tag{2.2}$$

where ψ is a four-component wave function, γ^μ $(\mu = 0, 1, 2, 3)$ is a 4×4 matrix fulfilling the anticommutation relation $\{\gamma^\mu, \gamma^\nu\} = 2\delta_{i,j}I$ $(\mu, \nu = 0, 1, 2, 3)$, I is the 4×4 identity matrix. One can chose a set of γ^μ matrices called Dirac representation:

$$\gamma^0 = \begin{pmatrix} I & 0 \\ 0 & -I \end{pmatrix}, \gamma^j = \begin{pmatrix} 0 & \sigma^j \\ -\sigma^j & 0 \end{pmatrix} (j = 1, 2, 3), \tag{2.3}$$

where $\sigma^1 = \begin{pmatrix} 0 & 1 \\ 1 & 0 \end{pmatrix}, \sigma^2 = \begin{pmatrix} 0 & -i \\ i & 0 \end{pmatrix}, \sigma^3 = \begin{pmatrix} 1 & 0 \\ 0 & -1 \end{pmatrix}$ are Pauli matrices. One can choose another set of γ^μ matrices called chiral representation or Weyl representation [2]:

$$\gamma^0 = \begin{pmatrix} 0 & I \\ I & 0 \end{pmatrix}, \gamma^j = \begin{pmatrix} 0 & -\sigma^j \\ \sigma^j & 0 \end{pmatrix} (j = 1, 2, 3). \tag{2.4}$$

In the Weyl representation, the Dirac spinor ψ can be decomposed into a right-handed chiral spinor ψ_R and a left-handed chiral spinor ψ_L fulfilling the following equation:

$$\psi = \psi_R + \psi_L \tag{2.5}$$
$$\gamma^5 \psi_R = +\psi_R \tag{2.6}$$
$$\gamma^5 \psi_L = -\psi_L \tag{2.7}$$

$$i\hbar c\left(\gamma^1 \frac{\partial}{\partial x_1} + \gamma^2 \frac{\partial}{\partial x_2} + \gamma^3 \frac{\partial}{\partial x_3}\right)\psi_R = mc^2 \psi_L \tag{2.8}$$
$$i\hbar c\left(\gamma^1 \frac{\partial}{\partial x_1} + \gamma^2 \frac{\partial}{\partial x_2} + \gamma^3 \frac{\partial}{\partial x_3}\right)\psi_L = mc^2 \psi_R, \tag{2.9}$$

where the operator $\gamma^5 = i\gamma^0\gamma^1\gamma^2\gamma^3$ gives the eigenvalue reflecting the chirality of the chiral spinor. A Weyl fermion is described by ψ_R or ψ_L and attains chirality, while a Dirac fermion is a particle satisfying eq. 2.2 and is regarded as a superposition of a pair of fermions with opposite chirality described by eq. 2.5. If $m = 0$, ψ_R and ψ_L are decoupled. The chirality of a massless particle is defined by whether the directions of its spin and momentum are parallel or antiparallel.

In solids, a massless Dirac fermion manifests as a linear dispersion so-called Dirac cone in energy-momentum space, which seems to follow $m = 0$ in eqs. 2.1 and 2.2: $E = \pm cp$, in sharp contrast to a nearly free quasiparticles described by Schrödinger equation $\mathcal{H} = \frac{p^2}{2m}$ so-called Schrödinger particle. Analogous to high-energy physics, Weyl cones always appear in pairs and attains defined chirality.

2.1.2 Spin-orbit coupling

One of the successes in the Dirac equation is the introduction of the electron spin and spin-orbit coupling (SOC). The origin of the SOC is interaction between an electron spin and a "virtual" magnetic field caused by the electron motion in the electric field. Imagine the electron orbiting around the atomic nucleus. When one looks from the moving coordinate system of the electron, the nucleus seems to orbit around the electron and it causes the "virtual" magnetic field for the electron as the effect of electromagnetic induction. From the relativistic point of view, this means the electric field is transformed into a magnetic field by the Lorentz transformation.

We consider the Dirac equation in the electromagnetic field. We replace $\boldsymbol{p} \to \boldsymbol{p} - \frac{e}{c}\boldsymbol{A}$ and $E \to E - e\phi$ in eqs. 2.1 and 2.2, where $\boldsymbol{A}$ is the vector potential, ϕ is the electric potential, and e is the electric charge:

$$\mathcal{H}\psi = E\psi, \ \mathcal{H} = \frac{1}{2m}\left(\boldsymbol{p} - \frac{e}{c}\boldsymbol{A}\right)^2 + e\phi. \tag{2.10}$$

In the non-relativistic limit, $E, e\psi \ll mc^2$, and introducing the energy $W = E - mc^2$ excluding the rest energy mc^2, we obtain:

$$\left[\frac{1}{2m}\left(\boldsymbol{p} - \frac{e}{c}\boldsymbol{A}\right)^2 + e\phi - \frac{e\hbar}{2mc}\sigma\cdot\boldsymbol{B} - \frac{e\hbar^2}{8mc^2}\nabla\cdot\boldsymbol{E} - \frac{e\hbar}{4m^2c^2}\sigma\left[\boldsymbol{E}\times\left(\boldsymbol{p} - \frac{e}{c}\boldsymbol{A}\right)\right]\right]\psi = W\psi, \tag{2.11}$$

where $\boldsymbol{E}$ is the electric field and $\boldsymbol{B}$ is the magnetic field. The first two terms are the same as the Schrödinger equation for a particle in the electromagnetic field. The third term $\frac{e\hbar}{2mc}\sigma \cdot \boldsymbol{B} = \frac{2\mu_B}{\hbar}\boldsymbol{S} \cdot \boldsymbol{B}$ ($\mu_B = \frac{e\hbar}{2mc}$: Bohr magneton) represents the interaction energy of the electron spin with the magnetic moment $-\frac{2\mu_B}{\hbar}\boldsymbol{S}$ and an external magnetic field. The forth term, Darwin term, may be understood as a relativistic correction to the electron energy and has no classical analogon. The fifth term, assuming $\boldsymbol{A} = 0$, becomes

$$\mathcal{H}_{\mathrm{SOC}} = \frac{e\hbar}{4m^2c^2}\sigma\,(\boldsymbol{E} \times \boldsymbol{p}) = \frac{e}{2m^2c^2r}\frac{d\phi}{dr}(\boldsymbol{L} \cdot \boldsymbol{S}) \tag{2.12}$$

by applying $\boldsymbol{E} = -\boldsymbol{r}(\frac{1}{r})\frac{d\phi}{dr}$, $\boldsymbol{S} = \frac{\hbar}{2}\sigma$, and $\boldsymbol{L} = \boldsymbol{r} \times \boldsymbol{p}$, which describes the SOC energy.

2.2 Classification of topological quantum materials

2.2.1 Overview

Topological quantum materials host quasiparticles as band crossing points with linear dispersions in their surface (topological insulators [3, 13]) or bulk (Dirac semimetals and Weyl semimetals [4, 14, 15]) electronic structures, so-called Dirac cones. These band crossing points are protected by symmetry or topology, often accompanied by topological surface states as a result of the bulk-boundary correspondence. When external or intrinsic parameters break certain symmetries, global properties of topological quantum materials change dramatically.

	Topological insulator	Dirac semimetal	Weyl semimetal
Band structure	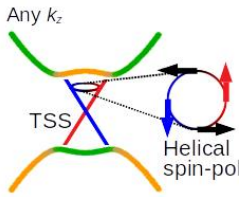	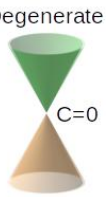	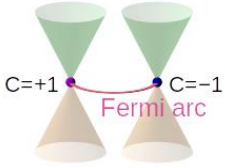
Symmetry	Time-reversal symmetry	Time-reversal and space-inversion symmetry	Broken time-reversal or space-inversion symmetry
Bulk states	Band inverted	Degenerate Dirac cone	Pairs of non-degenerate Dirac cones
Surface states	Helical spin-polarized Dirac cone		Fermi arc
Prototypical materials	Bi_2Se_3, Bi_2Te_3, $Bi_{1-x}Sb_x$	Na_3Bi, Cd_3As_2 (Type-II) $NiTe_2$	(Ta, Nb)(As, P) (Magnetic) $Co_3Sn_2S_2$, Mn_3Sn, Mn_3Ge (Type-II) $Mo_xW_{1-x}Te_2$

Table 2.1: Topological quantum materials

Table 2.1 reviews several classes of topological quantum materials. In topological insulators, the Dirac-cone surface states form inside an inverted bulk band gap, which is protected by time-reversal symmetry. The surface Dirac cone exhibits helical spin-texture and exists at any k_z in momentum space. In contrast, topological semimetals host Dirac cones in the bulk which disperse linearly in three-dimensional momentum space. In Dirac semimetals, crystal symmetry and time-reversal symmetry guarantee existence of a double degenerate Dirac cone. If the Dirac semimetal breaks space-inversion or time-reversal symmetry, a degenerate Dirac cone splits into a pair of non-degenerate Weyl cones, which becomes the Weyl semimetal. A pair of the corresponding Weyl points exhibit opposite chirality, and connected and topologically protected by a Fermi arc at the surface.

Figure 2.1 schematically illustrates a topological phase transition from the normal insulator to the topological insulator as a function of SOC strength. Strong SOC generates band inversion between the bulk conduction band and valence band. The two inverted bands hybridize, opening up an energy gap, where topological insulators can be realized [16]. The Dirac-semimetal phase can appear at the quantum critical point in the topological phase transition, where the bulk conduction and valence bands touch only at discrete (Dirac) points [17].

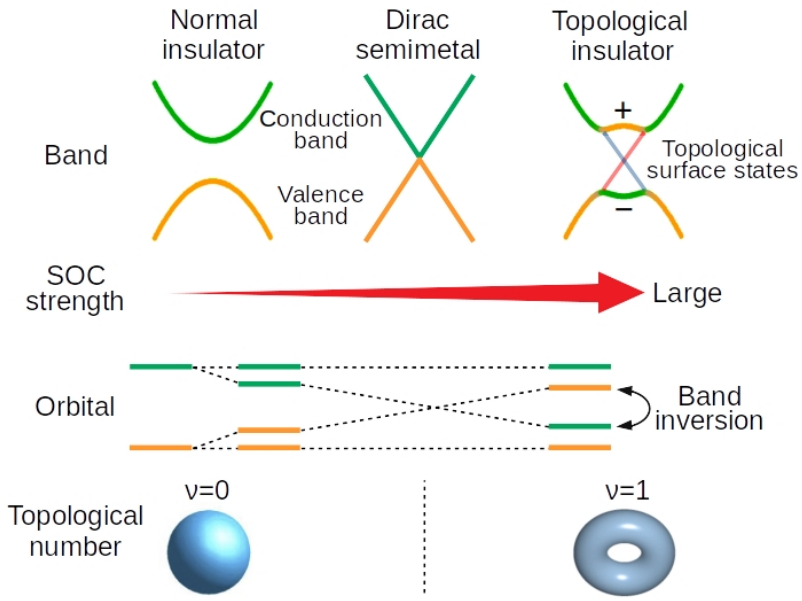

Figure 2.1: Schematic illustration of a topological phase transition from the normal insulator via the Dirac semimetal to the topological insulator as a function of SOC strength.

2.2.2 Chern number

Topology means the mathematical classification of properties of geometric objects by continuous deformation. For instance, a coffee mug can be transformed smoothly into a donut but not into a ball, which means that a coffee mug and a donut are classified as the same group, but a ball as the different group. In this case, the number of holes distinguishes these objects and can be understood as "topological invariant", since the mug can be deformed into the donut without changing the number of holes.

Here, we introduce a topological invariant for band structures, the Chern number. The Chern number is rooted in the mathematical theory but it can be understood physically in terms of the Berry phase [5]. The Berry phase γ [18, 19] is a quantum phase factor that appears in the course of an adiabatic evolution of a quantum-state system. We consider the parametric dependence of the eigenstate of the Hamiltonian $\mathcal{H}(\boldsymbol{R}(t))$ depending on a set of time-dependent parameters $\boldsymbol{R}(t)$, such that $\boldsymbol{R}(t)$ moves on a closed loop C from $t = 0$ and returns to the original position at $t = T$, i.e., $\boldsymbol{R}(t = 0) = \boldsymbol{R}(t = T)$, where γ becomes a gauge-invariant physical quantity. We introduce the n^{th} eigenstate $|\phi_n(\boldsymbol{R}(t))\rangle$. We set $\boldsymbol{R}(t)$ as the Bloch wave vector $\boldsymbol{k}$ and $|\phi_n(\boldsymbol{R}(t))\rangle$ as the Bloch wave function $|u_{n,k}\rangle$. We can also choose the closed loop as the Brillouin zone (BZ) boundary. The Berry phase γ for this loop C is defined as

$$\begin{aligned}
\gamma &= i\int_0^T dt\langle\phi_n(\boldsymbol{R}(t))|\frac{\partial}{\partial t}|\phi_n(\boldsymbol{R}(t))\rangle \\
&= i\oint_C d\boldsymbol{R}\cdot\langle\phi_n(\boldsymbol{R})|\frac{\partial}{\partial R}|\phi_n(\boldsymbol{R})\rangle \\
&= i\oint_C d\boldsymbol{R}\cdot\boldsymbol{A}_n(\boldsymbol{R}) \\
&= i\int_S dS\boldsymbol{\Omega}_n(\boldsymbol{R}).
\end{aligned} \tag{2.13}$$

On the last line, we applied the Stokes's theorem. Here, we define the Berry connection or the Berry vector potential $\boldsymbol{A}_n(\boldsymbol{R})$ and its rotation, i.e., the Berry curvature $\boldsymbol{\Omega}_n(\boldsymbol{R})$ as

$$\begin{aligned}
\boldsymbol{A}_n(\boldsymbol{R}) &= i\langle\phi_n(\boldsymbol{R})|\frac{\partial}{\partial t}|\phi_n(\boldsymbol{R})\rangle, \\
\boldsymbol{A}_n(\boldsymbol{k}) &= i\langle u_{n,k}|\frac{\partial}{\partial t}|u_{n,k}\rangle,
\end{aligned} \tag{2.14}$$

$$\begin{aligned}
\boldsymbol{\Omega}_n(\boldsymbol{R}) &= \nabla_{\boldsymbol{R}}\times A_n(\boldsymbol{R}), \\
\boldsymbol{\Omega}_n(\boldsymbol{k}) &= \nabla_{\boldsymbol{k}}\times A_n(\boldsymbol{k}).
\end{aligned} \tag{2.15}$$

The Berry curvature $\boldsymbol{\Omega}_n(\boldsymbol{R})$ plays the role of the magnetic field perpendicular to the area swept out by the integration path analogous to the field of the magnetic monopole.

The Chern number is the total Berry curvature in the BZ and for the n^{th} band it is defined as

$$\begin{aligned} C_n &\equiv \int_{BZ} \frac{d^2k}{2\pi} \boldsymbol{\Omega}_n(\boldsymbol{k}) \\ &= \oint_{\partial BZ} \boldsymbol{A}_n(\boldsymbol{k}) \cdot \frac{dk}{2\pi}. \end{aligned} \tag{2.16}$$

It can be interpreted as the numbers of monopoles in the BZ and known to become integer for reasons analogous to the quantization of the magnetic monopole [20]. The Chern number can be defined in each band and characterizes its topological structure of whether the phase of the wave function is "twiste". If it is nonzero, it is topologically non-trivial.

D. J. Thouless, M. Kohmoto, M. P. Nightingale, and M. den Nijst showed that, by applying linear response theory, so-called Kubo formula [21], Hall conductivity is quantized to integer multiples of $-\frac{e^2}{h}$ and is connected with the Chern number in the 2D integer quantum Hall system [22] as [5]

$$\sigma_{xy} = \frac{j_y}{E_x} = -\frac{e^2}{h} \sum_{n:\text{filled}} C_n, \tag{2.17}$$

where j_y is the current in y-direction for an applied electrical field in x-direction E_x. The Chern number is therefore also called TKNN number. For a band insulator at $T = 0$, the sum of the Chern numbers for the occupied bands $\sum_{n:\text{filled}} C_n$ gives the number of chiral edge modes which carry charges of integer multiples of $-e$ and propagate only in one direction at each edge. This is the so-called bulk-boundary correspondence [23, 24]. the topological understanding of the quantum Hall effect [25] opened up a new field in condensed-matter physics: topological quantum states of matter.

Let us see a quantum anomalous Hall insulator, a so-called Chern insulator [26], as an example. A Chern insulator with Chern number $C = 2$ exhibits the anomalous quantum Hall effect in the absence of an external magnetic field, accompanied

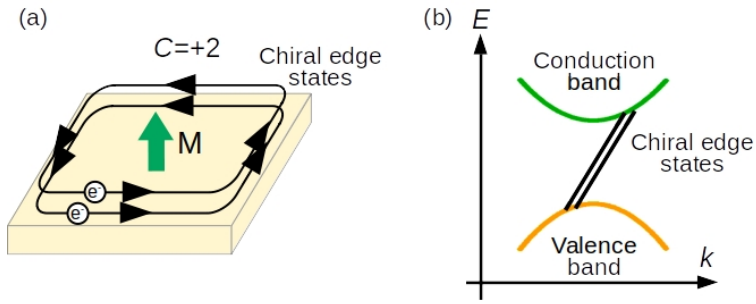

Figure 2.2: Relationship between the Chern number and chiral edge states in a quantum anomalous Hall insulator (Chern insulator) with $C = 2$.

by two chiral edge states as indicated in Fig. 2.2(a). Accordingly, in its electronic structure two topological non-trivial gapless edges states can be formed between the bulk conduction and valence band as shown in Fig. 2.2(b). These right moving edge states with + Fermi velocity indicate the Chern number of this system. As one can also recognize from the asymmetry of the chiral edge states with respect to $k = 0$, this system breaks time-reversal symmetry.

In summary, we derived the following important conclusions in this section:

- The Chern number directly corresponds to the number of chiral edge modes in the quantum Hall system.

- Even without any edge/surface information, the Chern number calculated from the bulk Bloch wave function predicts how the edge/surface states form as a result of the bulk-boundary correspondence.

2.2.3 Bulk-boundary correspondence

As in Chern insulators, Dirac-cone surface states to connect the bulk valence and conduction band in topological insulators and Fermi-arc surface states to connect the Weyl nodes with opposite chirality in Weyl semimetals also form as a result of the bulk-boundary correspondence as shown in Figs. 2.5 and 2.3. Their formation can be understood as decomposition of formation of chiral edge states in Chern insulators later described in detail in Secs. 2.3.2 and 2.4.2.

On the other hand, information of topological surface states in the electronic structure predicts existence of monopoles characterized by the Chern number, the so-called topological chiral charge [27]. The ways are as follows. We consider (i) a closed 2D loop or (ii) a cut in the surface BZ and we count chiral edge modes. We think of band dispersions of chiral edge states. We add up the signs of the Fermi velocities with +1 for right-moving chiral edge modes and −1 for left-moving chiral edge modes. The sum gives (i) the topological chiral charge in the closed cylinder corresponding to the Chern number in the bulk or (ii) the Chern number for the 2D plane.

Now, we apply these criteria to Weyl semimetals. We consider (i) a loop enclosing the Weyl node as shown in Fig. 2.3(a) in the surface BZ. As seen from the band dispersion in Figs. 2.3(b, d), we can find one left-moving chiral edge mode intersected by the loop. Therefore, the cylinder in the bulk BZ contains a topological charge −1. We then consider (ii) a cut between two Weyl nodes as shown in Fig. 2.3(a). We can find one right-moving chiral edge mode as shown in Figs. 2.3(b, c). Thus, the 2D subsystem in the bulk contains Chern number $C = +1$. This indicates that a non-trivial topological charge penetrates the considered 2D plane. The Fermi arc is regarded as a constant-energy cut of chiral edge states at the Fermi level, and therefore in this context, regarded to carry a topological charge.

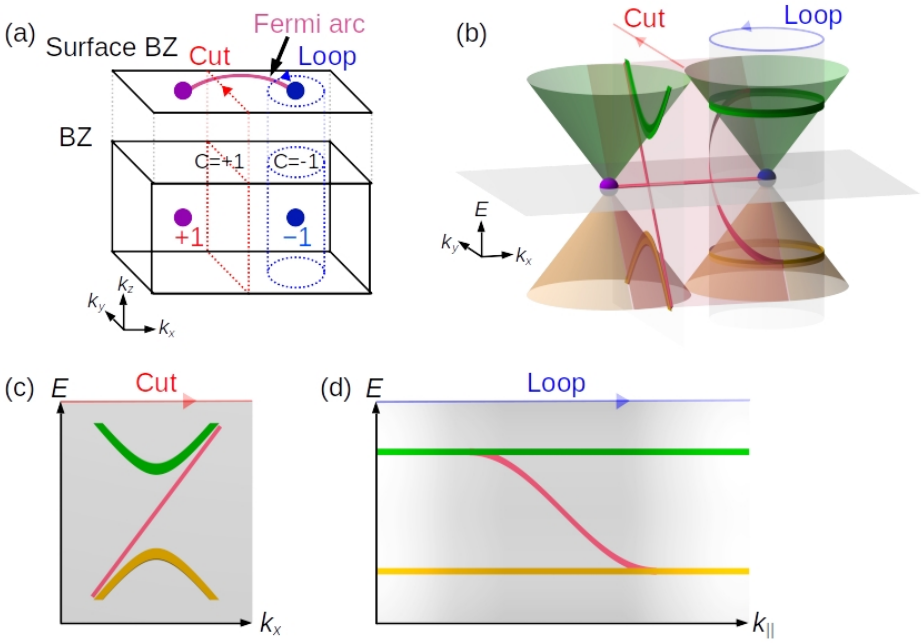

Figure 2.3: Application of the bulk-boundary correspondence to chiral edge states in Weyl semimetals. (a) Brillouin zone and surface Brillouin zone together with a cut and a loop. (b) A pair of Weyl cones in $E-k$ space. (c) $E-k$ section of the cut. One right-moving chiral edge state indicates Chern number $C = +1$. (d) $E-k$ section of the loop. One left-moving chiral edge state indicates Chern number $C = -1$. Green (Orange) planes and sections represent conduction (valence) bands. Pink plane and sections represent chiral edge states and the Fermi arc.

2.3 Topological insulators

2.3.1 Band structures of a time-reversal symmetric system

Before introducing topological insulators, we think of the time-reversal operation. The time-reversal operation transforms t to $-t$ in time, accordingly $\boldsymbol{k}$ to $-\boldsymbol{k}$ in momentum, $\boldsymbol{B}$ to $-\boldsymbol{B}$ in the magnetic field, and $\uparrow$ to $\downarrow$ in spin. Now we consider the spin $\frac{1}{2}$ system described by a time-reversal symmetric Hamiltonian. We can derive the following conclusions by the Kramers theorem and a schematic picture of the resulting band structure is shown in Fig. 2.4:

- The time reversal partner of the eigenstate $\psi_{(\uparrow,\boldsymbol{k})}$ with energy $E(\uparrow,\boldsymbol{k})$ is $\psi_{(\downarrow,-\boldsymbol{k})}$ with $E(\downarrow,-\boldsymbol{k})$, the so-called Kramers pair. For this, it is required that:

$$E(\uparrow,\boldsymbol{k}) = E(\downarrow,-\boldsymbol{k}), \tag{2.18}$$

suggesting that the bands come in pairs, i.e., energy eigenstates are symmetric and the spin is reversed upon $\boldsymbol{k} \to -\boldsymbol{k}$.

- The special points $\boldsymbol{k} = \Gamma_i$ satisfy $\Gamma_i = -\Gamma_i + G$, where G is a reciprocal lattice vector. Γ_i are invariant under the time-reversal operation and are called time-reversal invariant momenta (TRIM). At $\boldsymbol{k} = \Gamma_i$, the bands of Kramers pairs are always degenerate, so-called Kramers degenerate:

$$E(\uparrow, \Gamma_i) = E(\downarrow, \Gamma_i). \tag{2.19}$$

  In a three-dimensional system, there exist 8 TRIM at $\Gamma_i = \frac{1}{2}(n_1 b_1 + n_2 b_2 + n_3 b_3)$ $(n_i = 1, 2, 3)$ where b_k $(k = 1, 2, 3)$ are the primitive vectors of the reciprocal lattice [28].

- When inversion symmetry is present, the bands are degenerate everywhere:

$$E(\uparrow, \boldsymbol{k}) = E(\downarrow, \boldsymbol{k}). \tag{2.20}$$

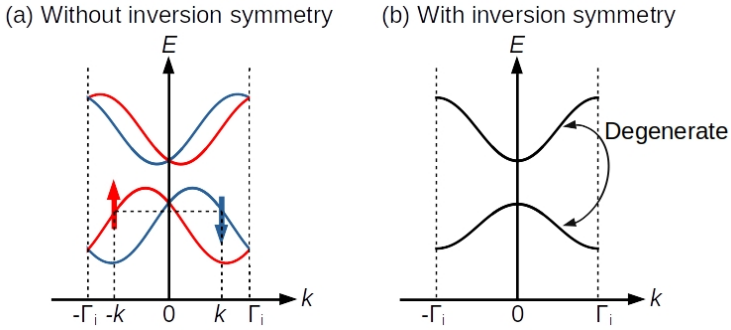

Figure 2.4: Band structures of a time-reversal symmetric system. (a) The time-reversal partners k and $-k$ share the same energy eigenstates, but have opposite spin. Time-reversal symmetry enforces degeneracy at the TRIM Γ_i due to the Kramers theorem and degeneracy is lifted everywhere else in inclusion of SOC. (b) When inversion symmetry is present, the bands are degenerate everywhere.

2.3.2 Z_2 topological insulators

We first see the simplest example of the topological insulator in 2D, also called a quantum spin Hall (QSH) system [29–31]. The QSH system can be realized by a superposition of two quantum Hall systems for the up and down spins with opposite magnetic fields. We assume that the up-spin (down-spin) subsystem has $C_\uparrow = +1$ $(C_\downarrow = -1)$. Hence, the up- and down-spin propagate in the opposite direction at the edge, which is commonly called helical edge states. While the magnetic field vanishes

in the whole system, preserving time-reversal symmetry, an "effective" magnetic field can emerge due to SOC. However, the Chern number C is not well-defined in the QSH system.

Here, we introduce the topological invariant for a QSH system with time-reversal symmetry [28, 29, 32, 33]. As in the Chern number, the topological invariant is related to the bulk wave functions. We define an index δ at each TRIM Γ_i as

$$\delta(\Gamma_i) \equiv \frac{\mathrm{Pf}[w(\Gamma_i)]}{\sqrt{\det[w(\Gamma_i)]}}, \tag{2.21}$$

where $w(\boldsymbol{k})$ is a unitary matrix with elements $w_{mn}(\boldsymbol{k}) = \langle u_m(\boldsymbol{k})|\Theta|u_n(\boldsymbol{-k})\rangle$, $|u_n(\boldsymbol{k})\rangle$ is the occupied Bloch wave function. Θ is the time-reversal operator $\Theta = i\sigma_y K$ with the complex conjugation operator K. Unlike the Chern number, the index δ denotes only the parity, i.e., $(-1)^\nu$ $(\nu = 0, 1)$, which classifies the Hilbert space into "twisted" $(\nu = 1)$ or trivial $(\nu = 0)$. These indices δ indicate whether or not the band inversion occurs at the TRIM Γ_i. The Z_2 topological numbers ν_j are given as products of all or some of the indices

$$(-1)^{\nu_j} = \prod_i \delta(\Gamma_i), \tag{2.22}$$

which distinguishes between the topological insulator $(\nu_j = 1)$ or the normal insulator $(\nu_j = 0)$. If the 2D system in Fig. 2.5 conserves the perpendicular spin p_z, $C_\uparrow + C_\downarrow = 0$ due to time-reversal symmetry, but $\frac{C_\uparrow - C_\downarrow}{2}$ defines a quantized spin Hall conductivity. The Z_2 topological number can be simplified as $\nu = \frac{C_\uparrow - C_\downarrow}{2}$ mod 2.

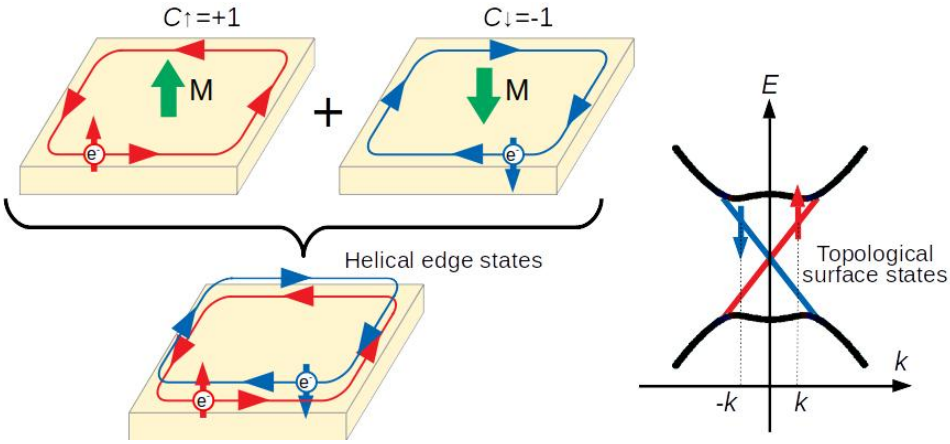

Figure 2.5: Simple model of 2D topological insulators is considered to be a superposition of two quantum Hall systems for the up and down spins with opposite magnetic fields. Helical edge states impose spin-momentum locking.

The most prominent property of topological insulators is the existence of topological surface states. Non-trivial Z_2 topological order ($\nu = 1$) guarantees formation of metallic surface states across the bulk band gap as a consequence of the bulk-boundary correspondence described in Sec. 2.2.3. Helical spin-polarized surface states naturally give rise to so-called spin-momentum locking, namely, the spin of an electron is locked perpendicular to its crystal momentum. This results in properties, such as suppression of non-magnetic backscattering from momenta k to $-k$ at the surface [28, 32, 34] and a dissipationless, pure spin current due to the absence of a net charge flow.

Topological insulators are realized in several materials such as $Bi_{1-x}Sb_x$ [28, 35], Bi_2Se_3, Bi_2Te_3 [16, 36], and so on.

2.4 Dirac and Weyl semimetals

2.4.1 Weyl semimetals

In Weyl semimetals, the Weyl nodes are topologically characterized by the Berry curvature and the Chern number. The Weyl nodes are the source and the sink of the Berry flux in momentum space, acting as a magnetic monopole and antimonopole. The chirality of the Weyl nodes is also connected with the Chern number $C = \pm 1$. Because of the so-called no-go theorem [37, 38], the Weyl nodes should always come in pairs of opposite chirality so that the total chiral charge integrated over the first BZ is zero.

Such Weyl points appear at generic momenta and are formed by band inversion. Therefore, these points can be removed without changing the symmetry of the system, e.g., by changing SOC strength as shown in Fig. 2.1. These crossing points are classified as accidental crossings [4] in contrast to essential crossings which are enforced at high-symmetry momenta (TRIM) by specific crystal symmetries later described in Sec. 2.5.2.

In a Weyl semimetal with time-reversal symmetry but without space-inversion symmetry, the Weyl points distribute symmetrically in momentum (k) space [Fig. 2.6(a)] and the total number of Weyl points must be a multiple of four [4, 15, 39]. This is because the time-reversal operation reverses the Berry curvature $\boldsymbol{\Omega}$ behaving like

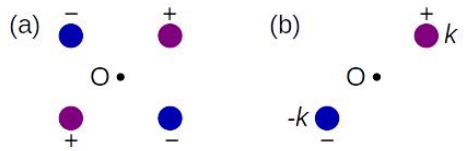

Figure 2.6: Configuration of Weyl points in momentum space with time-reversal but without space-inversion symmetry (a) and with space-inversion symmetry but without time-reversal symmetry (b). Purple and dark blue colors denote the opposite chirality of the Weyl points.

a "magnetic field", i.e., $\boldsymbol{\Omega}(\boldsymbol{k}) = -\boldsymbol{\Omega}(-\boldsymbol{k})$ and the Weyl point at the momentum $\boldsymbol{k}_0 = (k_{x_0}, k_{y_0}, k_{z_0})$ is converted into the Weyl point at $-\boldsymbol{k}_0$ with the same chirality. Since the sum of the chiral charge over the entire BZ needs to vanish, there must be at least one additional pair with opposite chirality. In a Weyl semimetal with space-inversion symmetry but without time-reversal symmetry, the Weyl points distribute antisymmetrically in momentum (k) space [Fig. 2.6(b)] because space inversion requires $\boldsymbol{\Omega}(\boldsymbol{k}) = \boldsymbol{\Omega}(-\boldsymbol{k})$ and thus the Weyl point at $\boldsymbol{k}_0$ are mapped onto $-\boldsymbol{k}_0$ with the opposite chirality [4, 15, 39].

These Weyl nodes necessitate the appearance of the Fermi-arc surface states [40–42]. Unlike usual Fermi surfaces, the Fermi arc is not a closed loop but an open arc that connects the projection of two Weyl points with opposite chirality onto the surface BZ. Formation of the Fermi arc can be understood as a collection of 2D Chern insulators, which will be described in the next subsection.

The Fermi arc is known to tangentially connect the bulk Fermi surface projected onto the surface BZ and then merges into the bulk Fermi surface [43, 44]. The Fermi arc emerges as a helicoid surface in E-k space throughout the wide energy across the Fermi level [45]. Two Fermi surfaces appear on the top and bottom surfaces of the crystal with opposite Fermi velocities.

Weyl semimetals can be realized in transition-metal monoarsenides/monophosphides (Ta, Nb)(As, P), where the crystal structure breaks space-inversion symmetry [46–48]. Magnetic Weyl semimetals breaking time-reversal symmetry can be realized in Mn_3Sn, Mn_3Ge, and $Co_3Sn_2S_2$ [4, 49], and the 2D magnet Fe/W(110) [50].

2.4.2 Properties of Weyl semimetals

One of the important phenomena for Weyl semimetals is the chiral anomaly [51]. Historically, the Adeler-Bell-Jackiw anomaly [52, 53] or the chiral anomaly [54] are introduced in high-energy physics, as a non-conservation of chiral charge in a system of relativistic fermions, coupled to an electromagnetic field with collinear electric and magnetic field. Figure 2.7 shows a simple explanation of the chiral anomaly based on the zeroth Landau level of the Weyl semimetal in the quantum limit. In the absence of an electromagnetic field E and B, the left-handed and right-handed Weyl fermions have equal chemical potentials, which implies that the chirality of Weyl fermions is conserved. An applied magnetic field leads to Landau levels that disperse only along the field direction. The zeroth Landau levels from the left-handed and right-handed chiral Weyl bands are considered to propagate along or opposite to the field direction with opposite velocities due to different chirality. When one applies an electric field E parallel to the magnetic field B, electrons are accelerated at a rate of eE in the $-E$ direction. This motion induces a charge pumping from one Weyl band to the other. There is charge flow around an individual Weyl band, and the chiral charge of each Weyl node is thus not conserved. This then generates an axial charge current.

One direct consequence of the chiral anomaly is negative magnetoresistance [54]. Owing to the axial charge current created by the chiral anomaly, the back scattering from one Weyl state to another one with opposite chirality is suppressed. As a

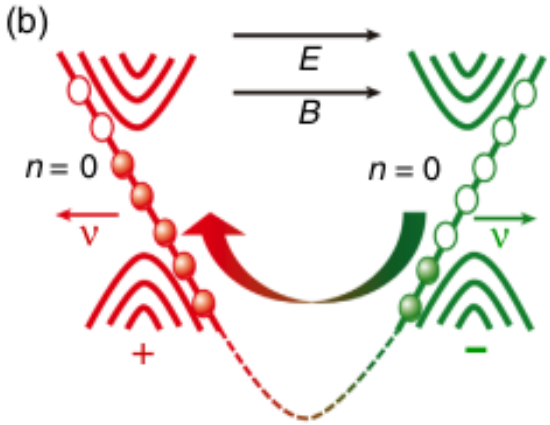

Figure 2.7: Schematic illustration of the chiral anomaly. Adapted from [4].

consequence, the longitudinal conductivity along the applied magnetic field is large and proportional to the magnitude of B. In other words, the resistivity decreases with increasing magnetic field, resulting in the negative magnetoresistance.

Another important transport property for the magnetic Weyl semimetals is the anomalous Hall effect [41, 42, 55]. Here, we describe the formation of the Fermi arc and the Hall effect in a concept that the Weyl semimetal can be viewed as a collection of 2D Chern insulators. We consider the simplest Weyl semimetal containing only one pair of Weyl nodes at $(\pm k_{x_0}, 0, 0)$ as shown in Fig. 2.3. We think of a 2D subsystem in the 3D BZ. Everywhere except at $k_x = \pm k_{x_0}$, band structures cutting through the k_y-k_z plane should be fully gapped. Since the Weyl nodes are described by the Berry curvature field, there must be a Berry flux penetrating all the 2D slices between the two Weyl nodes with the opposite chiral charge. In other words, when the slice is swept through the monopole (antimonopole), Chern number changes by +1 (−1). A 2D slice between the projection of the Weyl nodes, i.e., $-k_{x_0} < k_x < k_{x_0}$ has the Chern number $C = +1$. Each 2D subsystem behaves as a 2D Chern insulator and naturally exhibits a chiral edge state. Hence, the Fermi arc is regarded as a collection of the chiral edge modes of all possible 2D Chern insulator. Since each 2D Chern insulator contributes the Hall conductance, the total Hall conductivity of the system should be directly given by the integral of dk_x as

$$\begin{aligned} \sigma_{yz}^{\text{total}} &= -\frac{1}{2\pi}\int_{BZ} \sigma_{yz}(k_x)dk_x \\ &= -\frac{e^2}{2\pi h}2k_{x_0}, \end{aligned} \tag{2.23}$$

which should be quantized as $-\frac{e^2}{2\pi h}$. Note that the anomalous Hall effect principally diminishes in the space-inversion breaking Weyl semimetal, since it possess at least

two pairs of Weyl points in the BZ, and the total Berry phase contributed by the two Weyl pairs cancels each other.

Weyl semimetals also host exotic optical responses. Interaction with circularly polarized light, which possesses a specific chirality itself, in general, reflects the chirality of matter. In Weyl semimetals, it has been shown that the correlation between circularly polarized light and the intrinsic chirality of the Weyl states drives an unidirectional photocurrent in response to the respective light helicity, which is commonly called circular photogalvanic effect [56–58]. A circularly polarized photon along the $+\hat{i}$ $(i = x, y, z)$ direction couples only one branch of the Weyl cone, namely, only a transition from angular momentum $-\frac{\hbar\hat{i}}{2}$ to $\frac{\hbar\hat{i}}{2}$ for left-circularly polarized light with $L_i = +\hat{i}$ (from $\frac{\hbar\hat{i}}{2}$ to $-\frac{\hbar\hat{i}}{2}$ for right-circularly polarized light with $L_i = -\hat{i}$) is allowed due to the optical selection rule. Depending on the chirality of the Weyl cones, the generated photocurrents propagate in opposite directions. The sum of photocurrents from a pair of Weyl cones with opposite chirality should vanish. However, in some cases, the net photocurrents do not vanish identically.

2.4.3 Dirac semimetals

Coming from the Weyl picture described in Sec. 2.1.1, the Dirac cone in Dirac semimetals can be regarded as a superposition of two Weyl cones with Weyl nodes characterized by the Chern number $C = \pm 1$. Preserved time-reversal and space-inversion symmetries protect degeneracy of chiral-charge states, and therefore guarantee degeneracy of the Dirac cone in spin as well, because of the Kramers theorem (see Sec. 2.3.1). Due to the net Chern number $C = 0$, the Dirac node is not topologically protected and may result in opening up an energy gap. However, the Dirac node can be protected by additional crystal symmetry [59–62]. For instance, n^{th} fold uniaxial rotation $(n = 3, 4, 6)$ symmetry stabilizes a Dirac node, which appears along the rotational axis [59–62]. This mechanism has led to well-established Dirac materials Na_3Bi [60, 63] and Cd_3As_2 [64, 65], in which the Dirac nodes are protected by 3-fold and 4-fold rotational symmetry, respectively. The chiral anomaly can also arise in a Dirac semimetal, since the Dirac fermions can split into pairs of Weyl fermions with opposite chirality under an external magnetic field [66].

2.4.4 Type-II topological semimetal

Quasiparticles in condensed-matter systems are constrained by the symmetries of space groups rather than by Lorentz invariance. Unconventional Lorentz-invariance violating Weyl/Dirac fermions have been proposed, termed type-II Weyl/Dirac fermions, in contrast to conventional Weyl/Dirac fermions referred to as type-I Weyl/Dirac semimetals. Type-II Weyl/Dirac semimetals feature strongly tilted Dirac cones [11] as shown in Table 1.1. In the constant energy momentum map at the Fermi level displayed as a middle planar cut, the Weyl points appear at the boundary between electron and hole pockets forming the upper and lower half of the Dirac cone, respectively,

as compared to a point-like Fermi surface in type-I Weyl/Dirac semimetals. Thus, type-II Weyl/Dirac semimetals possess a finite density of states at the Fermi level (Dirac-point energy). Away from the Fermi level, these electron- and hole-pockets open and are separated in the constant energy cut. Type-II Weyl semimetals host exotic transport properties such as an anisotropic chiral anomaly depending on the current direction, and anisotropic negative magnetoresistance along certain direction [67, 68].

2.4.5 Topological semimetals in transition-metal dichalcogenides

Transition-metal dichalcogenides (TMDCs) constitute an emergent class of materials to host various crystal structures, various class of materials, and rich electronic and physical properties [9, 69, 70]. TMDCs with a chemical formula MX_2, where M is a transition metal and X is a chalcogenide (e.g., S, Se, Te), consist of a stacking of X-M-X trilayers, bond by van der Waals forces. Hence, the 2D nature of TMDCs offers a natural cleaving plane, which can facilitate the fabrication of devices. As shown in Fig. 2.8, TMDCs crystallize in various structures: hexagonal ($2H$), trigonal ($1T$), Monoclinic ($1T'$), and Orthorhombic ($1T_d$). $2H$-structured TMDCs such as MoS_2 and WSe_2 are often semiconductors. $1T$-structured TMDCs such as $PtSe_2$ [71–75], $PtTe_2$ [76], $PdTe_2$ [74, 75, 77–79], and $NiTe_2$ [80–82] are classified as type-II Dirac semimetals due to preserved space-inversion symmetry. On the other hand, $1T_d$-structured TMDCs such as WTe_2 [11] and $MoTe_2$ [83–93], and (Mo, W)Te_2 [85, 91] are classified as type-II Weyl semimetals because of broken space-inversion symmetry. TMDCs host superconductivity and charge density wave in e.g., TaS_2 [69].

$MoTe_2$ is known to have two different crystal phases: the semiconducting $2H$ phase and semimetalic $1T'$ phase. By cooling down below 250 K, the $1T'$-phased $MoTe_2$ undergoes a transition to the $1T_d$ phase [94, 95], where it becomes a type-II Weyl semimetal. $1T'$-MX_2 monolayers have been proposed to be a 2D topological insulator which exhibits the QSH effect [96]. Phenomena related to (type-II) Weyl semimetals were reported. For instance, the magnetoresistance is observed in WTe_2 [97] and $MoTe_2$ [98], which is induced by the chiral anomaly. The anisotropic magnetoresistance is observed in WTe_2 [99]. $MoTe_2$ also hosts Seebeck enhancement of Seebeck effect [100, 101], and superconductivity [102, 103].

The number of Weyl points in $MoTe_2$ has been debated and is still controversial [83–91, 93]. Some studies predicted a total of 4 Weyl points lying at $k_z = 0$ with one inequivalent set of projected Weyl point WP1 onto the surface BZ [84, 91]. Others predicted a total of 8 Weyl points lying at $k_z = 0$ with two inequivalent sets of projected Weyl points W1 and W2 [83]. Others predicted a total of 12 Weyl points with two inequivalent sets of projected Weyl points W1 lying at $k_z = 0$ and W2 lying off the $k_z = 0$ plane [93]. However, one can think of a unified understanding associated with the Weyl phase transition in $Mo_xW_{1-x}Te_2$ [85, 91] as shown in Fig. 2.9(b). According to theoretical studies, the number of Weyl points and their position depends on lattice constant, SOC strength, and atom positions. The band structure of $1T_d$-$Mo_xW_{1-x}Te_2$ contains a hole pocket at the BZ center and two electron pockets at the positive and

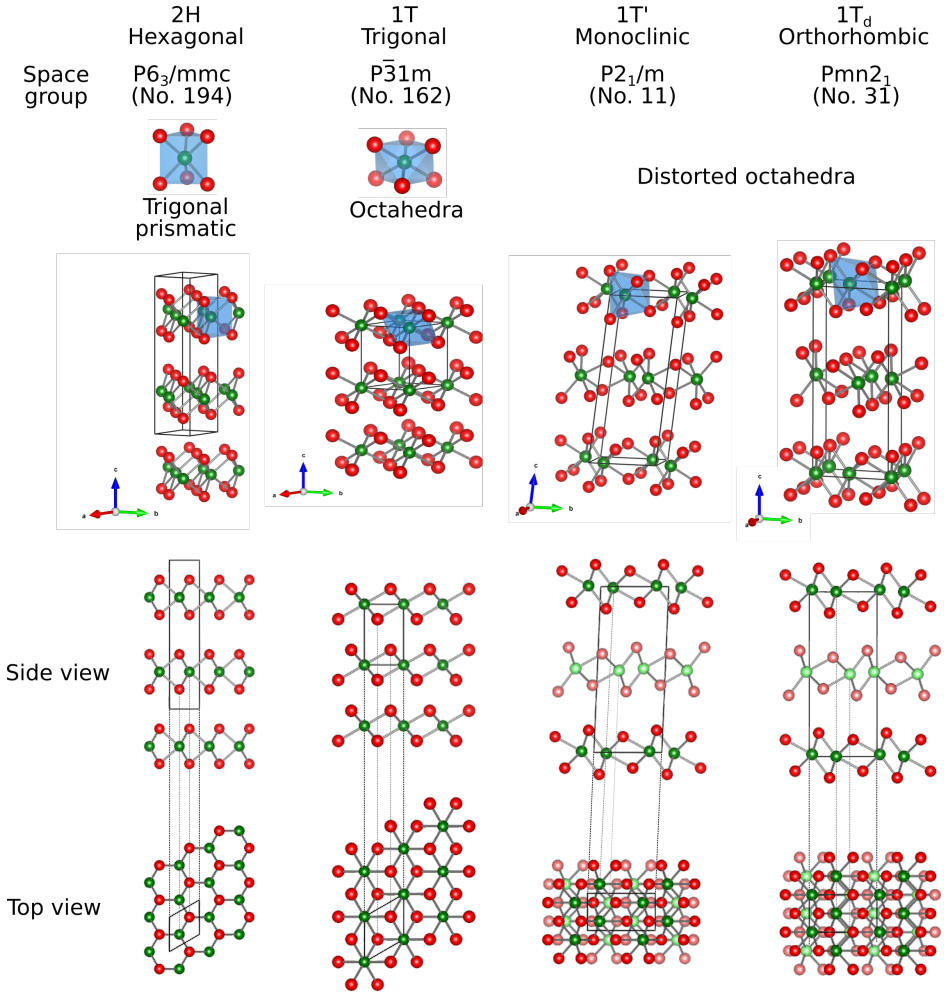

Figure 2.8: Crystal structures of transision-metal dichalcogenides MX_2

negative k_x near the Fermi level. In $Mo_xW_{1-x}Te_2$, total 8 Weyl points appear as the touching points between hole and electron pockets. One type (WP1) is located slightly above the Fermi level. The other (WP2) is located near the Fermi level. By increasing Mo concentration, which naturally modifies the lattice constant, the Weyl points WP1 and WP2 become well separated in momentum space. By further increasing Mo concentration, the Weyl points WP2 annihilate pairwise and $MoTe_2$ possesses a total of 4 Weyl points. Since the Weyl point WP1 is robust against the parameters and has a large Weyl-point separation that can be resolved in measurements, in this thesis, we take a scenario with 4 Weyl points in $MoTe_2$.

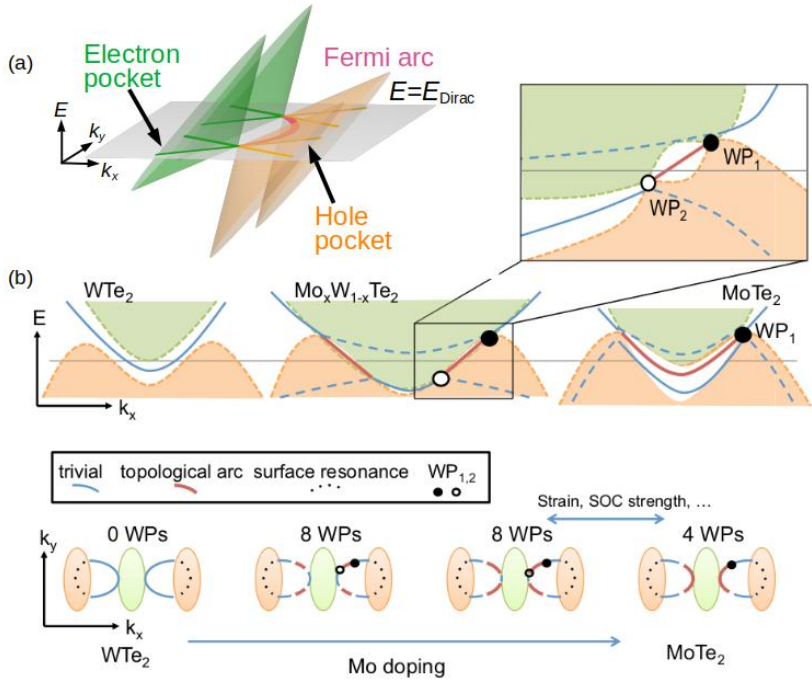

Figure 2.9: Type-II Weyl semimetal $MoTe_2$ (a) A pair of strongly tilted Dirac cones characterizing Type-II Weyl semimetals. (b) Schematic illustration of the Weyl phase transition in $Mo_xW_{1-x}Te_2$. Red and blue contours indicate topological Fermi-arc and trivial surface states, respectively. (b) adapted from [91].

Figure 2.10 reviews type-II Dirac semimetals of the type 1T-MX_2. Previously predicted and experimentally confirmed $PtTe_2$-class type-II Dirac semimetals possess, however, Dirac points far below the Fermi level. In such situation, the physical properties remain still dominated by non-topological properties. Recently, $NiTe_2$ has emerged as the new type-II Dirac semimetal with Dirac points near the Fermi level [80–82].

The 1T-MX_2 crystal structure is composed of edge-sharing MX_6 octahedra with three M-X-M sub-layers as shown in Fig. 2.8. A center transition metal sub-layer divides six chalcogen atoms into two triangle sub-layers indicated by red and orange atoms in Fig. 2.10(b). There is a 180° rotation between these two chalcogen sub-layers, which suggests that both layers are inequivalent. By space inversion ($r \rightarrow -r$), a chalcogen atom can be mapped onto that of the other sub-layer. Thus, this system preserves a 3-fold rotational symmetry (C_3) along the c-axis as well as space-inversion symmetry.

Figure 2.10(a) schematically shows how the bulk Dirac cone in type-II Dirac semimet-

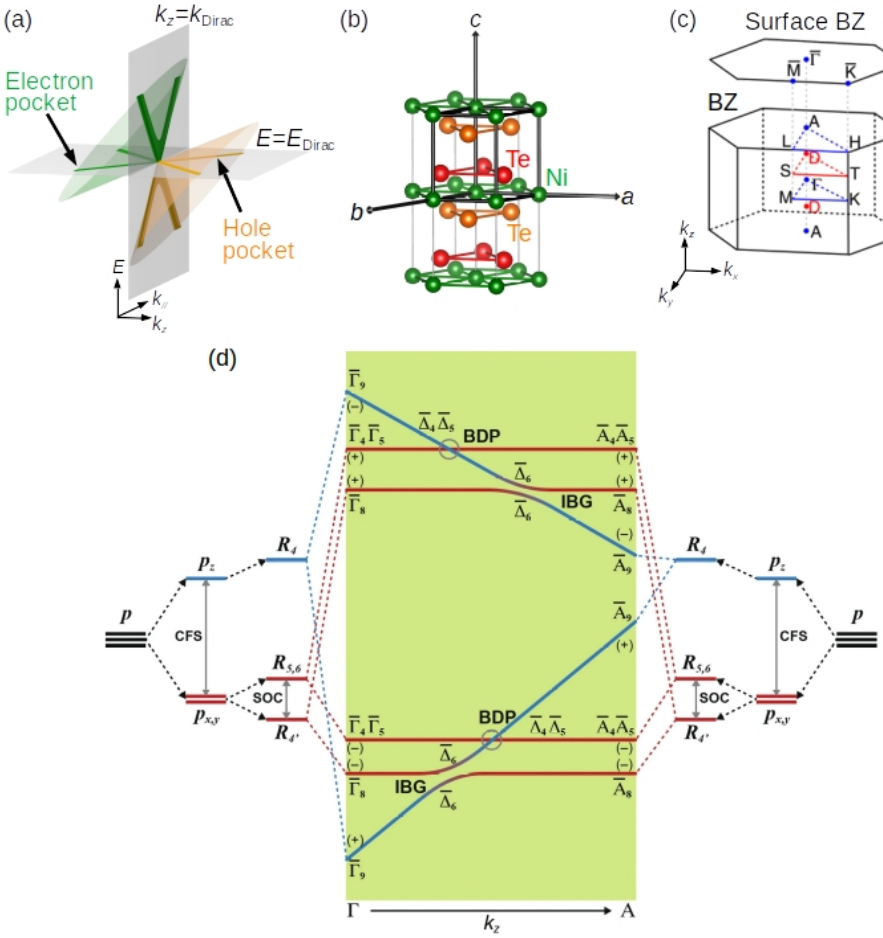

Figure 2.10: Type-II Dirac semimetal 1T-MX_2. (a) Strongly tilted Dirac cone. (b) Crystal structure possessing space-inversion and three-fold symmetry. Red and orange Te atoms represent inequivalent Te atoms. (c) Brillouin zone. (d) Energy hierarchy of p orbitals at the Γ (left) and A (right) points. A combination of crystal-field splitting (CFS), spin-orbit coupling (SOC), and bonding and anti-bonding splitting leads to the different energy levels of the p orbitals. A strong k_z dispersion for the p_z-derived band crosses with other bands and results in the inverted band gap (IBG) and the bulk Dirac point (BDP). The symmetry of the states are labeled with the irreducible representations ($R_i, \Gamma_i, A_i, \Delta_i$) and parity (+, −). (d) adapted from [82].

als of the type 1T-MX_2 appears in (E, k_x, k_y, k_z) space. The Dirac point appears at the D point ($k_z = 0.75\frac{\pi}{c}$ in $NiTe_2$) between the Γ and A points along the C_3 rotational axis in the BZ, shown in Fig. 2.10(c). The Dirac cone is tilted towards the k_z direction. Cutting through the Dirac point energy (E_D) as a constant energy cut, the hole and electron pockets touch at the Dirac point at $k_z = k_D$. Cutting through k_D parallel to the k_z axis, the up-right Dirac cone appears in the $k_z = k_D$ plane.

More interestingly, 1T-MX_2 hosts not only tilted Dirac cones in the bulk but also a surface Dirac cone. The mechanism of such Dirac-cones formation is simply explained by a single chalcogen X p orbital manifold [74, 75] as shown in Fig. 2.10(d). Consider a 2-site model with 3×2 p-orbitals in a trigonal crystal field. A combination of crystal-field splitting, SOC, and bonding and anti-bonding splitting leads to the different energy levels of the p orbitals. Since inter-layer hopping for p_z-orbitals is larger than that of $p_{x,y}$-orbitals, we suppose that inter-layer hopping of $p_{x,y}$-orbitals can be neglected. This approximation is reasonable, because hopping strengths along the c-axis are naturally much larger for p_z orbitals than $p_{x,y}$ orbitals for TMDCs. This results in a large band width of the p_z-orbitals caused by bonding and anti-bonding splitting at the Γ point compared to the A point, and therefore a strong dispersion for the p_z-derived band as a function of the out-of-plane momentum k_z. The strong k_z dispersion for the p_z-derived band crosses with the $p_{x,y}$-derived bands, resulting in two crossing points labeled with BDP and IBG. The crossing labeled with BDP consists of bands with a different reducible representation and is protected by C_3 rotational symmetry against hybridization [61, 62]. Thus, the crossing BDP generate the tilted Dirac cone in the bulk. The other crossing labeled with IBG consist of bands with the same representation. These bands hybridize and open a gap due to an anti-crossing. These bands have opposite parity caused by bonding and anti-bonding splitting, and thus their hybridization leads to an inverted band gap with non-trivial Z_2 topological order, between which Dirac-cone surface states can be formed as in topological insulators.

2.5 Chiral topological semimetals

2.5.1 Unconventional fermions

Recently, unconventional fermions beyond Weyl and Dirac, which have no analogues in high-energy physics, have been proposed [12, 49]. Weyl fermions are characterized by band-crossing points with two-fold degeneracy and Chern number $C = \pm 1$ [Table 2.2(a)], while unconventional fermions are characterized by band-crossing points with multiple (higher than two-fold) degeneracy and a nonzero Chern number which is usually higher than $C = \pm 1$ e.g., as shown in Table 2.2(c-e). Bradlyn et al. systematically examined all non-magnetic space groups in inclusion of SOC and revealed two-, three-, four-, six- and eight-fold degenerate band crossings [12].

(a) Weyl fermion	(b) Dirac fermion	(c) Spin-1 fermion	(d) Double WF	(e) RSW fermion
Two-fold	Four-fold	Three-fold	Four-fold	Four-fold
$C = \pm 1$	$C = 0$	$C = \pm 2$	$C = \pm 2$	$C = \pm 4$
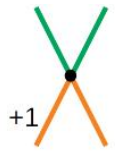		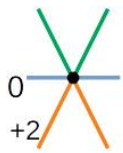	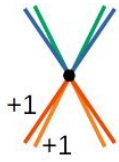	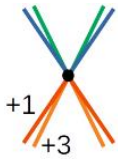

Table 2.2: Conventional and Unconventional fermions in solids. Chern numbers are indicated close to corresponding bands. WF: Weyl fermion. RSW fermion: Spin-3/2 Rarita-Schwinger-Weyl fermion.

2.5.2 Kramers-Weyl fermions

As described in Sec. 2.3.1, the Kramers degeneracy should not be lifted at TRIM with time-reversal symmetry and without inversion symmetry in inclusion of SOC due to the Kramers theorem. Such Kramers degeneracy can form Weyl points, termed Kramers-Weyl fermions [10]. Non-magnetic structurally chiral crystals, which possess no mirror and space-inversion symmetry, are a good platform for realizing Kramers-Weyl fermions. Note that chirality in geometry refers to a concept of "handedness". This means that an object does not coincide with its mirror image. Chang et al. systematically examined chiral space groups [10]. They revealed that all degeneracies at TRIM in non-magnetic chiral crystals with relevant SOC exhibit a non-zero quantized Chern number, and depending on the space group, they can host two-, three-, four-, and six-fold crossings. Thus, unconventional fermions can emerge as Kramers-Weyl fermions there.

Unlike conventional Weyl fermions, Kramers-Weyl fermions are classified as essential crossings [4], which are pinned to the high-symmetry points, i.e., TRIM, by specific crystal symmetries. This enables fermions with maximal separation in momentum space. In contrast to accidental crossings, these points cannot be removed as long as the symmetry is maintained.

2.5.3 Chiral topological semimetals in transition-metal monosilicides

B20 materials with a chemical formula MB, where M is a transition metal and B is a group 14 element, such as transition-metal monosilicides MSi and monogermanide MGe, crystallize in a structurally chiral cubic lattice with space group $P2_13$ (No. 198). They have attracted great interest because they host chiral magnetism and skyrmions in metallic ferromagnets e.g., MnSi and MnGe [104–107] and thermoelectric materials in a correlated narrow-gap semiconductor e.g., FeSi [108]. Recently, it has

been predicted that B20 materials host unconventional fermions induced by structural chirality described in Sec. 2.5.2, termed chiral topological semimetals [10, 109–112].

Figure 2.11 reviews the electronic structure of the chiral topological semimetal CoSi. In this thesis, we ignore accidental crossings in B20 materials appearing at generic momenta in inclusion of SOC [109, 115]. Irrespective of SOC, B20 materials host unconventional fermions. We first consider its electronic structure without SOC as shown in Fig. 2.11(a). All bands are doubly degenerated. At the Γ point, a Dirac band and a flat band form a three-fold degenerate node near the Fermi level with Chern number $C = +2$, which form a fermion shown in Table 2.2(c). At the R point, two separate Weyl cones forms a four-fold degenerate node below the Fermi level with Chern number $C = -2$, which is called a double Weyl cone, shown in Table 2.2(d). The flat band and the top part of the Weyl cone contribute electronic states at the Fermi level, which form a hole pocket centered at the Γ point and an electron

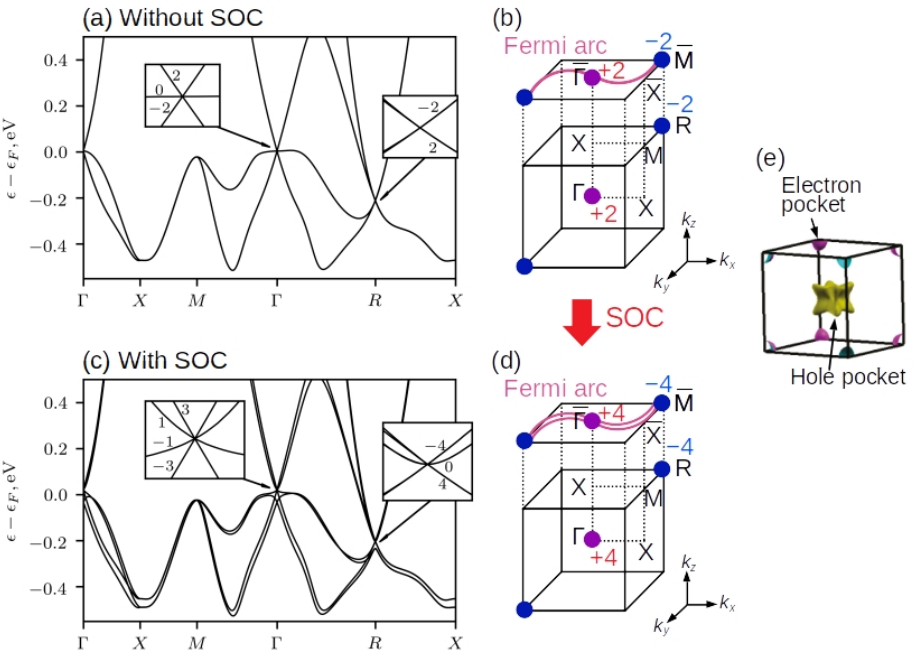

Figure 2.11: Electronic structure of the chiral topological semimetal CoSi with (a, b) and without (c, d) SOC. (a, c) Calculated bulk band structure. Insets show enlargement of bands around the Γ and X points. Chern numbers are indicated close to corresponding bands. (b, d) Brillouin zone and (001) surface Brillouin zone together with emergent chiral charges and Fermi arcs. (e) 3D Fermi surface. SOC results in a change of the Chern number from $C = \pm 2$ to $C = \pm 4$ and spin-splitting of the Fermi arc. (a, c) adapted from [113]. (e) adapted from [114].

pocket centered at the R point in the 3D BZ as shown in Fig. 2.11(e). Due to the bulk-boundary correspondence, the Fermi arc is formed at the surface by connecting two fermions with the opposite chiral charge as shown in Fig. 2.11(b) and lies in the gap between the hole and electron pockets.

When taking into account SOC, all bands split, and accordingly emerging fermions and the Chern number are modified as shown in Fig. 2.11(c, d). At the Γ point a four-fold degenerate node with Chern number $C = +4$ [Table 2.2(e)] and a Weyl fermion appear. At the R point, a six-fold degenerate node with Chern number $C = -4$ emerges. The Fermi arc also splits as a direct consequence of changing the Chern number, since the Fermi arc is regarded to carry a topological charge. Predicted spin-split Fermi arcs and their spin texture are displayed in Fig. 2.12.

First experimental band-structure observations suggest no spin splitting of bands within experimental resolution due to weak SOC in CoSi [114, 116, 117], RhSi [117], AlPt [118], RhSn [119]. Later, several studies observed spin-split Fermi arcs of the strong SOC materials PdGa [120] and PtGa [121].

Properties of chiral topological semimetals depend on structural handedness of chiral crystals. Figure 2.13(a) illustrates the crystal structure of PdGa with opposite handedness. The chiral motif in their structure is the helical arrangement of Pd and

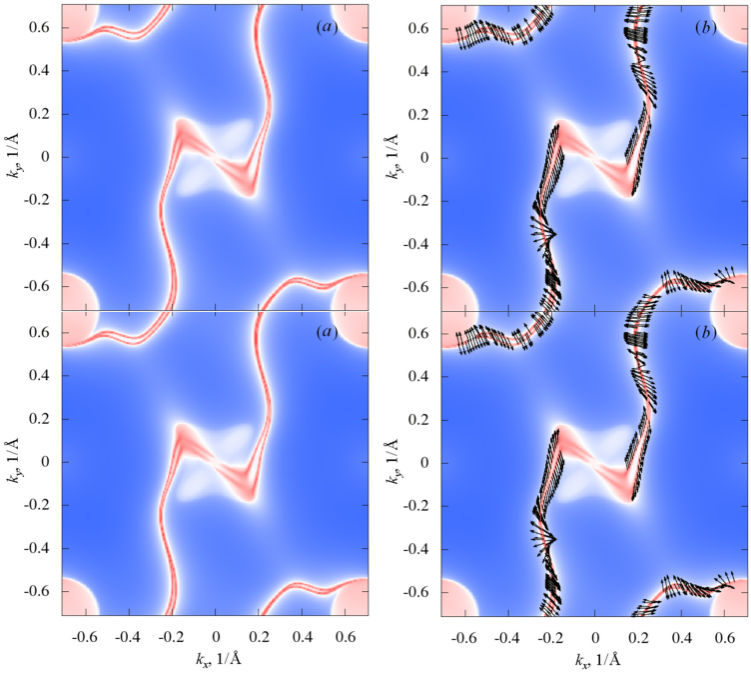

Figure 2.12: Calculated Fermi surface derived from surface for CoSi(100) showing the spin-split Fermi arcs (a) and their spin texture (b). Adapted from [111].

Ga atoms along the (111) direction. On a mirror operation, these helices reverse their handedness. The mirror operation reverses not only the structural chirality but also the sign of the Chern number at the high symmetry points. Accordingly, this leads to a reversal of their Fermi-arc velocities as a consequence of the bulk-boundary correspondence (see Sec. 2.2.3) as shown in Fig. 2.13(C). Schröter et al. succeeded in growing two different enantiomer of PdGa with opposite handedness [120]. The chirality of the crystal structure can be observed from low energy electron diffraction (LEED) patterns of the (100) surface as shown in Fig. 2.13(B). The S-shaped intensity distribution is mirrored when comparing the two enantiomers.

Most Weyl semimetals suffer from several drawbacks, such as large numbers of Weyl points, Weyl fermions close to each other in momentum space, and short Fermi arcs. In such materials, Weyl fermions are located at the non-high-symmetry points. They are less topologically robust, because Weyl points may easily annihilate in pairs e.g., by changing SOC strength. In contrast, CoSi provides platform of the ideal Weyl semimetal with only one pair of Weyl points, manifested as maximal separation of the opposite Weyl points, and correspondingly, the long Fermi arc, irrespective of SOC.

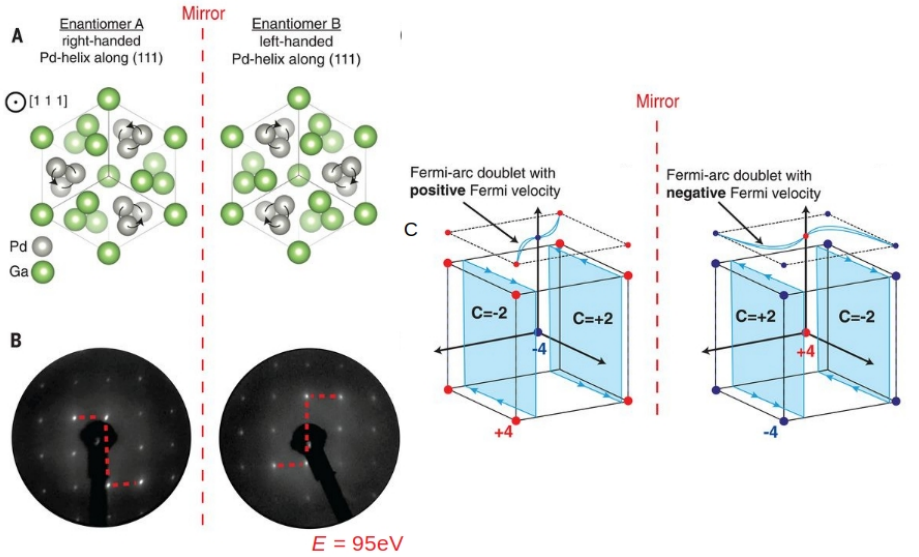

Figure 2.13: Crystal-handedness dependent Chern number and Fermi arc of chiral topological semimetals. (A) Crystal structure of two enantiomers of PdGa with opposite handedness. (B) Low energy electron diffraction (LEED) patterns for two enantiomers. The S-shaped intensity distribution of the spots (highlighted by red dashed lines) reflects the handedness of the crystal structure. (C) Sign of the Chern number and the Fermi-arc velocities are reversed for opposite handedness of the crystal. Adapted from [120]

Moreover, chiral topological semimetals exhibit exotic properties analogous to Weyl semimetals which may reflect larger Chern number and structural chirality in addition [10]. Since one Weyl node at the BZ center sit near the Fermi level and the opposite node lies energetically far away from it, chiral topological semimetals meet the requirement for the quantized circular photogalvanic effect [10, 57, 110, 122]. The helicity-dependent quantized circular photogalvanic effect was observed in RhSi [123] and CoSi [124]. A recent study pointed out that van Hove singularity, namely the singularity in the electronic structure, is realized in a helicoid Fermi arc of chiral topological semimetals in transition-metal monosilicides [125], which will be described in detailed in Sec. 6.3.

3 Experimental methods

Here, we summarize the general description of photoemission spectroscopy [126–128] and electron spin detection [7, 129] in a way that can be usefully applied not only to conventional angle-resolved photoemission spectroscopy but also to momentum microscopy [7, 126]. This enables easy comparison between both methods. Section 3.4 describes how polarization-dependent measurements clarify orbital information of the electronic wave functions and their useful applications to topological quantum materials. Section 3.5 outlines the NanoESCA beamline, where we performed spin-resolved momentum microscopy.

3.1 Photoemission spectroscopy

3.1.1 General description

Photoemission spectroscopy (PES) is based on the photoelectric effect, in which photoelectrons are emitted when a photon impinges on a material and is absorbed by electrons in the solid. In this process, the photon energy of monochromatic light, $h\nu$, and the kinetic energy of the emitted photoelectrons in vacuum, $E_{\mathbf{kin}}$, satisfy the following energy conservation formula (see also Fig. 3.1):

$$E_{\mathbf{kin}} = h\nu - \phi - E_{\mathbf{B}}, \tag{3.1}$$

where $E_{\mathbf{B}}$ is the binding energy of an electron inside the solid before its excitation and ϕ is a material-dependent work function. In order to escape from the material, electrons have to overcome a potential barrier described by the work function ϕ. The photoemission intensity I is related to the transition matrix element and the initial state spectral function which are involved in the photoemission process. Based on eq. 3.1, recording photoemission intensities $I(E_{\mathbf{kin}})$ as a function of $E_{\mathbf{kin}}$ can provide information of the momentum(k)-integrated initial state spectral function, i.e., the density of states. Taking into account the in-plane momentum conservation law, one can record the momentum distribution of photoemission intensities and probe the k-dependent initial state spectral function, which provide information of a band structure.

The photoemission process can be understood in the so-called three step model: (Step 1) Photoexcitation of an electron inside the solid. (Step 2) Travel of the excited photoelectron to the sample surface. (Step 3) Emission of the photoelectron into the vacuum. Here, we emphasize three different states of the electrons:

- $|\phi(i, \boldsymbol{k}_i)\rangle$: **The initial state of the electrons before excitation.**
  $\boldsymbol{k}_i$: The initial state crystal momentum
- $|\phi(f, \boldsymbol{k}_f)\rangle$: **The final state of the electrons after excitation.**
  $\boldsymbol{k}_f$: The final state crystal momentum.
- $\boldsymbol{K}$: The momentum of the electron **after being emitted into vacuum**.

Our final goal is to obtain the initial state information in the solid.

In the photoexcitation process, as shown in Fig. 3.2, the momentum conservation law including the crystal and incident photon momenta $\boldsymbol{q}$ is obtained as

$$\begin{aligned} \boldsymbol{k}_f &= \boldsymbol{k}_i + \boldsymbol{G} + \boldsymbol{q}, \\ k_{f\parallel} &= k_{i\parallel} + G_\parallel + q_\parallel, \\ k_{f\perp} &= k_{i\perp} + G_\perp - q_\perp, \end{aligned} \tag{3.2}$$

where $\boldsymbol{G}$ is an arbitrary reciprocal lattice vector. Here the photon momentum normal to the sample surface is defined as $-q_{i\perp}$. In the case of low photon energy at $h\nu < 100$

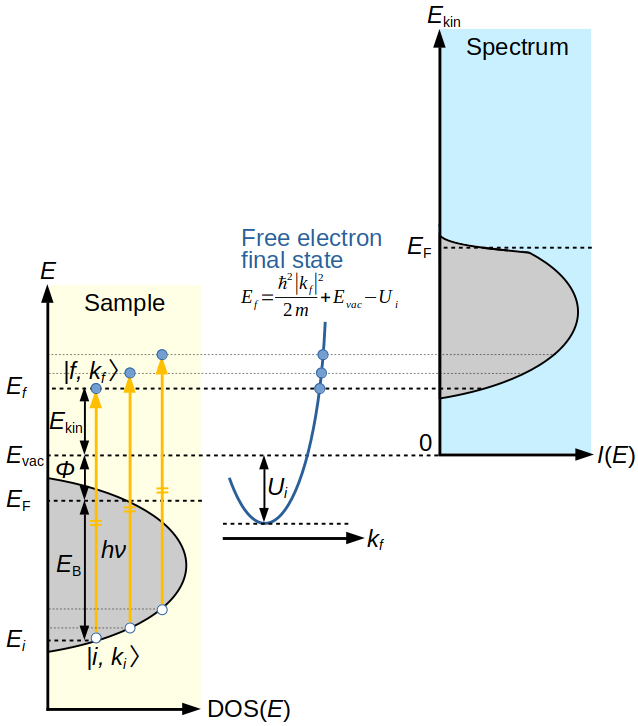

Figure 3.1: Energy diagram of the photoemission process. The final state is often approximated by a parabolic free-electron dispersion (free electron final state model).

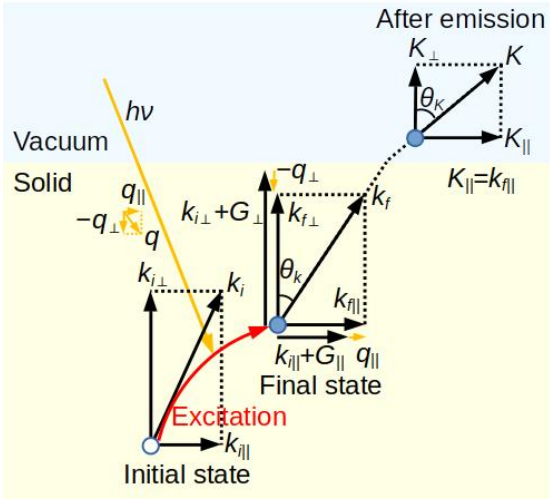

Figure 3.2: Momentum conservation at each state in the photoemission process.

eV, $\boldsymbol{q}$ is often neglected since it is much smaller than $\boldsymbol{k}_i$ and $\boldsymbol{k}_f$. When the photoelectron escapes from the solid to the vacuum, the momentum component parallel to the surface is conserved because of the in-plane translation symmetry of the crystal structure, which can be described as

$$K_\parallel = k_{f\parallel} = k_{i\parallel} + G_\parallel. \tag{3.3}$$

Assuming that the photoelectron in the vacuum is a free electron with the kinetic energy E_{kin} and the free electron mass m, i.e., $E_{\mathrm{kin}} = \frac{|\boldsymbol{p}|^2}{2m} = \frac{\hbar^2|\boldsymbol{K}|^2}{2m}$, the momentum of the emitted electron is described using the polar emission angle θ_K as

$$K_\parallel = \frac{\sqrt{2mE_{\mathrm{kin}}}}{\hbar}\sin\theta_K, \tag{3.4}$$

$$K_\perp = \frac{\sqrt{2mE_{\mathrm{kin}}}}{\hbar}\cos\theta_K. \tag{3.5}$$

Combining eq. 3.4 and the momentum conservation parallel to the surface in eq. 3.3, one can finally reach to

$$k_{f\parallel} = k_{i\parallel} + G_\parallel = \frac{\sqrt{2mE_{\mathrm{kin}}}}{\hbar}\sin\theta_K. \tag{3.6}$$

This equation allows one to calculate $k_{f\parallel}$ by collecting photoelectrons emitted into a certain θ_K in angle-resolved photoemission spectroscopy (ARPES). Note that, in contrast to conventional ARPES, momentum microscopy directly accesses the in-plane crystal momentum $k_{f\parallel} = (k_{fx}, k_{fy})$ and no conversion from θ_K to $k_{f\parallel}$ is necessary.

The momentum component perpendicular to the surface is not conserved during the emission of the photoelectron, but can be deduced under certain assumptions described in the next subsection.

3.1.2 Free electron final state model

To address the out-of-plane momentum $k_\perp$, we introduce the free electron final state model which assumes that the dispersion of the unoccupied bands is approximated by a free-electron dispersion [126] (see Fig 3.1). The free-electron dispersion of the final state with a band minimum at $E_{\text{vac}} - U_i$ is described as

$$E_f(|\boldsymbol{k}_f|) = \frac{\hbar^2 |\boldsymbol{k}_f|^2}{2m} + E_{\text{vac}} - U_i, \tag{3.7}$$

where U_i is the inner potential, i.e., energy at the bottom of the free-electron valence band with respect to the vacuum level energy E_{vac}. This dispersion describes a parabola for the energy as a function of $\boldsymbol{k}_f$. Based on eq. 3.2, we replace $\boldsymbol{k}_f$ with $\boldsymbol{k}_i - \boldsymbol{G}$ as

$$\begin{aligned} |\boldsymbol{k}_i - \boldsymbol{G}|^2 &= \frac{2m}{\hbar^2}(E_f - E_{\text{vac}} + U_i) \\ &= \frac{2m}{\hbar^2}(E_{\text{kin}} + U_i). \end{aligned} \tag{3.8}$$

Here, we applied $E_f = E_{\text{vac}} + E_{\text{kin}}$ (see Fig. 3.1). With E_{kin} =constant, this describe a sphere in k space centered at $-\boldsymbol{G}$ with a radius of $\frac{\sqrt{2m}}{\hbar}\sqrt{E_{\text{kin}} + U_i}$. A momentum disk at a certain kinetic energy E_{kin} obtained by momentum microscopy can be regarded as the constant-energy spherical surface in k space described by eq. 3.8 projected onto the $k_\parallel$ plane in the surface BZ. Since E_{kin} varies with $h\nu$ in eq. 3.1, by varying $h\nu$ one can access the $k_{i\perp}$ dispersion of the bands. U_i can be determined experimentally by the periodicity of the bands in $k_{i\perp}$. When U_i is known, the perpendicular momentum component can be evaluated as

$$\begin{aligned} k_{i\perp} &= k_{f\perp} - G_\perp \\ &= \sqrt{\frac{2m}{\hbar^2}(E_{\text{kin}} + U_i) - {k_{f\parallel}}^2} - G_\perp. \end{aligned} \tag{3.9}$$

3.1.3 Photoemission process

The photoemission process is driven by the interaction of the solid with a dynamic electromagnetic field. The electrons in a solid are described by the electron Hamiltonian $\mathcal{H}_{\text{e}}$. After the light irradiation, the Hamiltonian for the total system is written using the photon Hamiltonian $\mathcal{H}_{\text{ph}}$ and the Hamiltonian $\mathcal{H}_{\text{int}}$ for interactions between electrons and photons as,

$$\mathcal{H} = \underbrace{\mathcal{H}_{\text{e}} + \mathcal{H}_{\text{ph}}}_{\mathcal{H}_0} + \underbrace{\mathcal{H}_{\text{int}}}_{\mathcal{H}'} \tag{3.10}$$

Since $\mathcal{H}' = \mathcal{H}_{\text{int}}$ is considered to be a time-dependent perturbing Hamiltonian the transition probability $w_{i\to f}$ from the occupied initial state $\phi_i^{\boldsymbol{k}}$ into the unoccupied final

state $\phi_f^{\boldsymbol{k}}$ is obtained by time-dependent perturbation theory in quantum mechanics as

$$w_{i\to f} = \frac{2\pi}{\hbar}|\langle\phi_f^k|\mathcal{H}_{\rm int}|\phi_i^k\rangle|^2\delta(E_f - E_i - h\nu), \tag{3.11}$$

which represents Fermi's golden rule. The δ function ensures energy conservation in the excitation process. The photoemission intensity is proportional to $w_{i\to f}$ and is described as

$$I \sim w_{i\to f} \propto |\langle\phi_f^k|\mathcal{H}_{\rm int}|\phi_i^k\rangle|^2 = \left|M_{f,i}^{\boldsymbol{k}}\right|^2, \tag{3.12}$$

where $M_{f,i}^{\boldsymbol{k}}$ is the transition matrix element.

The Hamiltonian in an electromagnetic field in eq. 2.10 is further written as

$$\begin{aligned}
\mathcal{H} &= \frac{1}{2m}\left(\boldsymbol{p} - \frac{e}{c}\boldsymbol{A}\right)^2 - e\phi \\
&= \underbrace{\frac{1}{2m}\boldsymbol{p}^2}_{\mathcal{H}_{\rm e}} + \underbrace{\frac{e}{2mc}(\boldsymbol{A}\cdot\boldsymbol{p} + \boldsymbol{p}\cdot\boldsymbol{A}) + \frac{e^2}{2mc^2}\boldsymbol{A}^2 - e\phi}_{\mathcal{H}_{\rm int}} \\
&\approx \mathcal{H}_{\rm e} + \frac{e}{mc}\boldsymbol{A}\cdot\boldsymbol{p}.
\end{aligned} \tag{3.13}$$

On the third line, we neglect the term $\frac{e^2}{2mc^2}\boldsymbol{A}^2$ describing two-photon processes, enforce the Weyl gauge in which $\phi = 0$, and apply $\nabla\cdot\boldsymbol{A} = 0$ for a plane electromagnetic field.

One of the solutions of $\boldsymbol{A}$ for the plane electromagnetic field is

$$\boldsymbol{A}(\boldsymbol{r}, t) = \boldsymbol{\epsilon}e^{i(\boldsymbol{k}\boldsymbol{r} - c|\boldsymbol{k}|t)} \approx A_0\boldsymbol{\epsilon}, \tag{3.14}$$

where the vector $\boldsymbol{\epsilon}$ denotes the oscillating direction of the electric field of the incident light, $\boldsymbol{k}$ is the wave vector, and $\boldsymbol{r}$ is the position operator. Since the wave length λ of the radiation field (e.g., $\lambda = \frac{2\pi}{|\boldsymbol{k}|} = 124\,\text{Å}$ for $h\nu = 100\,\text{eV}$) is much longer than the atomic dimension (~ Å), i.e., $\boldsymbol{k}\cdot\boldsymbol{r} \approx 2\pi\frac{a_0}{\lambda} << 1$ (a_0 : Lattice constant), we can apply the approximation: $e^{i\boldsymbol{k}\cdot\boldsymbol{r}} = 1 + i\boldsymbol{k}\cdot\boldsymbol{r} + \cdots \approx 1$ to eq. 3.14, known as dipole approximation. Therefore, the matrix element can be expressed as

$$\begin{aligned}
M_{f,i}^{\boldsymbol{k}} &= \frac{e}{mc}\langle\phi_f^k|\boldsymbol{A}\cdot\boldsymbol{p}|\phi_i^k\rangle \\
&\approx \frac{e}{mc}\langle\phi_f^k|A_0\boldsymbol{\epsilon}\cdot\boldsymbol{p}|\phi_i^k\rangle \\
&= \frac{e}{mc}A_0\langle\phi_f^k|\boldsymbol{\epsilon}\cdot[\boldsymbol{r}, \mathcal{H}_0]|\phi_i^k\rangle \\
&= -\frac{ie}{\hbar c}A_0\langle\phi_f^k|\boldsymbol{\epsilon}\cdot\boldsymbol{r}\mathcal{H}_0^\dagger - \mathcal{H}_0\boldsymbol{\epsilon}\cdot\boldsymbol{r}|\phi_i^k\rangle \\
&= -\frac{ie}{\hbar c}A_0(E_f - E_i)\langle\phi_f^k|\boldsymbol{\epsilon}\cdot\boldsymbol{r}|\phi_i^k\rangle.
\end{aligned} \tag{3.15}$$

On the third line, we applied the commutator relationship $\frac{\hbar\boldsymbol{p}}{m} = -i[\boldsymbol{r}, \mathcal{H}_0]$. The term $\boldsymbol{\epsilon}\cdot\boldsymbol{r}$ represents electric dipole moment.

3.1.4 Surface sensitivity

The surface sensitivity of PES depends on the photon energy [130]. The photoelectron signal is attenuated by inelastic scattering. Although the inelastic mean free path of electrons is material dependent, it can be assumed to follow a universal curve as a function of the kinetic energy of the electron in the energy region $E_{\mathrm{kin}} > 20\,\mathrm{eV}$ as shown in Fig. 3.3. A minimum of the universal curve is found around 20-100 eV with 3-10 Å. This implies that PES with vacuum ultraviolet (VUV) light is highly surface sensitive and probes predominantly the top few atomic layers. In the case of the low-energy region $E_{\mathrm{kin}} < 10\,\mathrm{eV}$, the inelastic mean free path could be material dependent [126].

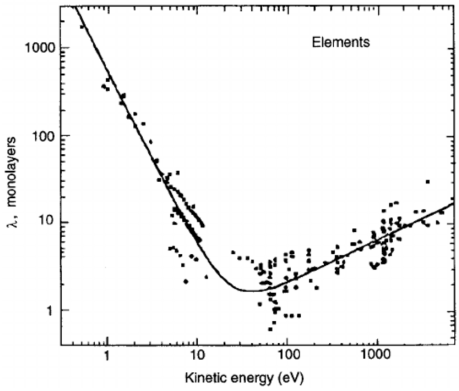

Figure 3.3: The inelastic mean free path of electrons as a function of kinetic energy for various materials. Adapted from [130].

3.2 Momentum microscopy

3.2.1 Overview

Momentum microscopy is based on the principles of photoemission electron microscopy (PEEM) [131]. As outlined in Fig. 3.4, the momentum microscope system consists of a sample stage, PEEM optics, a double hemispherical analyzer, a 2D detector. The momentum microscope collects all electrons emitted into complete half space from the sample surface by applying an acceleration voltage between the sample and the microscope objective lens. Therefore, it directly provides two-dimensional photoelectron maps $I(k_x, k_y)$ of the in-plane crystal momentum over the whole Brillouin zone at a single measurement in sharp contrast to conventional ARPES that collects and records a certain emission angle of photoelectrons. It records individual momentum discs $I(k_x, k_y)$ at a fixed energy. The 3D $I(k_x, k_y, E_{\mathrm{B}})$ data, that yields the band dispersion along all directions in the surface BZ, is then obtained by a series of such

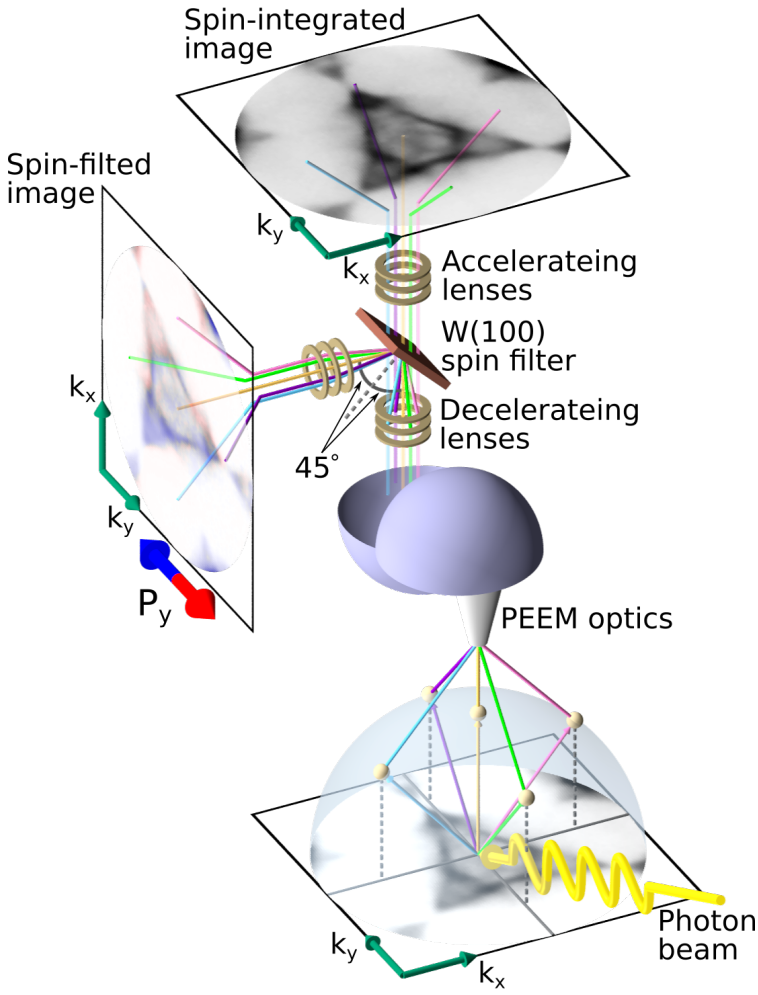

Figure 3.4: Schematic illustration of band structure imaging by momentum microscopy equipped with an imaging spin filter. The momentum microscope collects all electrons emitted into complete hemisphere above the sample. The imaging spin filter can be inserted/retracted after the second hemispherical analyzer. Electrostatic decelerating and accelerating lenses before and after the scattering target allow the selection of the scattering energy, E_s, of electrons. Electrons are reflected from the imaging spin filter crystal at an angle of incidence 45°, with small deviations. Every position of the image is encoded as a different reflection angle of the electron. The spin-filtered image is flipped up on the reflection with respect to the plane perpendicular to the scattering plane (k_y).

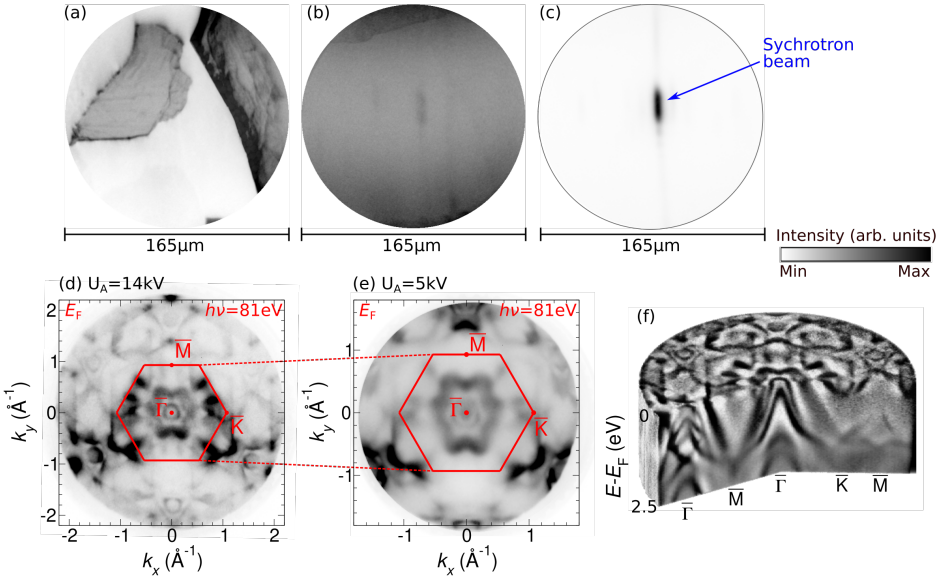

Figure 3.5: Selective local band structure measurement of $NiTe_2$. (a-c) The best sample region is explored by PEEM illuminated with a mercury lamp. (b) We found a flat and good region. (c) In order to record band dispersions, we turned the synchrotron beam on, showing strong intensity near the PEEM image center. (d, e) We measured Fermi surface with the different acceleration voltage U_A. U_A = 5 kV enlarges momentum space compared to U_A = 14 kV. (f) Scanning the binding energy E_B yield the 3D band dispersion map $I(k_x, k_y, E_B)$.

measured constant-energy momentum discs by scanning the binding energy E_B as shown in Fig. 3.5(f).

The momentum microscope enables both real-space PEEM mode and momentum space mode in the same instrument by changing the optical lens settings. Figures 3.5(a-c) shows how PEEM images help us find a good sample region. Figure 3.5(a) shows a PEEM image on the boundary of a well cleaved region in $NiTe_2$. High contrast between black and white regions shows different regions of the sample, indicating that a well cleaved region exhibits high intensity (black intensity). The well cleaved region, however, shows inhomogeneous intensity with several terraces. After moving the sample, we found a flat and good region as shown in Fig. 3.5(b). Figure 3.5(c) shows a PEEM image after turning the synchrotron beam on. Strong intensity near the image center suggests the beam spot size 10 μm (V) × 20 μm (H). After we have identified a good sample region, the microscope is then switched to the momentum image mode to record the band dispersions as indicated in Figs. 3.5(d, e). Therefore, the analyzed area for momentum maps [Figs. 3.5(d, e)] is the area with strong intensity near the PEEM image center in Fig. 3.5(c). In this way, we can

measure the local electronic structure on nano-sized samples and individual domains.

3.2.2 Working principles

Photoelectrons are emitted with an angle θ with respect to the sample surface normal from the sample and are accelerated by an electron optical immersion lens. The lens sees a virtual sample located behind the real sample surface, from which photoelectrons are emitted with an effective angle $\theta'(< \theta)$. Even those photoelectrons that are emitted parallel to the surface ($\theta = 90°$) enter the lens under a finite angle θ'. The initial emission angle θ is related to the initial momentum $\hbar k = \sqrt{2mE_{\mathrm{kin}}}$ as $\sin\theta = \frac{\hbar k_\parallel}{\hbar k} = \frac{\hbar k_\parallel}{\sqrt{2mE_{\mathrm{kin}}}}$, and the effective angle θ' is related to the momentum after acceleration $\hbar k' = \sqrt{2m(eU_A + E_{\mathrm{kin}})}$ as $\sin\theta' = \frac{\hbar k'_\parallel}{\hbar k'} = \frac{\hbar k'_\parallel}{\sqrt{2m(eU_A+E_{\mathrm{kin}})}}$. Since the acceleration along the surface-normal preserves the surface parallel momentum component, $k_\parallel = k'_\parallel$, we obtain:

$$\sin\theta' = k_\parallel \frac{\hbar}{\sqrt{2m(eU_A + E_{\mathrm{kin}})}} \approx k_\parallel \frac{\hbar}{\sqrt{2meU_A}}. \tag{3.16}$$

When the acceleration voltage U_A is large compared to the initial kinetic energy E_{kin} of the photoelectrons, $eU_A >> E_{\mathrm{kin}}$, $\sin\theta'$ is scaled linear in $k_\parallel$ [6, 132]. For a geometrical lens with focal length f, a beam that enters the lens under an angle θ' will be focused in the momentum image plane in the distance $r_k = f\tan\theta'$ from the optical axis. With $\tan\theta' \approx \sin\theta'$, thus, the lateral position in the image focal plane can be directly calibrated in $k_\parallel$. For a fixed θ', i.e., a fixed position in the momentum image plane, $k_\parallel$ becomes larger with increasing U_A. This means that with increasing U_A the momentum field of view becomes larger as demonstrated in Figs. 3.5(d, e). In such way, band structure imaging from overview to highest resolution is possible.

The momentum image is formed in the back focal plane of the objective lens. The spatial image is formed further downstream. The momentum microscope enables one to switch the image plane between the real-space and momentum-space image by changing the electron-optical lens settings. With increasing U_A the momentum field of view becomes larger, while the spatial (PEEM) field of view becomes smaller. This corresponds to the fact that when the momentum image shrinks in the focal plane, the spatial image in the image focal plane expands accordingly.

The double hemispherical analyzer plays a crucial role as an aberration compensated energy filter. The first hemispherical analyzer selects the energy of the electrons. The second hemispherical analyzer compensates the aberration introduced by the first analyzer. Due to the spherically symmetric $1/r$ potential (r: the radius), electron trajectories can be interpreted as Kepler ellipses, giving rise to the largest energy dispersion after a deflection angle of 180° or after passing the first analyzer [133]. Electrons are again refocused after the second analyzer by reversing the beam path in the second anti-symmetrical analyzer, realizing an effective 360° pass, like closed trajectories of Kepler ellipses for the 360° deflection [134].

An improved high-resolution momentum microscope with double-pass energy filter is reviewed in Ref. [135].

3.2.3 Momentum microscopy vs. ARPES

To conclude this section, let us summarize the advantages of momentum microscopy compared to ARPES.

- Momentum microscopy enables both real-space PEEM imaging and momentum-space band structure imaging. Thus, we can select an analyzed area of the band structure measurement.
- Momentum microscopy provides 2D photoemission intensity distribution $I(k_x, k_y)$ at a single measurement, while ARPES requires scanning an emission angel θ together with rotating the sample or moving the analyzer especially for spin-resoled ARPES.
- Momentum microscopy captures all emission directions θ in the complete emission hemisphere above the sample and covers the maximum $k_\parallel$ space described by the photoemission horizon for emission angles of $\theta = \pm 90°$ (see Fig. 3.6). ARPES capture a relatively small fraction of the emission hemisphere up to, e.g., $\theta = \pm 30°$ and covers a smaller $k_\parallel$ space described by eq. 3.4.
- The fixed photoemission geometry, where the angle of photon incidence stays constant during the measurement without rotating the sample, gives direct access to symmetry dependent effects of wave functions and light polarization.

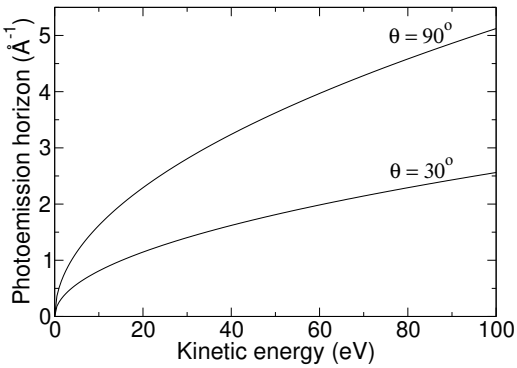

Figure 3.6: The maximum accessible $k_\parallel$, the photoemission horizon, is given when the emission angle θ reaches 90° in eq. 3.4: $k_\parallel^{\max} = \frac{\sqrt{2mE_{\text{kin}}}}{\hbar} \sin 90° = \frac{\sqrt{2mE_{\text{kin}}}}{\hbar}$. The photoemission horizon follows the parabolic dispersion of a free electron in the vacuum as a function of the photoelectron kinetic energy. The accessible $k_\parallel$ for emission angles of $\theta = 30°$, $k_\parallel = \frac{\sqrt{2mE_{\text{kin}}}}{\hbar} \sin 30°$, is plotted for comparison.

- The parallel momentum imaging allows a direct combination with an imaging spin filter, providing spin-resolved 2D photoemission intensity distribution $I(k_x, k_y)$ (see Sec. 3.3.2).

3.3 Spin-resolved momentum microscopy

3.3.1 Principle of electron spin detection

A measurement of the spin of a free electron cannot be realized in an "ideal" Stern-Gerlach type experiment due to the Heisenberg uncertainty relation and the strong effect of the Lorentz force by a magnetic field [136]. Thus, we can only detect the electron spin using a spin-dependent electron scattering experiment. So far, there are two primary methods of detecting the electron spin [7, 129]. One is utilizing SOC between the incoming electrons and a non-magnetic scattering target. The other is utilizing exchange interaction between the incoming electrons and a ferromagnetic scattering target. The most common detector using SOC as the fundamental interaction is the Mott detector [137, 138], which employs heavy-element targets such as Au or Th. Another detector based on SOC is single-channel spin-polarized low-energy electron diffraction (SP-LEED) by W(100) [139, 140]. As a detector based on exchange interaction, very low-energy electron diffraction (VLEED) detector such as Fe(100)/Ag(100) [141], improved and long life time Fe(001)$p(1 \times 1)$-O [142–145] are developed. All detectors mentioned above are so far employed as single-channel detectors. Recently, an imaging spin filter by W(100) [146–148], Ir(100) [149], long life time Au/Ir(100) [6, 150, 151] has been developed as a multi-channel detector based on SOC.

Here, we describe basics of electron spin detection taking Mott scattering [138] as

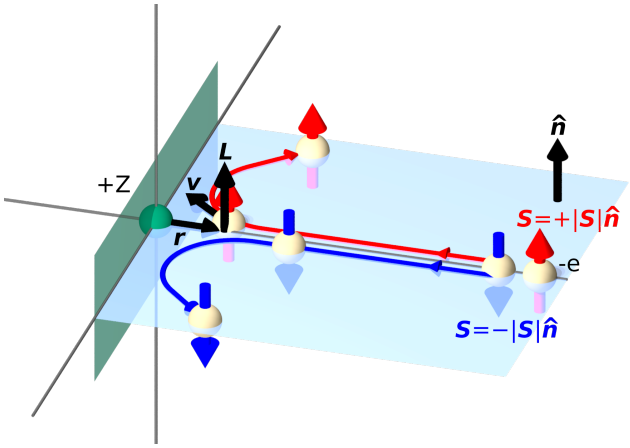

Figure 3.7: Schematic illustration of Mott scattering.

an example. Mott scattering describes the scattering of an electron Coulomb field of the atomic nucleus, including the effect of SOC. The SOC contribution to the Hamiltonian is given by

$$\mathcal{H}_{\mathrm{SOC}} = \frac{e}{2m^2c^2r}\frac{d\phi}{dr}(\boldsymbol{L}\cdot\boldsymbol{S}) = \frac{Ze^2}{2m^2c^2r^3}(\boldsymbol{L}\cdot\boldsymbol{S}), \tag{3.17}$$

$$\phi(r) = -\frac{eZ}{r}, \tag{3.18}$$

where $\phi(r)$ is the Coulomb potential, Z is the atomic number, and $\boldsymbol{L}$ and $\boldsymbol{S}$ are the orbital and spin angular momentum. SOC contributes to the scattering potential and induces a spin-dependent spatial asymmetry of the reflected electrons (see Fig. 3.7), which leads to the following results.

- The term $\boldsymbol{L}\cdot\boldsymbol{S}$ depends on spin polarization of electrons. Thus, the scattering probability of spin-polarized electron to right and left will be different. Taking into account that the term $\boldsymbol{L}\cdot\boldsymbol{S}(>0)$ can be maximized and can induce maximum repulsion if $\boldsymbol{S} = \pm|S|\hat{\boldsymbol{n}}$ ($\hat{\boldsymbol{n}}$: unit vector normal to the scattering plane), the scattering probability is related to spin polarization perpendicular to the scattering plane.
- $\mathcal{H}_{\mathrm{SOC}}$ becomes large for high-Z heavy elements and larger $\boldsymbol{L}$. Heavy-element materials are suitable for use as scattering target.

Left-right scattering asymmetry can be defined as

$$A = \frac{I_L - I_R}{I_L + I_R}, \tag{3.19}$$

where I_L (I_R) is the intensity of the detected electrons scattered to the left (right). The asymmetry A is related to the spin polarization P as

$$P = \frac{A}{S} = \frac{1}{S}\frac{I_L - I_R}{I_L + I_R}, \tag{3.20}$$

where S is the Sherman function, i.e., the spin sensitivity of the detector. S depends on the target material, the electron energy, and the scattering angle, and can be evaluated experimentally.

The scattered intensity I is proportional to the differential cross section $\frac{d\sigma}{d\Omega}$ and can be written as [136]

$$\begin{aligned} I &= \frac{d\sigma}{d\Omega}I_0, \\ \frac{d\sigma}{d\Omega}(\theta,\phi) &= R(\theta,\phi)\left(1 + S(\theta,\phi)\boldsymbol{P}\cdot\hat{\boldsymbol{n}}\right), \end{aligned} \tag{3.21}$$

where I_0 is incident photo current, R is the spin integrated scattering amplitude, θ and ϕ are the polar and azimuthal angles of the scattered electrons, respectively, $\hat{\boldsymbol{n}}$ is the scattering plane normal. In a kinematic model, the scattering cross section only depends on θ. In contrast, for low-energy scattering at the solid surface such as SP-LEED and an imaging spin filter, S and R depend on θ and ϕ due to multiple scattering [148].

3.3.2 Imaging spin filter

Up to now spin-resolved experiment have been extremely time-consuming because of the low efficiency of spin detectors and single-channel spin detection by which the spin at one energy and at only one momentum point (k_x, k_y) can be detected at a time [7]. These difficulties are overcome by combining momentum microscopy with an imaging spin filter, which enables parallel spin detection in the entire momentum image [6, 148].

The imaging spin filter is based on the spin-dependent specular reflection of low-energy electrons which is governed by SOC. The imaging spin filter is introduced into the electron optical path after the energy filter of the double hemispherical analyzer as shown in Fig. 3.4. The imaging spin filter can be inserted/retracted after the second analyzer from the beam path. The reciprocal/real-space image is formed at the scattering target such that every position of the images is encoded as a different scattering angle. Electrons are reflected from the target at an angle of 45°, corresponding to a central image point, with small deviations ±1.5° (off-center image points) as shown in Fig. 3.4. The image information is conserved upon the mirror-like specular reflection in the (00) LEED beam. Note that the obtained image is flipped upon the reflection with respect to the plane perpendicular to the scattering plane. The quantization axis $\boldsymbol{P}$ is aligned perpendicular to the scattering plane as we discussed in Sec. 3.3.1.

For the single-channel detector based on SOC, spin-polarized electrons scattered to the left and right are detected (see Fig. 3.7). For the imaging spin filter, right/left-scattered electrons can be detected by e.g., tilting the spin-filter crystal around 90° back and forth. Instead, we measure two different images at two different scattering energies. Though we need two detectors for the former way, for the latter way we need only one detector and thus we do not need to change the optical path.

The scattering amplitude depends on the scattering energy [152] such that we replace $I = I_{E_s}, S = S_{E_s}, R = R_{E_s}$ in eq. 3.21. As shown in Fig. 3.4, electrostatic decelerating and accelerating lenses before and after the scattering target allow the selection of the scattering energy E_s of the electrons. We need to know S_{E_s} and R_{E_s} in advance, and the property of the spin filter will be described later.

Here, we derive a general equation to obtain a spin-resolved image from eq. 3.21. The spatial coordinate (x, y) [the momentum coordinate (k_x, k_y)] is encoded in the corresponding angle (θ, ϕ). We replace $R(\theta, \phi)$, $P(\theta, \phi)$ by $R(x, y)$, $P(x, y)$. Only the component of the polarization vector $\boldsymbol{P}$ parallel to the scattering plane normal $\hat{\boldsymbol{n}}$ can be measured. Therefore, we write $P = \boldsymbol{P} \cdot \hat{\boldsymbol{n}}$. From eq. 3.21, we obtain intensities $I_{E_{s1}}$, $I_{E_{s2}}$ at two different scattering energies E_{s1}, E_{s2}:

$$I_{E_{s1}}(x, y) = I_0(x, y)\,(1 + S_{E_{s1}}(x, y)P(x, y))\,R_{E_{s1}}(x, y) \tag{3.22}$$

$$I_{E_{s2}}(x, y) = I_0(x, y)\,(1 + S_{E_{s2}}(x, y)P(x, y))\,R_{E_{s2}}(x, y) \tag{3.23}$$

Dividing eq. 3.22 by eq. 3.23, we obtain the spin polarization $P(x, y)$ and subsequently the spin-integrated incident photocurrent $I_0(x, y)$:

$$P(x,y) = \frac{\frac{I_{E_{s1}}(x,y)}{R_{E_{s1}}(x,y)} - \frac{I_{E_{s2}}(x,y)}{R_{E_{s2}}(x,y)}}{S_{E_{s1}}(x,y)\frac{I_{E_{s2}}(x,y)}{R_{E_{s2}}(x,y)} - S_{E_{s2}}(x,y)\frac{I_{E_{s1}}(x,y)}{R_{E_{s1}}(x,y)}} = \frac{\Gamma_{E_{s1}}(x,y) - \Gamma_{E_{s2}}(x,y)}{S_{E_{s1}}\Gamma_{E_{s2}}(x,y) - S_{E_{s2}}\Gamma_{E_{s1}}(x,y)}, \tag{3.24}$$

$$I_0(x,y) = \frac{S_{E_{s1}}(x,y)\frac{I_{E_{s2}}(x,y)}{R_{E_{s2}}(x,y)} - S_{E_{s2}}(x,y)\frac{I_{E_{s1}}(x,y)}{R_{E_{s1}}(x,y)}}{S_{E_{s1}}(x,y) - S_{E_{s2}}(x,y)} = \frac{S_{E_{s1}}\Gamma_{E_{s2}}(x,y) - S_{E_{s2}}\Gamma_{E_{s1}}(x,y)}{S_{E_{s1}}(x,y) - S_{E_{s2}}(x,y)}, \tag{3.25}$$

where $\Gamma_{E_s}(x,y) = \frac{I_{E_s}(x,y)}{R_{E_s}(x,y)}$ denotes the measured intensity at the scattering energy E_s normalized by the respective reflectively $R_{E_s}(x,y)$. The reflectively $R_{E_s}(x,y)$ can be obtained from an unpolarized electron image with homogeneous intensity. We measured a clean Cu(100) surface illuminated with unpolarized light from a mercury lamp in defocused condition [148]. As the spin sensitivity S is sufficiently constant over the image, we assume $S_{E_s}(x,y) = S_{E_s}$ [148].

Figure 3.8 demonstrates how we analyze the spin-resolved data. We first obtain the intensity $I_{E_s}(k_x,k_y)$ [Figs. 3.8(a, d)] measured on the $NiTe_2$ sample and the reflectively $R_{E_s}(x,y)$ [Figs. 3.8(c, f)] measured on a clean Cu(100) surface illuminated with a mercury lamp at two different scattering energies E_{s1}, E_{s2}. One can clearly find the different reflectively between E_{s1} and E_{s2} which originate from the spin-filter crystal. We then obtain the normalized intensity $\Gamma_{E_s}(k_x,k_y) = \frac{I_{E_s}(k_x,k_y)}{R_{E_s}(x,y)}$ [Figs. 3.8(b, e)]. Based on eqs. 3.24 and 3.25, we finally obtain the spin polarization $P(k_x,k_y)$ [Fig. 3.8(i)] and the spin-integrated total intensity $I_0(k_x,k_y)$ [Fig. 3.8(j)].

In this thesis, we utilized a W(100) spin-filter crystal. Figure 3.9 shows the spin sensitivity S and the spin-averaged reflectively R as function of the scattering energy [148]. One can determine working points, such that large difference of the spin sensitivity S at two different scattering energy and/or high reflective R are fulfilled. We utilize two working points in the scattering energy at $E_{s1} = 26.5$ eV and $E_{s2} = 30.5$ eV with a spin sensitivity of $S_{26.5\text{eV}} = 0.42$ and $S_{30.5\text{eV}} = 0.05$.

The well established procedure for preparation of the W(100) crystal leads to clean, carbon free surfaces [153]. Several cycles of low-power flash (1700 K) in 5×10^{-8} mbar O_2 atmosphere are performed followed by a final single high-power (2500 K) flash removing the oxide layer right before measurement. At a pressure of 1×10^{-10} mbar inside the spin-filter chamber during the measurements, the analyser-crystal could be used for 2 hours. Several hours after the high-power flash, a single low-power flash (without O_2) partially recovers W(100) surface and one can restart another set of the spin-resolved measurements for another 2 hours. We have used several low-power flash before repeating a time-consuming full preparation (several cycles of low-power flash with O_2 + high power flash).

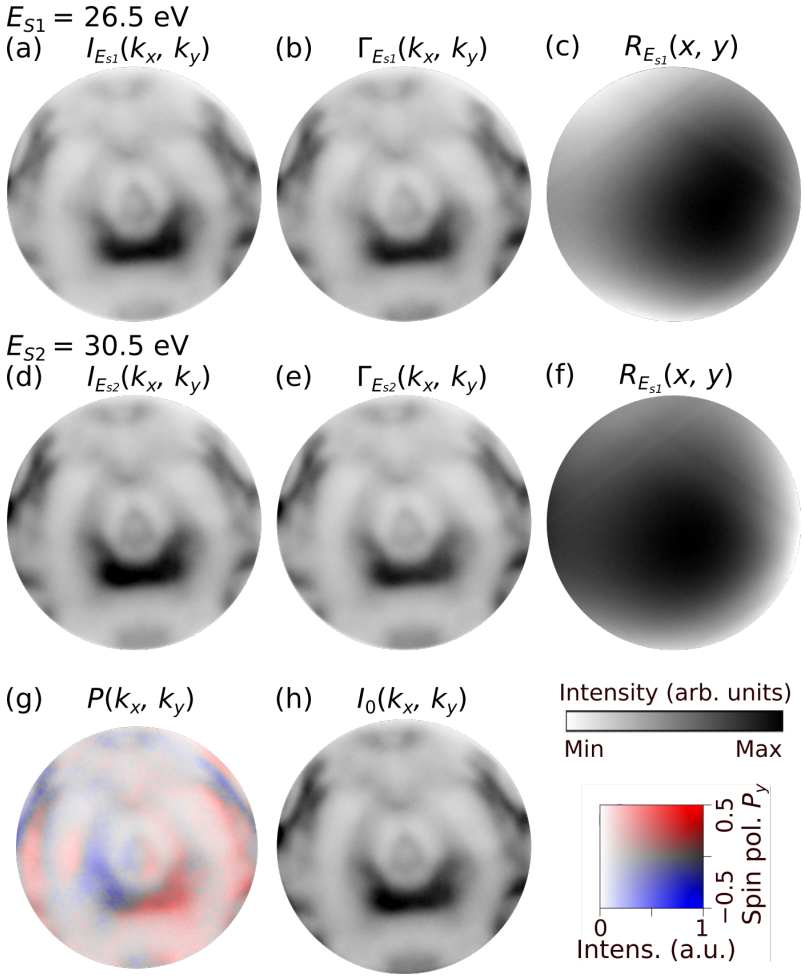

Figure 3.8: Analysis of the spin-resolved data of $NiTe_2$ measured using a W(100) spin filter. (a-c) Measurement at E_{s1} = 26.5 eV. (d-f) Measurement at E_{s1} = 30.5 eV. (a, d) Measured $I_{E_s}(k_x, k_y)$. (b, e) $\Gamma_{E_s}(k_x, k_y)$. (c, f) Measured $R_{E_s}(k_x, k_y)$. (g) Obtained $P(k_x, k_y)$. (h) Obtained $I_0(k_x, k_y)$.

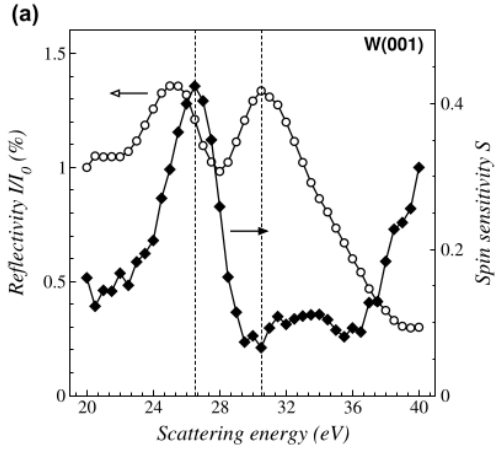

Figure 3.9: Properties of the spin-filter crystal of W(100). Spin averaged reflectivity I/I_0 and spin sensitivity S as a function of the electron scattering energy E_s. Working points are indicated by dotted lines at E_{s1} = 26.5 eV and E_{s2} = 30.5 eV. Data from [148]. Adapted from [126].

3.4 Polarization

3.4.1 Effect of the matrix element

The photoemisiion intensity distribution can be described by the matrix element as introduced in Sec. 3.1.3. Here, we demonstrate how we determine the orbital character of the initial state wave function $|\phi_i^{\boldsymbol{k}}\rangle$ by use of the optical polarization of the incident light $\boldsymbol{\epsilon}$. We assume that the final state $|\phi_f^{\boldsymbol{k}}\rangle$ is even with respect to mirror plane like a free electron (since odd-parity states are zero everywhere on the mirror plane). Any component of $\boldsymbol{\epsilon}$ orthogonal to the mirror plane has odd parity, while the component parallel to the mirror plane has even parity. Therefore, the parity of each term can be summarized as:

$$\left|M_{f,i}^{\boldsymbol{k}}\right| \propto \left|\langle\phi_f^k|\boldsymbol{\epsilon}\cdot\boldsymbol{r}|\phi_i^k\rangle\right| = \begin{cases} \langle+|+|+\rangle \neq 0 & \phi_i^{\boldsymbol{k}}:\text{even} \;\rightarrow\; \boldsymbol{\epsilon}:\text{even (p-polarization)} \\ \langle+|-|-\rangle \neq 0 & \phi_i^{\boldsymbol{k}}:\text{odd} \;\rightarrow\; \boldsymbol{\epsilon}:\text{odd (s-polarization)} \\ \langle+|+|-\rangle = 0 & \\ \langle+|-|+\rangle = 0 & \end{cases} \tag{3.26}$$

For p-polarization, which is the plane of polarization parallel to the mirror plane (see Fig. 3.10), only even orbital components of the initial state contribute to the photoemission intensity, while for s-polarization, which is the plane of polarization perpendicular to the mirror plane, only odd components contribute. Detectable orbitals in the case of the xz- and yz-mirror planes are summarized in Fig. 3.10.

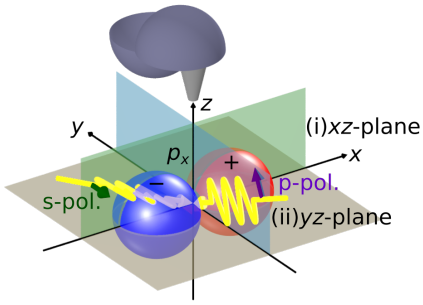

(i) Mirror plane: xz-plane

	p_x	p_y	p_z		
p-pol.	✓	-	✓		
s-pol.	-	✓	-		
	d_{xy}	d_{yz}	d_{zx}	$d_{x^2-y^2}$	d_{z^2}
p-pol.	-	-	✓	✓	✓
s-pol.	✓	✓	-	-	-

(ii) Mirror plane: yz-plane

	p_x	p_y	p_z		
p-pol.	-	✓	✓		
s-pol.	✓	-	-		
	d_{xy}	d_{yz}	d_{zx}	$d_{x^2-y^2}$	d_{z^2}
p-pol.	-	✓	-	✓	✓
s-pol.	✓	-	✓	-	-

Figure 3.10: Polarization-dependent photoemission probes orbital symmetry. The experimental geometry is indicated on the left hand side together with the p_x orbital as an example. The p_x orbital is even with respect to the xz-plane and odd with respect to the yz-plane. Purple and green arrows indicates the electric field vector ($\boldsymbol{E}$) for p- and s-polarized light, respectively. Detectable orbitals in the case of the xz- and yz-mirror planes are summarized on the right hand side. ✓: Allowed orbitals. -: Forbidden orbitals.

As we see now, differently polarized light probes specific orbital symmetries. This thesis aims to clarify the orbital texture of topologically non-trivial bands. Here, we see an application of polarization-dependent measurements to the prototypical type-I Weyl semimetal TaP. As shown in Fig. 3.11(a), TaP possesses 24 Weyl points in the first BZ [46–48]. Each Weyl point possess a chiral charge $C = \pm 1$. A projection onto the (001) surface gives rise to two inequivalent sets of projected Weyl points, W1 and W2. Since there are two W2 at the same k_z, the projected Weyl point W2 onto the (001) surface carries a chiral charge $C = \pm 2$. The Fermi surface of TaP(001) consists of the spoon-shaped feature α, the neck feature β, and the outer bowtie-shaped feature γ around the $\overline{\mathrm{X}}$ and $\overline{\mathrm{Y}}$ points as shown in Figs. 3.11(b, d). Ref. [154] assigned the state α to the surface Fermi arc, the state β to the bulk-like states, the state γ to the surface-like state. These three states are separated by the Weyl points W1 and W2. The two split Fermi arcs α terminate at the Weyl point W2. Since the number of the Fermi arcs corresponds to the chiral charge as a result of the the bulk-boundary correspondence (see Sec. 2.2.3), this observation is consistent with a chiral charge $C = \pm 2$ of the projected W2.

Photoemission-intensity maps excited by p- and s-polarized light exhibit different intensity variations for the different states, because different orbital symmetries contribute to the photoemission intensity. For s-polarized light [Fig. 3.11(b)], the state α along the $k_x = 0$ axis on the upper side and the state β along the $k_y = 0$ axis on

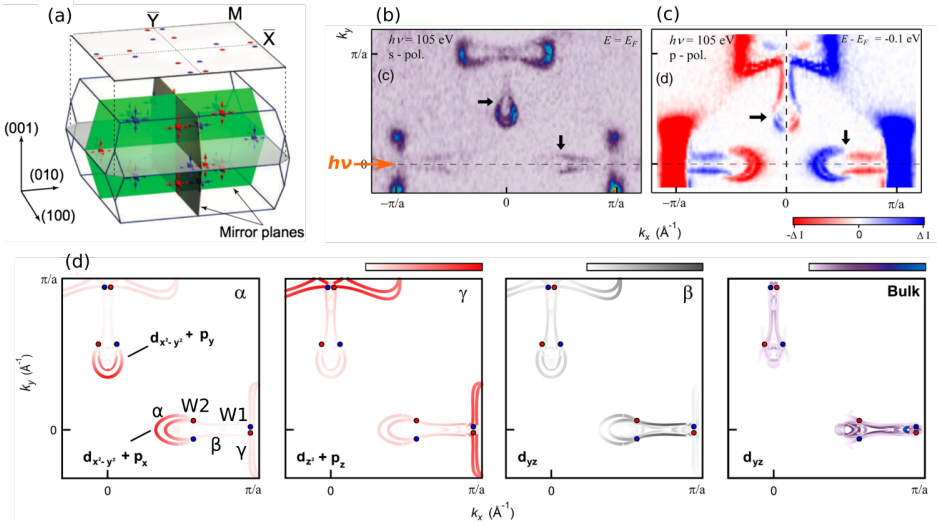

Figure 3.11: Orbital-resolved band structures in TaP(001) (a) Brillouin zone showing 24 Weyl points. (b) Photoemission-intensity maps obtained with s-polarized light. (c) Linear dichroism, defined as the intensity asymmetry $I(k_x, k_y) - I(-k_x, k_y)$, obtained from the measured intensity $I(k_x, k_y)$ with p-polarized light in panels (b). (d) Calculated Fermi surface projected onto different Ta $5d$ and P $3p$ orbitals derived from surface or bulk. α, β, and γ indicate the features and W1 and W2 indicate the projected Weyl points. (a) adapted from [15]. (b-d) adapted from [154].

the right hand side are pronounced. According to the calculated Fermi surface in Fig. 3.11(d), the state α along the $k_x = 0$ axis includes odd p_y orbital and the state α along the $k_y = 0$ axis mainly consists of odd d_{yz} orbital. The observation agrees with the fact that s-polarized light is sensitive to odd orbitals with respect to the xz optical mirror plane (see Fig. 3.10(i)). The different intensity variations for the α and β distinguish the topological Fermi arc α and the bulk-like states β, which are characterized by the different orbital symmetries [154]. The linear dichroism in Fig. 3.11(c) will be discussed in Sec. 3.4.3.

Next, we see orbital-dependent spin texture taking the Dirac-cone surface states as an example. The spin texture of the Dirac-cone surface states has been directly observed by spin-resolved ARPES [36]. Later several studies have reported that the measured photoelectron spin depends on the optical polarization of the exciting light [155–157].

Figures 3.12 (a-e) shows the most advanced observation of the spin texture of the Dirac cone in Bi_2Se_3 by spin-resolved momentum microscopy [158]. It clearly shows that the probed spin texture is reversed when using p- and s-polarized light. This is caused by a concept that different spin textures are locked to different orbitals as schematically shown in Fig. 3.12(f) [156, 157, 160]. This is a direct consequence of the

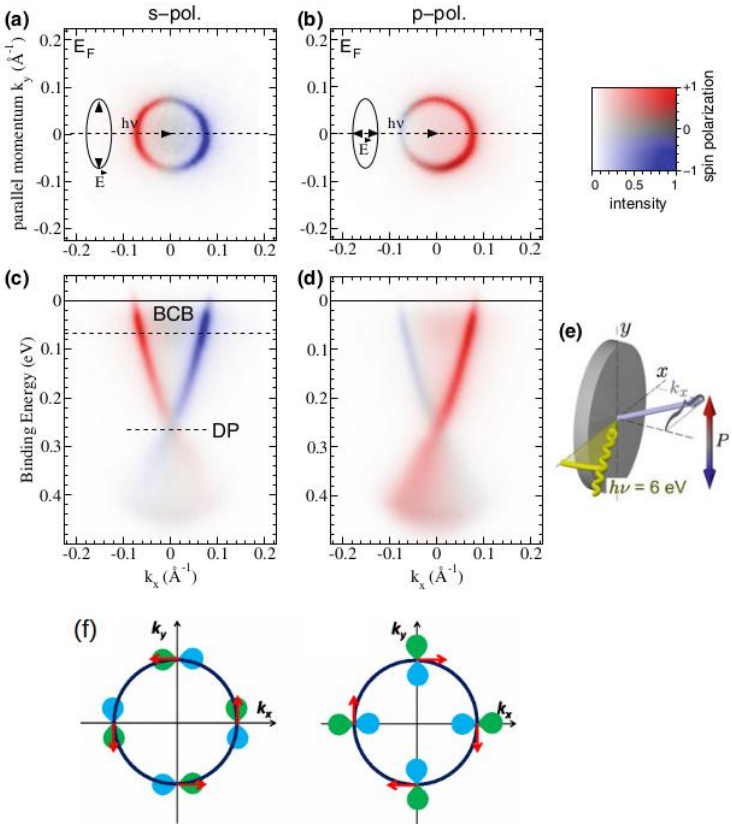

Figure 3.12: Orbital-dependent spin texture of the Dirac-cone surface sates. (a-e) Spin-resolved measurement of Bi_2Se_3 excited by s- (a, c) and p- (b, d) polarized light. Red, blue, and gray shaded intensities show the photoelectron spin polarization along the k_y in-plane direction according to the two dimensional color code and photoemission geometry displayed in panel (e). (f) Reversed spin texture upon different polarization is caused by a concept that different spin textures are locked to different orbitals. (a-e) adapted from [158]. (f) adapted from [159].

large SOC present in topological insulators. Note that the observation of a reversed photoelectron spin polarization for different light polarizations in topologically trivial materials such as BiTeI reveals that this effect is not due to topological protection, but large SOC [161]. An additional asymmetry of intensities and spin polarizations between the left and right half of the cone for p-polarized light is caused by the linear dichroism and will be discussed in Sec. 3.4.3.

Kuroda and Yaji et al. systematically measured the 3D spin polarization vector (P_x, P_y, P_z) of spin-orbit coupled surface states in Bi_2Se_3 and Bi(111) as a function

of the linear-polarization angle with respect to the incident mirror plane from p- to s-polarization [162, 163]. Since spin-orbit entanglement causes the wave function to be a coherent superposition of the spinor coupled to orbital components [159, 160, 164], they demonstrated that p- and s-polarized light can selectively excite the the fully spin-polarized photoelectron with spin-up or spin-down states and in other case the both states can be excited simultaneously due to spin-dependent interference in photoemission.

3.4.2 Circular dichroism

Circularly polarized light, which possesses a specific chirality itself, couples to chiral systems. In general, circular dichroism implies that the response of a chiral crystal to left and right circularly polarized is different. Circular dichroism in the angular distribution (CDAD) can be caused by not only a intrinsic chiral system but also a chirality that is induced by the handedness of the experimental setup [8, 165] as shown in Fig. 3.13. As shown in Fig. 3.14, circularly polarized light breaks the mirror symmetry of the incident plane, giving rise to a top-bottom asymmetry of the photoemission intensity. The CDAD signal I_{CDAD} is then obtained from the difference of photoemission intensities taken with right(I_{R})- and left(I_{L})-circularly polarized light in two separate measurements and thus defined as

$$I_{\mathrm{CDAD}}(k_x, k_y) = I_{\mathrm{R}}(k_x, k_y) - I_{\mathrm{L}}(k_x, k_y) : \text{ Definition (i).} \tag{3.27}$$

The CDAD asymmetry can be used for a quantification of the CDAD effect and is defined as

$$A_{\mathrm{CDAD}}(k_x, k_y) = \frac{I_{\mathrm{R}}(k_x, k_y) - I_{\mathrm{L}}(k_x, k_y)}{I_{\mathrm{R}}(k_x, k_y) + I_{\mathrm{L}}(k_x, k_y)}, \tag{3.28}$$

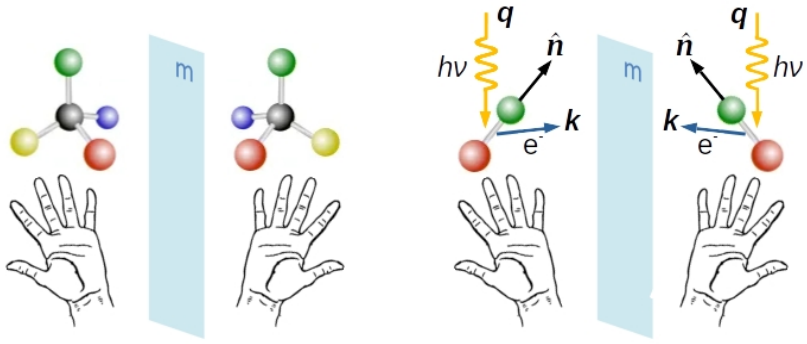

Figure 3.13: Natural handedness (left) and handedness induced by a dissymmetric experimental arrangement (right). The incoming light vector $\boldsymbol{q}$, the outgoing photoelectron momentum $\boldsymbol{k}$, and the surface normal $\hat{\boldsymbol{n}}$ define a handed coordinate system.

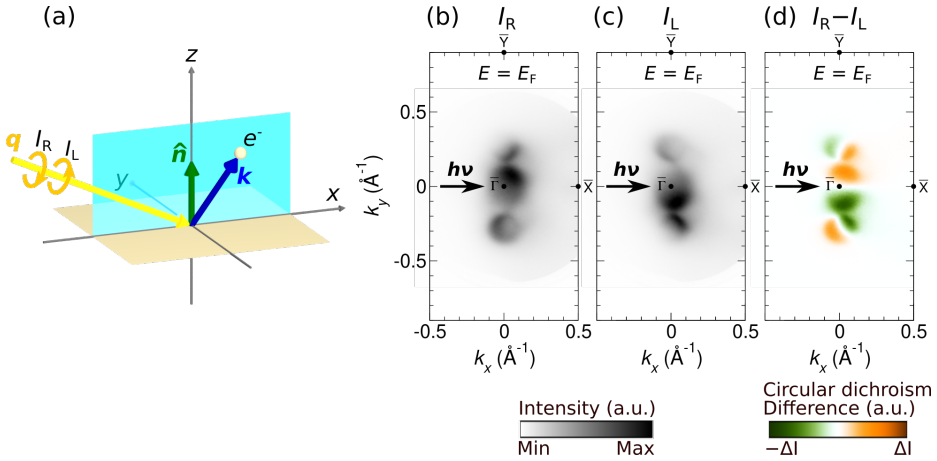

Figure 3.14: Circular dichroism in the angular distribution (CDAD) of $MoTe_2$. (a) Schematic illustration of experimental geometry indicating the incident mirror plane aligned in the xz-plane. (b-d) Fermi-surface contour obtained with right circularly polarized light I_R (b), left circularly polarized light I_L (c), $I_R - I_L$ (CDAD) (d). I_R and I_L maps exhibit a top-bottom asymmetry of the photoemission intensity and fulfill $I_R(k_x, k_y) = I_L(k_x, -k_y)$.

which varies between ±1.

In detail, the incoming light vector $\boldsymbol{q}$, the outgoing photoelectron momentum $\boldsymbol{k}$, and the surface normal $\hat{\boldsymbol{n}}$ define a handed coordinate system as shown in Fig. 3.13. We assume that the incoming light is in the $xz(yz)$-plane. Here, symmetry arguments allow the following general conclusions.

- The CDAD due to the experimental geometry vanishes at the $k_y = 0$ ($k_x = 0$) line along the incident plane, because all three vectors $\boldsymbol{q}$, $\boldsymbol{k}$, and $\hat{\boldsymbol{n}}$ lie in the same plane and thus cannot a define handedness.

- When the incident plane matches a crystal mirror plane, a result $\tilde{I}_R$, where tilde ˜ stands for mirrored experiment with respect to the incident plane, yields the identical result as the original experiment with reversed circularly polarized light I_L, since the mirror operation reverses the photon helicity, i.e., $\tilde{I}_R(k_x, k_y) = I_L(k_x, k_y)$. Thus, we obtain

$$I_R(k_x, k_y) = I_L(k_x, -k_y) \ (xz \text{ mirror plane}) \tag{3.29}$$
$$(I_R(k_x, k_y) = I_L(-k_x, k_y) \ (yz \text{ mirror plane})), \tag{3.30}$$

  where $I_{CDAD}(k_x, k_y) = I_R(k_x, k_y) - I_L(k_x, k_y)$ is an odd function of k_y (k_x). The CDAD should be anti-symmetric with respect to the incident plane.

In this case, the CDAD can be obtained in another way in a single measurement without helicity reversal as

$$I_{\mathrm{CDAD}}(k_x, k_y) = I_{\mathrm{R}}(k_x, k_y) - I_{\mathrm{R}}(k_x, -k_y) : \text{ Definition (ii).} \tag{3.31}$$

Further studies with detailed calculation of the dipole transition matrix element $\left|M^{\boldsymbol{k}}_{f,i}\right| \propto \left|\langle\phi^k_f|\boldsymbol{\epsilon}\cdot\boldsymbol{r}|\phi^k_i\rangle\right|$ in eq. 3.15 suggests that CDAD probes the orbital part of the wave function [8, 165] and is related to the orbital angular momentum [166].

We aim to capture a topological signature, which is related to the orbital degree of freedom of the electronic states. A fingerprint of the Weyl points and the associated chiral Dirac states can be obtained through the CDAD measurement. Previous studies have reported the CDAD accesses the orbital angular momentum or the Berry curvature of Dirac cones in graphene [167, 168] and topological insulators [169, 170], and of valleys in TMDCs [171, 172]. Recently, this attempt has been applied to Weyl semimetals, demonstrating that momentum mapping of the orbital angular momentum reflects the Berry curvature field describing the Weyl nodes [173].

Figure 3.15 shows the orbital- and spin angular momentum, and the Berry curvature field of the type-I Weyl semimetal TaAs. Broken space-inversion symmetry and SOC induces a spin splitting into non-degenerate band branches $v_\pm$ and $c_\pm$ due to the

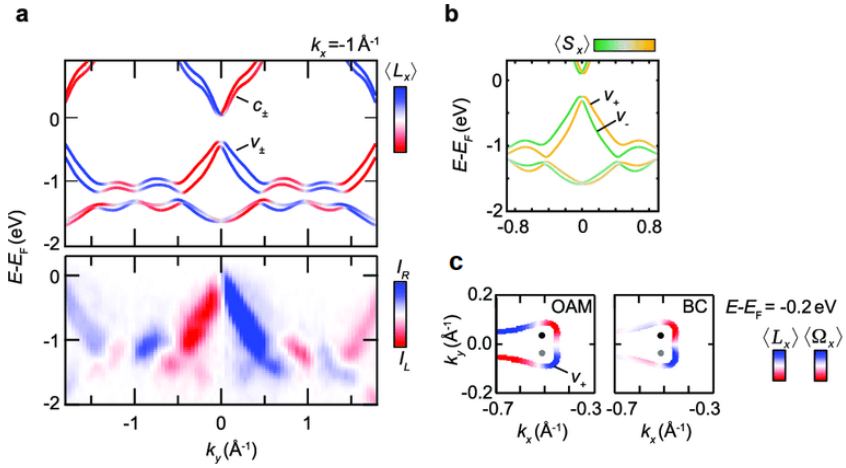

Figure 3.15: Orbital and spin angular momentum, and Berry curvature field of the type-I Weyl semimetal TaAs. (a) Calculated bulk band dispersion projected onto the orbital angular momentum L_x (top) and corresponding measured band dispersion for the circular dichroim (bottom). (b) Calculated bulk band dispersion projected onto the spin angular momentum S_x. (c) Momentum maps of the orbital angular momentum L_x and the Berry curvature Ω_x slightly below an energy of the Weyl node W2 (black points). Adapted from [173].

Kramers theorem (see Sec. 2.3.1). The spin-split branches $v_\pm$ and $c_\pm$ carry parallel orbital angular momentum (Fig. 3.15(a)), while antiparallel spin angular momentum (Fig. 3.15(b)). Ref. [173] further confirmed this experimentally by performing CDAD and spin-resolved photoemission. The CDAD signal can be shown to be approximately proportional to the projection of the orbital angular momentum $\boldsymbol{L}$ on the light propagation direction [166, 169, 173]. In this experimental geometry, where the light is incident along the x direction, the CDAD signal predominantly reflects the L_x component of the orbital angular momentum. A comparison of the measured CDAD and the L_x of band structure shows a good agreement. As indicated in Fig. 3.15(c), momentum maps of the orbital angular momentum L_x and the Berry curvature Ω_x are closely related. Sign changes of the L_x and the Ω_x close to the Weyl nodes reveal the topological nontrivial winding of the wave function.

3.4.3 Linear dichroism

Circular polarized light breaks the mirror symmetry of the incident plane and gives rise to an asymmetries of the intensities as shown in Fig. 3.14. In the same analogy, a finite E_z component of the electric field vector, e.g, linearly p-polarized light, breaks the mirror symmetry and gives rise to an asymmetry of the intensities. This asymmetry reflects the linear dichroism in the angular distribution (LDAD) [174, 175]. We assume that the incidence of p-polarized light is in the yz-plane (see Fig. 3.16(a)). The tilted electric field vector $\boldsymbol{E}$ aligned in the same plane breaks the symmetry of the xz-plane, i.e., the orthogonal plane to the incident mirror plane. This causes a top-bottom asymmetry of the intensity as shown in Fig. 3.16(b). The term "dichroism" here refers to the different response of a system to p-polarized light coming from $-k_y$ and $+k_y$ directions at a definite angle (see Fig. 3.16(a)). $E_{z,\mathrm{p}}$ ($E'_{z,\mathrm{p}}$) and I_p (I'_p) are the electric field vector and measured intensity with p-polarized light coming from $-k_y$ ($+k_y$). Thus, the LDAD signal I_LDAD is determined as

$$I_\mathrm{LDAD}(k_x, k_y) = I_\mathrm{p}(k_x, k_y) - I'_\mathrm{p}(k_x, k_y) : \text{ Definition (i).} \tag{3.32}$$

We consider that mirror operation with respect to the xz-plane converts $E_{z,\mathrm{p}}$ to $E'_{z,\mathrm{p}}$. Therefore, the LDAD signal I_LDAD is evaluated in another way from a single measurement $I(k_x, k_y)$ as

$$I_\mathrm{LDAD}(k_x, k_y) = I_\mathrm{p}(k_x, k_y) - I_\mathrm{p}(k_x, -k_y) : \text{ Definition (ii),} \tag{3.33}$$

where $I_\mathrm{p}(-k_x, k_y)$ is the reversed intensity map with respect to the xz-plane. The LDAD asymmetry is defined as

$$A_\mathrm{LDAD}(k_x, k_y) = \frac{I_\mathrm{p}(k_x, k_y) - I_\mathrm{p}(k_x, -k_y)}{I_\mathrm{p}(k_x, k_y) + I_\mathrm{p}(k_x, -k_y)}. \tag{3.34}$$

Note that Definition (ii) includes information on the broken mirror symmetry due to not only the incident light but also the crystal structure as described in detail in Sec. 5.2.

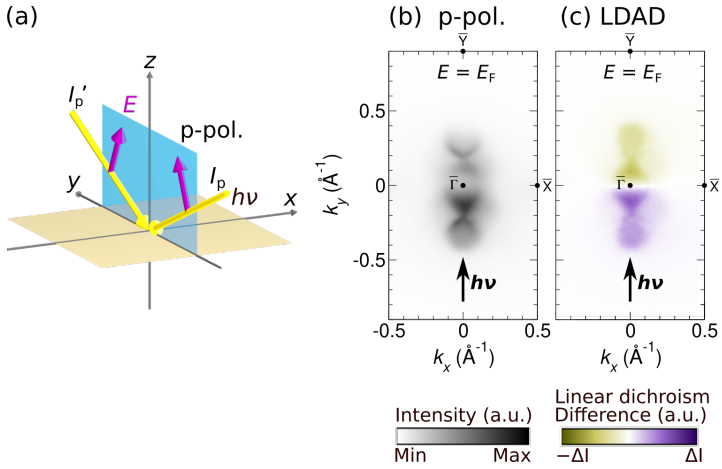

Figure 3.16: Linear dichroism in the angular distribution (LDAD) of $MoTe_2$. (a) Schematic illustration of experimental geometry indicating the incident mirror plane aligned in the yz-plane. (b) Fermi-surface contour obtained with p-polarized light I_p showing a top-bottom asymmetry of the photoemission intensity. (c) Corresponding map of $I_{LDAD}(k_x, k_y) = I_p(k_x, k_y) - I_p(k_x, -k_y)$.

The LDAD and CDAD reflect the handedness of the experiment and give similar information on the orbital part of the wave function except for a phase factor [174].

An application of the LDAD to the type-I Weyl semimetal TaP is indicated in Fig. 3.11(c). The measured LDAD $I(k_x, k_y) - I(-k_x, k_y)$ map clearly shows a sign reversal between the topological Fermi arc α and the bulk-like states β at the Weyl point W2 as indicated by black arrows. Note that the LDAD does not directly reflect a specific orbital. These complement measurements together with p- and s-polarized light clarified pronounced switches in the orbital texture at the projected Weyl points [154], reflecting the different orbital character of the topological Fermi arc and the bulk-like states.

Next, we discuss the LDAD effect of spin polarization taking the Dirac-cone surface states as an example. As shown in Figs. 3.12(b, d), for p-polarized light, one can find an additional asymmetry of intensities and spin polarizations between the left and right half of the cone due to the LDAD. This asymmetry in the spin-polarization can be attributes to a different LDAD for spin-up and spin-down states, and shows that these spin-states can be locked to different orbitals [158].

3.5 NanoESCA beamline

We performed all experiments at the NanoESCA beamline [176] of the Elettra Synchrotron in Trieste, Italy, operated by PGI-6, Forschungszentrum Jülich. A commercial momentum microscope (NanoESCA) with a aberration compensated double hemispherical analyzer [131, 134] is available there, with some modifications. It is equipped with a W(100) imaging spin filter. Dual APPLE-II type undulators with phase modulation electromagnet in the beamline provide a wide range of photon energies between 25 eV and 1000 eV with lineally and circularly polarized light. The beam spot size is focused to around 10 μm (V) × 20 μm (H). We confirmed the beam spot size from a PEEM image as indicated in Fig. 3.5(c). The energy resolution of the analyzer can reach 100 meV. The sample stage can be cooled down at $T \sim 100$ K using liquid nitrogen and at $T \sim 30$ K using liquid helium. The NanoESCA beamline is equipped with the *in-situ* preparation chamber including a sample heating stage (annealing system), a sputter gun, a low energy electron diffraction (LEED), Auger electron spectroscopy (AES), and a metal evaporation system, which provides the complete surface cleaning and preparation system.

4 Type-II Dirac semimetal $NiTe_2$

4.1 Sample preparation

The crystal of $NiTe_2$ was mounted on the sample plate with silver epoxy and the plate was attached to the sample holder as shown in Fig. 4.1(a). Dr. Raman Sankar at Prof. Fang-Cheng Chou's group, National Taiwan University synthesized high-quality single crystals of $NiTe_2$ as described in Ref. [80] and provided them as a collaborative project. Since the layered 2D nature of $NiTe_2$ offers a natural cleaving plane (see Sec. 2.4.5), we cleaved the crystal *in situ* at room temperature using a carbon tape as shown in Fig. 4.1(b). As shown in Fig. 4.1(c), we succeeded in obtaining a low energy electron diffraction (LEED) pattern after cleavage, suggesting a clean sample surface. We measured them in an ultrahigh vacuum of better than ~ 10^{-10} Torr. All measurements were performed while keeping the sample at T ~ 100 K. Before the momentum microscope measurements, the best sample region was selected by using photoemission electron microscopy (PEEM) as described in Fig. 3.5.

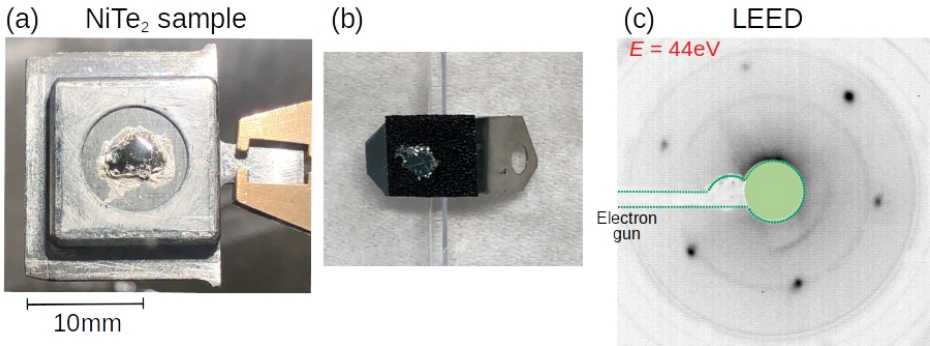

Figure 4.1: (a) $NiTe_2$ sample on the sample holder. (b) We cleaved the sample using a carbon tape. (c) Low energy electron diffraction (LEED) pattern measured with an electron beam energy of 44 eV showing sharp spots.

4.2 Fermi surface tomography

To construct the 3D Fermi surface of $NiTe_2$, we have performed photon-energy-dependent measurements in the energy range between 48 eV and 132 eV as shown in

Fig. 4.2. This measurement enables us to determine specific photon energies which can access the high-symmetry points from symmetry of a shape of the observed bands as described later. 2D momentum discs shows tomographic sections through the 3D BZ in reciprocal space as indicated in Fig. 4.2(a). These disks are described by eq. 3.8 as a constant-energy sphere in k space, and the perpendicular momentum component ($k_\perp$) is selected by the photon energy. We performed a band structure calculation in collaboration with Dr. Philipp Rüßmann at Peter Grünberg Institut (PGI-1), Forschungszentrum Jülich. Density functional theory (DFT) calculations were carried out within the local spin density approximation [177] using the full-potential relativistic Korringa-Kohn-Rostoker Green's function method (KKR) [178, 179] with exact description of the atomic cells [180, 181]. The 3D Fermi surface

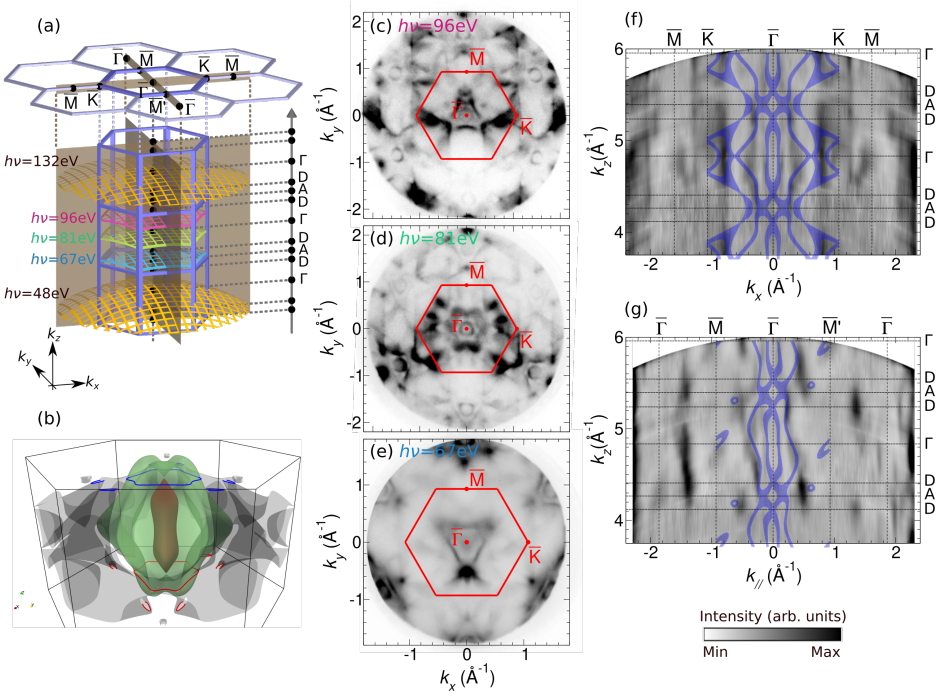

Figure 4.2: Fermi surface tomography. (a) Bulk and surface Brillouin zone together with the corresponding 2D momentum discs measured at several photo energies as indicated by the spherical section. (b) Calculated 3D Fermi surface. (c-e) Measured Fermi-surface contour at a photon energy of $h\nu = 96$ eV (c), 81 eV (d), and 67 eV (e). High symmetry points of the surface Brillouin zone are indicated by the corresponding labels. (f, g) k_z dispersion maps at E_F along $\overline{M} - \overline{K} - \overline{\Gamma} - \overline{K} - \overline{M}$ (f) and $\overline{\Gamma} - \overline{M} - \overline{\Gamma} - \overline{M'} - \overline{\Gamma}$(g) indicated by dark orange orthogonal planes in panel (a). Dark blue lines indicate calculated bulk bands.

exhibits a three-fold and space-inversion symmetry reflecting the symmetry of the crystal structure (see Fig. 2.10(b)). Figure 4.2(b) shows Fermi surface contours at the top and bottom D points ($k_z = \pm 0.75\frac{\pi}{c}$) between the Γ and A points (see Fig 2.10(c) or Fig 4.2(a)) indicated by red and blue contours, respectively, demonstrating that the direction of the contour is reversed.

A Fermi surface contour obtained at $h\nu = 81$ eV [Fig. 4.2(d)] cutting through the high symmetry Γ point is characterized by a flower-like shape with six-fold symmetry centered at the BZ center. Fermi surfaces contour obtained at $h\nu = 96$ eV [Fig. 4.2 (c)] and 67 eV [Fig. 4.2(e)] cutting through the top and bottom D point demonstrate a triangle-like contour with three-fold symmetry. The direction of the triangle contour obtained at both photon energies is reversed, which is consistent with the calculated 3D Fermi surface. The reversal is required by space-inversion symmetry of the crystal structure. Our result is the first experimental observation of the full 3D Fermi surface in the type-II Dirac semimetal 1T-MX_2.

Figures 4.2(f, g) show k_z dispersion maps at E_F along the $\overline{M} - \overline{K} - \overline{\Gamma} - \overline{K} - \overline{M}$ (f) and $\overline{\Gamma} - \overline{M} - \overline{\Gamma} - \overline{M'} - \overline{\Gamma}$ (g) directions indicated by dark orange orthogonal planes in Fig. 4.2(a). The photon energy $h\nu$ is converted to k_z based on eq. 3.9. From the photon energy scan measurement, we found best agreement to the calculated band structure by taking an inner potential $U_i = 9.5\text{eV} + \phi$. Here, the inner potential was determined from an energy offset between an experimental kinetic energy at the high symmetry point $E_{kin} = h\nu - \phi$ and an energy at the corresponding high symmetry k_z $E_{kin} + U_i = \frac{\hbar k_z^2}{2m}$.

As described in Fig. 2.10(a), appearance of the boundary between hole and electron pockets together with the Dirac point at E_D is a solid signature of the strongly titled Dirac cone in the type-II Dirac semimetal $NiTe_2$. As we can see from the calculated 3D Fermi surface in Fig 4.2(b), a dark orange colored hole pocket and a green colored electron pocket touch at the Weyl point. As shown Figs. 4.2(f, g), one observes an inner ellipse-like electron pocket centered at $(k_\parallel, k_z) = (\overline{\Gamma}, \Gamma)$, as clearly recognized from calculated bulk bands indicated by dark blue lines. This electron pocket corresponds to the orange electron pocket in Fig. 4.2(b). Above and below the electron pocket, one finds the Dirac points at $(k_\parallel, k_z) = (\overline{\Gamma}, D)$ and adjacent hole pockets.

The observed band dispersions should fulfill a 3-fold and space-inversion symmetry expected from the crystal symmetry described in Sec. 2.4.5. Fermi surface sections are symmetry with respect to the $k_x = 0$ line, i.e., the $\overline{\Gamma} - \overline{M} - \overline{\Gamma} - \overline{M'} - \overline{\Gamma}$ direction, which corresponds to the axis of the 3-fold symmetry, as seen from Figs. 4.2(c-e). The k_z dispersions at E_F along $\overline{M} - \overline{K} - \overline{\Gamma} - \overline{K} - \overline{M}$ [Fig. 4.2(f)], corresponds to a section parallel to the mirror plane, exhibits symmetry with respect to the $k_x = \overline{\Gamma}$ line. The k_z dispersions at E_F along $\overline{\Gamma} - \overline{M} - \overline{\Gamma} - \overline{M'} - \overline{\Gamma}$ [Fig. 4.2(g)] exhibits asymmetry with respect to the $k_\parallel = \overline{\Gamma}$ and $k_z = \Gamma$ lines. Measured sections through the Fermi surface show an overall good agreement with calculated ones and the expected symmetries.

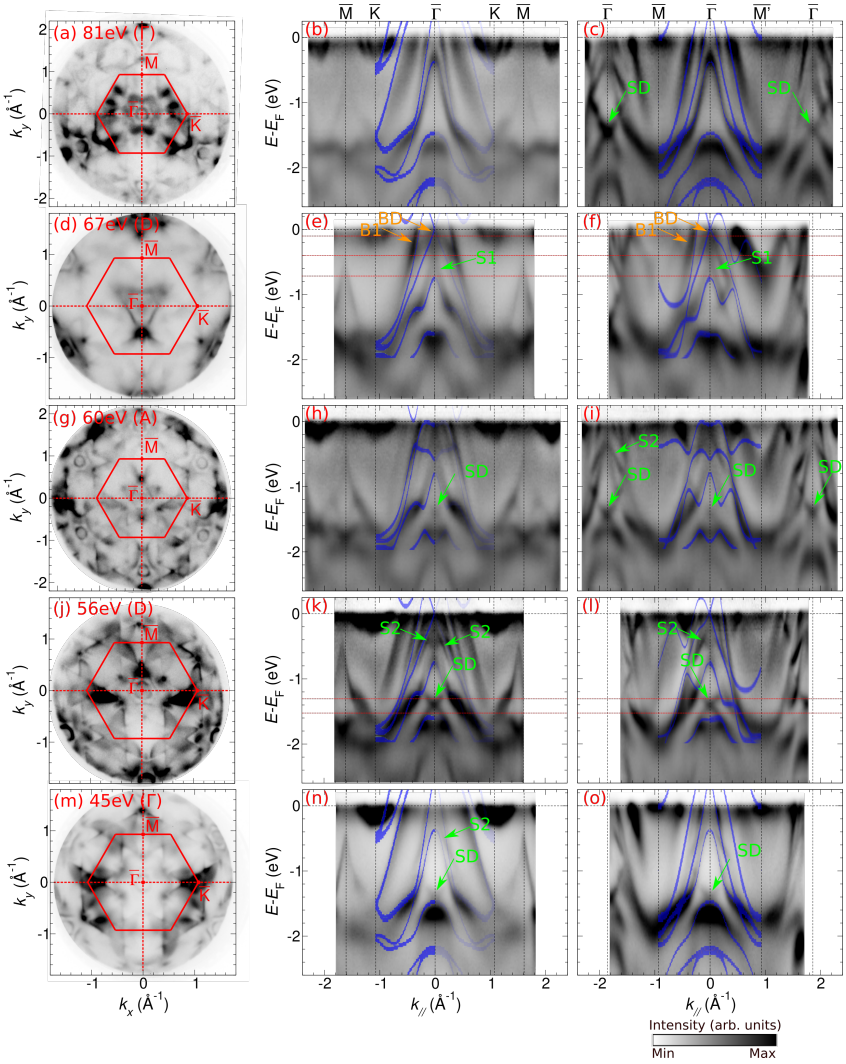

Figure 4.3: Band structures at the high symmetry (Γ, A) and the Dirac (D) points. Measured Fermi-surface contours (a, d, g, j, m) and band dispersions along the $\overline{\mathrm{M}}$ – $\overline{\mathrm{K}}$ – $\overline{\Gamma}$ – $\overline{\mathrm{K}}$ – $\overline{\mathrm{M}}$ (b, e, h, k, n) and $\overline{\Gamma}$ – $\overline{\mathrm{M}}$ – $\overline{\Gamma}$ – $\overline{\mathrm{M}'}$ – $\overline{\Gamma}$ (c, f, i, l, o) directions measured at a photon energy of $h\nu$ = 81 eV (Γ) (a-c), 67 eV (D) (d-f), 60 eV (A) (g-i), 56 eV (D) (j-l), 45 eV (Γ) (m-o) with p-polarized light are indicated. Corresponding momentum sections for the band dispersions are indicated by red dotted lines on the Fermi-surface contours and dark orange orthogonal planes on the surface BZ in Fig. 4.2(a). BD and B1 represent the bulk Dirac cone and the bulk state B1, respectively, indicated by orange arrows. SD, S1, and S2 represent the surface Dirac cone, the surface states S1 and S2, respectively, indicated by green arrows. Red dotted lines in panels (e, f, k, l) indicate binding energies where we display spin-resolved results in Figs. 4.6 and 4.7.

4.3 Band structure

We measured band-dispersions at the high symmetry (Γ and A) and the Dirac (D) points as shown in Fig. 4.3. We display measured Fermi-surface countours and band dispersions along the $\overline{\mathrm{M}}-\overline{\mathrm{K}}-\overline{\Gamma}-\overline{\mathrm{K}}-\overline{\mathrm{M}}$ and $\overline{\Gamma}-\overline{\mathrm{M}}-\overline{\Gamma}-\overline{\mathrm{M}'}-\overline{\Gamma}$ directions from left to right. Corresponding momentum sections for the band dispersions are indicated by red dotted lines on the Fermi-surface contours. Since the bulk Dirac cone disperses in 3D momentum space, the up-right Dirac cone appears only at the D point. One can find the Dirac cone centered at the $\overline{\Gamma}$ point near E_{F}, annotated by a orange arrow with label BD [Figs. 4.3(e, f)]. One can also observe a hole-like band outside the B1 band indicated by a orange arrow labeled B1. The B1 band actually develops from the flower-like into the triangle-like contour as a function of k_z as seen in Fig. 4.2. We find an overall agreement of measured band dispersions with the calculated bulk bands indicated by blue lines. Note that one can not find a clear signature of the up-light bulk Dirac cone at $h\nu = 56$ eV (D point) probably because the bulk states are suppressed and the surface states are enhanced due to matrix-element effects.

Now we take a look at the surface states. One can observe the surface Dirac cone with the Dirac point at $E \sim E_{\mathrm{F}} - 1.4$ eV at the $\overline{\Gamma}$ point, indicated by orange arrows labeled SD in Fig. 4.3. One can also find that the photoemission intensity of the surface Dirac cone is modulated as a function of the photon energy. It is most pronounced at $h\nu = 56$ eV [Figs. 4.3(k, l)], and is suppressed and almost vanishes at $h\nu = 67$ eV and 81 eV. Interestingly, even when the surface Dirac cone disappears at the first BZ, one can find the surface Dirac cone with pronounced intensity at the second BZ, e.g., measured at $h\nu = 60$ eV [Fig. 4.3(i)] and 81 eV [Fig. 4.3(c)]. Such phenomena that a certain band dispersion is suppressed in a certain BZ, whereas it is clearly observed in the next BZ have been often experimentally reported. This can also be related to matrix-element effects, which so far has not been theoretically

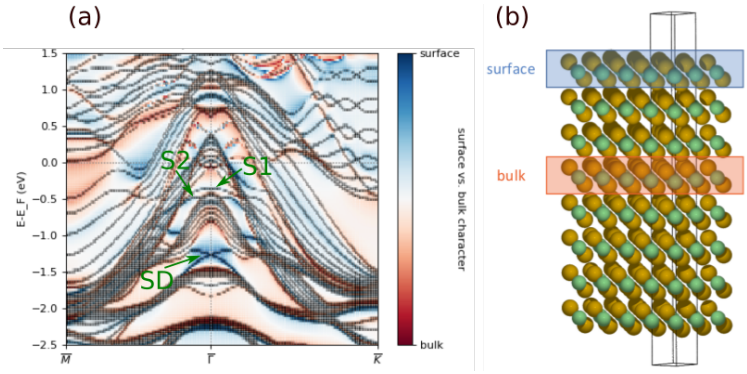

Figure 4.4: Bulk and surface character of the bands obtained by the thin film calculation. (a) Band dispersion showing the surface and bulk character according to the blue and red color code on the right hand side. (b) We used an 8 trilayers film model.

calculated [126]. In addition to the surface Dirac cone, several other surface states are present. For instance, the surface state S1 is indicated in band-dispersion maps measured at $h\nu = 67$ eV and S2 at $h\nu = 45$ eV and 56 eV. The SD, S1, and S2 states are consistent with previous ARPES and theoretical studies [81, 82].

To identify the surface and bulk origin of the bands, we performed a thin film calculation for an 8 trilayer film of $NiTe_2$ as shown in Fig. 4.4. We define a localization of the states $X = \dfrac{n^{1^{st}} - n^{mid}}{n^{1^{st}} + n^{mid}}$, where $n^{1^{st}}$, n^{mid} are the integrated densities within the 1^{st} and 4^{th} (i.e, middle) trilayer in the film, respectively. The localization of the states X gives the surface and bulk character according to the blue and red color code on the right hand side in Fig. 4.4(a). The observed SD, S1, and S2 bands indicated by green arrows are well reproduced by the calculation.

Next, we focus on the Bulk Dirac cone. Figure 4.5 shows the energy development of momentum sections measured at a photon energy of $h\nu = 67$ eV (D point). One can see that the triangle-like B1 band indicated by yellow arrows becomes bigger towards deeper binding energies. Inside the B1 band, the bulk Dirac cone with the Dirac point near E_F develops into a star-like triangle pocket BD clearly seen at $E = E_F - 0.4$ eV. We find a good agreement of the observed B1 and BD bands with bulk band calculation indicated by dark blue lines at $E = E_F, E_F - 0.5$ eV. Inside the bulk Dirac cone, one can find a circular contour developing from $E = E_F - 0.4$ eV and clearly seen at $E = E_F - 0.7$ eV, which corresponds to the S1 band. Our calculation clarified that

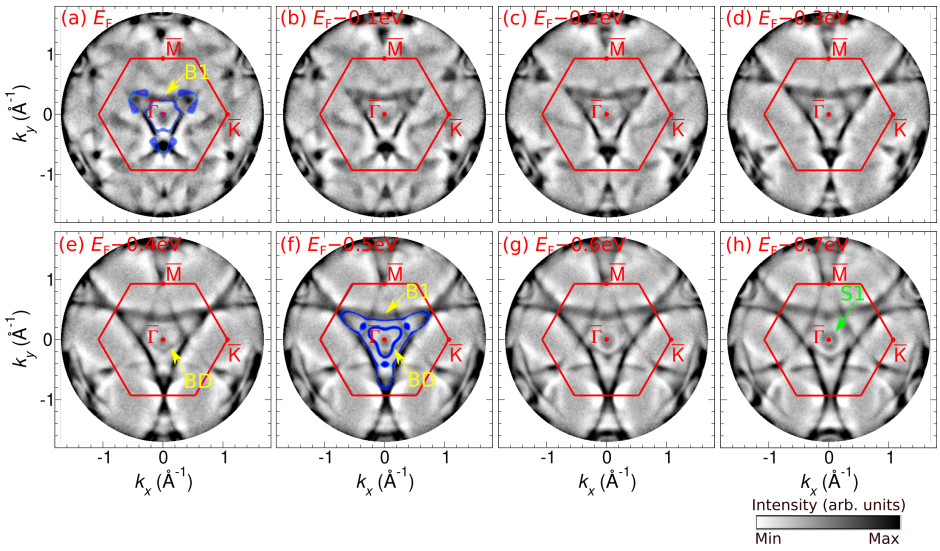

Figure 4.5: Energy development of momentum distribution of photoemission intensity measured at a photon energy of $h\nu = 67$ eV (D point) with p-polarized light. Dark blue lines indicate the calculated bulk bands.

bulk-derived states exhibit a three-fold symmetry at the off-high-symmetry point, while surface-derived states exhibit a six-fold symmetry, since surface states can be understood as projection of all k_z in the BZ.

4.4 Spin texture

Figure 4.6 shows a spin-resolved measurement of the surface Dirac cone. For the spin-resolved measurements, the spin quantization axis $\boldsymbol{P}$ points in-plane along the positive k_y axis. The spin-resolved momentum map recorded slightly above the surface Dirac point in Fig. 4.6(a) shows characteristic spin-momentum locking of a inner circular contour centered at the $\overline{\Gamma}$ point with directly opposite P_y-spin-polarization (blue and red colors) for the positive and negative k_x. Below the surface Dirac point, the inner circular contour demonstrates a reversed spin polarization as clearly seen in Fig. 4.6(b). Though the spin texture of the surface Dirac cone in $PdTe_2$ has been observed [75], this observation gives clear evidence for a helical spin-polarized surface Dirac cone in $NiTe_2$ for the first time. Since the surface Dirac cone in the type-II Dirac semimetal $1T$-MX_2 is formed by band inversion with non-trivial Z_2 topological order [74, 75] as in topological insulators (see Sec. 2.4.5), the helical spin-polarized surface Dirac cone is predicted.

Figure 4.7 shows a spin-resolved measurement of the bulk Dirac cone and related features. One can see that the BD, B1, and S1 bands are spin polarized. All bulk bands, however, must be spin degenerate in non-magnetic materials, which naturally preserves time-reversal symmetry, with space-inversion symmetry due to the Kramers

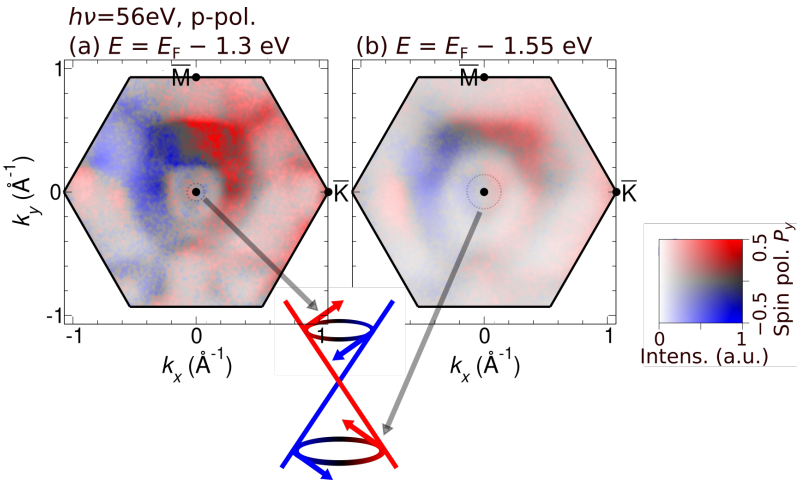

Figure 4.6: Spin texture of the surface Dirac cone. (a, b) Measured constant-energy maps at $E = E_F - 1.3$ eV (a), $E_F - 1.55$ eV (b) at a photon energy of $h\nu = 56$ eV. A lower inset illustrates the spin texture of the surface Dirac cone.

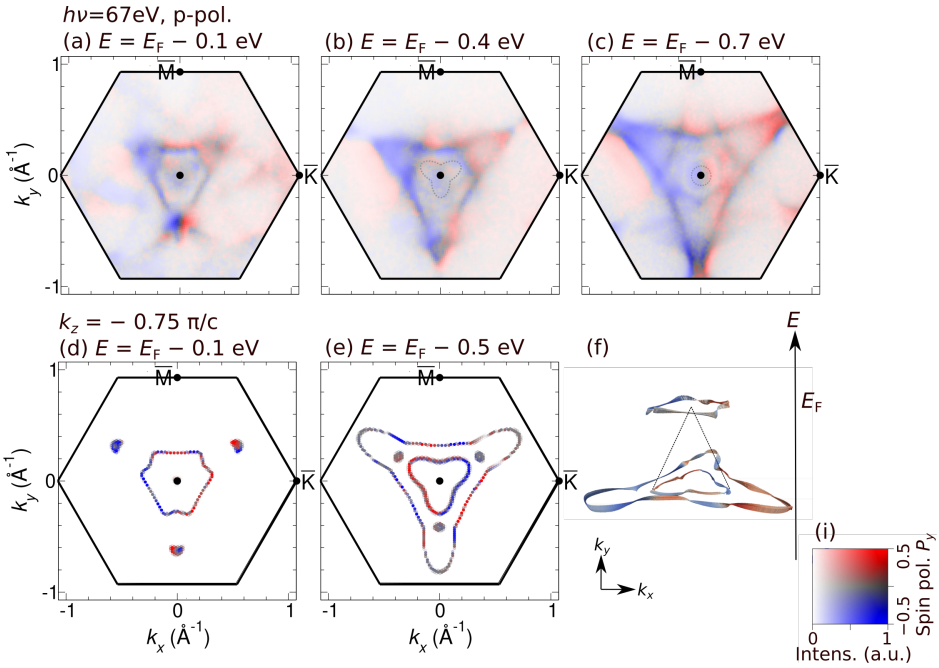

Figure 4.7: Spin texture of the bulk Dirac cone. (a-c) Measured constant-energy maps at $E = E_F - 0.1$ eV (a), $E_F - 0.4$ eV (b), $E_F - 0.7$ eV at a photon energy of $h\nu = 67$ eV cutting through the D point. (d, e) Calculated spin-polarized bulk bands in the top Te layer for the y component at $E = E_F - 0.1$ eV (d), $E_F - 0.5$ eV (e) at $k_z = -0.75\frac{\pi}{c}$ (D point). (f) Schematic 3D spin texture of the bulk Dirac cone and the related features in (E, k_x, k_y) space.

theorem described in Sec. 2.3.1. Therefore, the observed spin polarization of the BD and B1 bands are unexpected. Thus, previous studies on the type-II Dirac semimetal 1T-MX_2 only focused on the spin texture of the surface states [75, 81, 82]. The observed "hidden" spin polarization of the bulk bands originates from the top Te layer of a Te-Ni-Te trilayer due to broken inversion symmetry at the surface probed by surface sensitive VUV light, which will be described in detail in Sec. 7.2.

Figures 4.7(d, e) shows calculated spin-polarized bulk bands in the top Te layer at $k_z = -0.75\frac{\pi}{c}$ (D point). The color code gives the y-component of the spin polarization. We find a good agreement of the observed spin texture with calculated one. The observed P_y spin texture is anti-symmetric with respect to the $k_x = 0$ axis i.e, $P_y \rightarrow -P_y$ upon the mirror operation $k_x \rightarrow -k_x$. In general, mirror operation with respect to the mirror plane of three-fold symmetry reverses the spin component parallel to the corresponding plane, as clearly seen in the calculation. Figure 4.7(f) schematically illustrates 3D spin texture of the bulk Dirac cone and the related features in (E, k_x, k_y)

space. Vectors at each momenta indicate direction of the spin polarization. The color code gives the y-component of the spin polarization as in Fig. 4.7(d, e). One can find a complicated spin texture developing in 3D.

4.5 Summary

By preforming photon-energy dependent measurements, for the first time we succeeded in capturing the full 3D Fermi surface, which reflects the three-fold and space-inversion symmetry of the crystal structure. Together with band structure calculations and symmetry arguments, we identified bulk and surface states, latter of which exhibits a 6-fold symmetry. We give clear evidence for a helical spin-polarized additional surface Dirac cone below the Fermi level caused by band inversion as in topological insulators for the first time in $NiTe_2$. We observed and mentioned for the first time a "hidden" spin polarization of the bulk Dirac cone and bulk states, which is not allowed for non-magnetic materials with space-inversion symmetry. The observed P_y spin texture is anti-symmetric with respect to the $k_x = 0$ axis, consistent with the three-fold symmetry of the crystal structure.

5 Type-II Weyl semimetal $MoTe_2$

5.1 Sample preparation

High-quality single crystals of $MoTe_2$ were synthesized by Prof. Keiji Ueno's group as described in Ref. [182] for our collaboration. The crystal was mounted on the sample holder [Fig. 5.1(a)] and was cleaved *in situ* at room temperature using a carbon

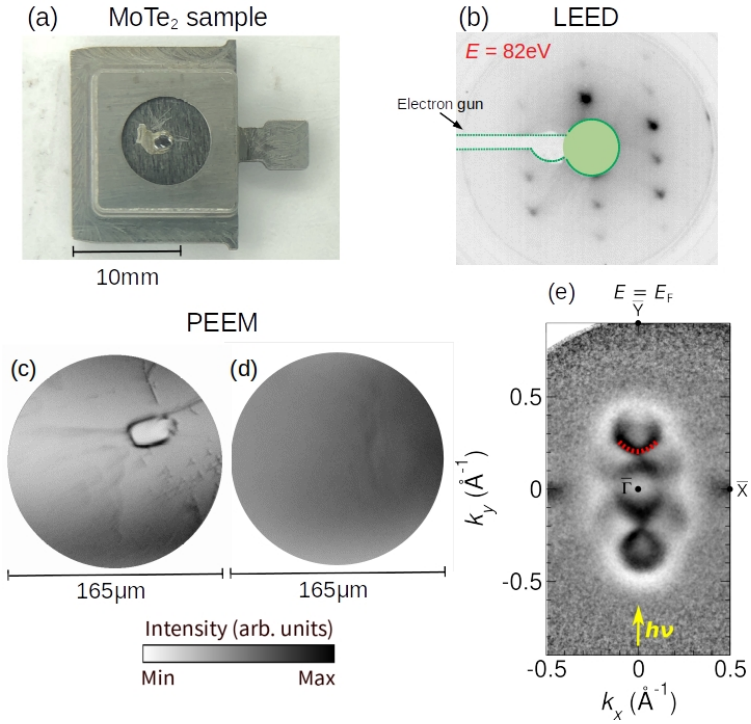

Figure 5.1: (a) $MoTe_2$ sample on the sample holder. (b) Low energy electron diffraction (LEED) pattern measured with an electron beam energy of 82 eV showing sharp spots. (c, d) PEEM images illuminated with a mercury lamp including a defect (c) and on the flat region (d). (e) Measured Fermi-surface contour using p-polarized light at a photon energy of $h\nu = 52$ eV. A red dotted line indicates the Fermi arc as a guide to the eye.

tape as in $NiTe_2$. As shown in Fig. 5.1(c), we succeeded in obtaining a low energy electron diffraction (LEED) pattern after cleavage, suggesting a clean sample surface. The experimental conditions are the same as measurements of $NiTe_2$ as described in Sec. 4.1. By measuring real space PEEM images [Figs. 5.1(c, d)], we explored the best sample region in the same way as Sec. 3.2.1. Figure 5.1(c) includes a defect and Figure 5.1(d) indicates the flat region. The synchrotron beam is illuminated on the image center in Fig. 5.1(d) as in measurements of $NiTe_2$ (see Fig. 3.5(c)), where we recorded the band dispersions.

Figure 5.1(e) shows the measured Fermi-surface contour using p-polarized light at a photon energy of $h\nu = 52\,\mathrm{eV}$. One can clearly see the hole-pocket centered at the BZ center and two electron pockets centered at the positive and negative $k_y = \pm 0.3\,\mathrm{Å}^{-1}$ and $k_x = 0$. These electron- and hole-pockets form the tilted Dirac cones in the upper and lower half of the $MoTe_2$ Fermi-surface contour. The measured Fermi-surface section here corresponds to the planar cut displayed in Fig. 2.9(a), such that the Dirac cone states appear with a linear crossing in the constant energy photoelectron momentum map. One can also observe the Fermi arc being located outside of the electron pocket towards the touching points between the electron- and hole-pockets, indicated in Fig. 5.1(e) by a red dotted line as a guide to the eye. This result is in good agreement with previous observations for this material [87, 92].

Figures 5.2 and 5.3 show the sum of photoemission intensities obtained with left and right circularly polarized light. According to the energy development of momentum maps in Fig. 5.2, the circular-like hole pocket centered at the BZ center becomes

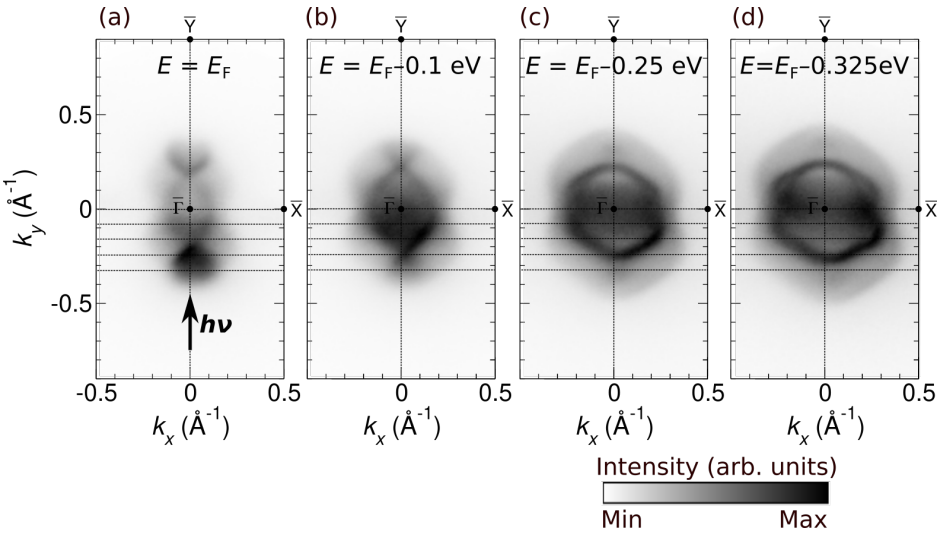

Figure 5.2: Momentum distribution of the sum of the photoemission intensities obtained with left and right circularly polarized light. (a-d) Constant-energy maps at $E = E_F$ (a), $E_F - 0.1\,\mathrm{eV}$ (b), $E_F - 0.25\,\mathrm{eV}$ (c), $E_F - 0.325\,\mathrm{eV}$ (d).

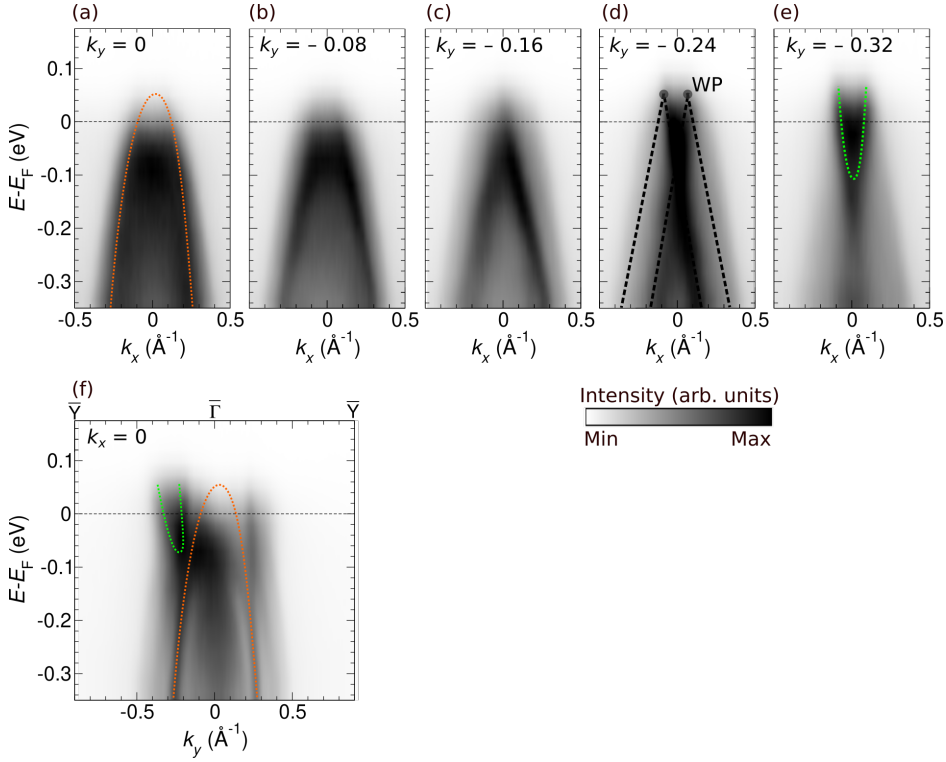

Figure 5.3: Band-dispersion maps of the sum of the photoemission intensities obtained with left and right circularly polarized light at $k_y = 0\,\text{Å}^{-1}$ (a), $-0.08\,\text{Å}^{-1}$ (b), $-0.16\,\text{Å}^{-1}$ (c), $-0.24\,\text{Å}^{-1}$ (d), $-0.32\,\text{Å}^{-1}$ (e), and $k_x = 0\,\text{Å}^{-1}$ (f). Orange and green dotted lines indicates hole and electron bands as a guide to the eye.

bigger, and the half-arc-like electron pockets become smaller and finally disappear towards deeper binding energies. Energy-momentum diagrams in Fig. 5.3 indicate sections of these hole and electron pockets. At $k_y = 0$ in Fig. 5.3(a), one can find the hole-like band with the broad band width indicated by a orange dotted line. At $k_y = -0.32\,\text{Å}^{-1}$ in Fig. 5.3(e), one can find the electron-like band centered at $k_x = 0$ indicated by a green dotted line. One can see the development of these bands. At $k_x = 0$ in Fig. 5.3(f), one can find the hole-like band centered at $k_y = 0$ and the electron-like band centered at $k_y = \pm 0.3\,\text{Å}^{-1}$. The observed band dispersions are overall consistent with previous reports [83–92].

5.2 Experimental geometry

As described in Sec. 2.4.5, the $1T'$-phased $MoTe_2$ undergoes a transition to the $1T_d$ phase by cooling down below 250 K [95]. We have performed measurements at $T \sim$ 100 K, where $MoTe_2$ crystallizes in the $1T_d$ structure and becomes a type-II Weyl

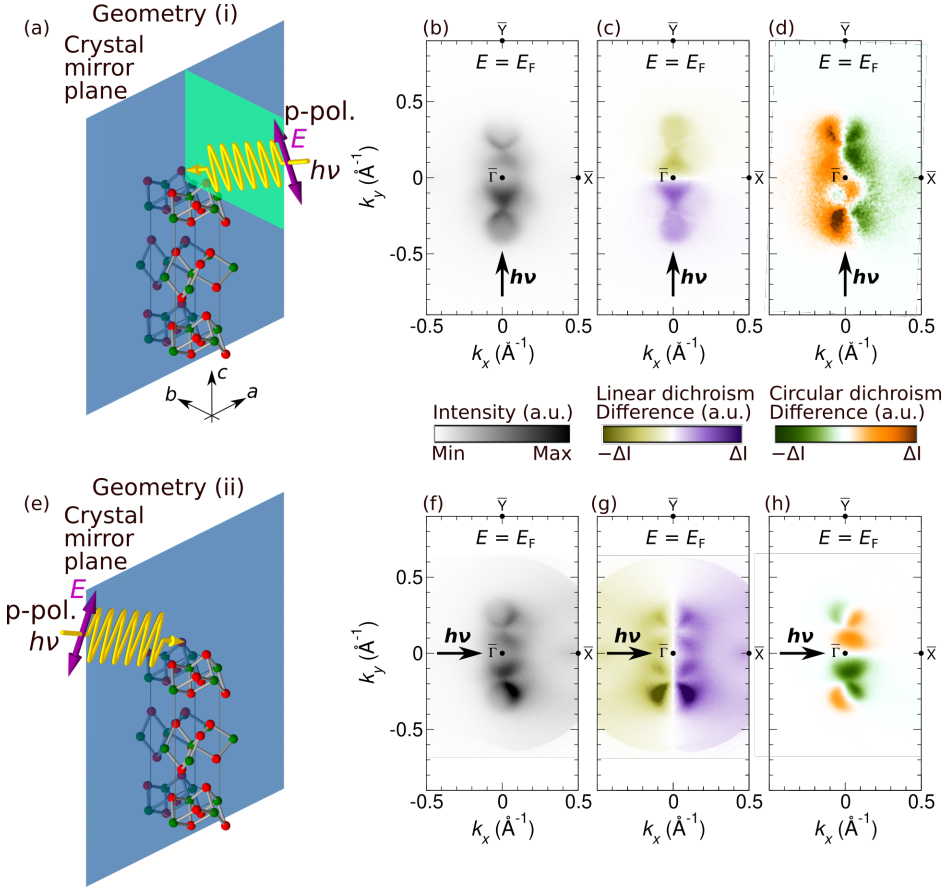

Figure 5.4: Experimental geometry. We have performed experiments with two different geometries at a photon energy of $h\nu = 52$ eV, where the optical plane is aligned perpendicular (a-d) and parallel (e-h) to the crystal mirror plane. Measured Fermi-surface contours (b, f) show top-bottom (b) and right-left (f) intensity asymmetries due to the LDAD. Corresponding maps of $I_{\mathrm{LDAD}}(k_x, k_y) = I(k_x, k_y) - I(k_x, -k_y)$ are displayed in panel (c) and $I_{\mathrm{LDAD}}(k_x, k_y) = I(k_x, k_y) - I(-k_x, k_y)$ in panel (g). The I_{CDAD} map in panel (d) shows a non-vanishing signal at the $k_x = 0$ line. The I_{CDAD} map in panel (h) shows anti-symmetry with respect to the $k_y = 0$ axis.

semimetal. $1T_d$-$MoTe_2$ possesses one mirror plane as indicated by a blue orthogonal plane in Figs. 5.4(a, e). We have performed experiments with two different geometries: (i) The optical plane is aligned perpendicular to the crystal mirror plane [Fig. 5.4(a)]. (ii) The optical plane is aligned parallel with the crystal mirror plane [Fig. 5.4(e)]. We display the corresponding results in Figs. 5.4(b-d) for geometry (i) and in Figs. 5.4(f-h) for geometry (ii). Figure 5.4 shows the measured Fermi-surface contours taken using p-polarized light (b, f), corresponding linear dichroism (c, g), and circular dichroism (d, h). For p-polarization, one can find the expected top-bottom asymmetry of the intensity with respect to the $k_y = 0$ axis in Fig. 5.4(b) for geometry (i) and right-left asymmetry with respect to the $k_x = 0$ axis in Fig. 5.4(f) for the geometry (ii). The observed intensity asymmetries reflect the linear dichroism in the angular distribution (LDAD) as described in Sec. 3.4.3. The corresponding I_{LDAD} maps defined as $I_{\mathrm{LDAD}}(k_x, k_y) = I(k_x, k_y) - I(k_x, -k_y)$ in Fig. 5.4(c) and $I_{\mathrm{LDAD}}(k_x, k_y) = I(k_x, k_y) - I(-k_x, k_y)$ in Fig. 5.4(g) visualize the LDAD effect more clearly. In geometry (i), the LDAD is caused solely by the mirror symmetry breaking due to the incident light with respect to the orthogonal plane to the incident plane. On the other hand, in geometry (ii), the LDAD is caused by a mixture of the broken mirror symmetry due to the incident light and the crystal structure. The LDAD asymmetries A_{LDAD} yield ~ 30% for both experimental geometries, and therefore we conclude that the contribution by the broken crystal symmetry is small.

Figures 5.4(d, h) show the circular dichroism. The CDAD signal I_{CDAD} is obtained from the difference in photoemission intensities for right- and left-circularly polarized light according to eq. 3.27. When the incoming light vector $\boldsymbol{q}$, the outgoing photoelectron momentum $\boldsymbol{k}$, and the surface normal $\hat{\boldsymbol{n}}$ lie in the same plane, handedness can not be defined and contribution of the asymmetric photoemission geometry to the CDAD should vanish. In geometry (i), contribution of the asymmetric photoemission geometry to the CDAD should vanish at the $k_x = 0$ line, while in geometry (ii), it should vanish at the $k_y = 0$ line. Nevertheless, we observed a non-vanishing CDAD at the $k_x = 0$ line in geometry (i), indicating an intrinsic chirality of the wave functions as described in detail in the next section. In geometry (ii), where the incident plane coincides with a crystal mirror plane, the observed CDAD map fulfills anti-symmetry with respect to the incident plane, i.e., the $k_y = 0$ axis based on eq. 3.29. The overall CDAD vanishes at the $k_y = 0$ line, since eq. 3.29 requires $I_{\mathrm{CDAD}}(k_x, k_y = 0) = I_{\mathrm{R}}(k_x, k_y = 0) - I_{\mathrm{L}}(k_x, k_y = 0) = 0$. The I_{CDAD} maps also contain a contribution of the LDAD, in addition. In particular, Figure 5.4(h) shows a clear left-right asymmetry. Later in this chapter, we focus on experiments with geometry (i).

5.3 Circular dichroism of the Weyl states

Figure 5.5 shows the energy development of momentum distribution of the CDAD measured at a photon energy of $h\nu = 60$ eV. In the Fermi-surface contour in Fig. 5.5(a), one can clearly see the CDAD texture of "X"-shaped crossings originating from the

boundary between the electron and hole pockets, which is summarized in Fig. 5.5(e). Interestingly, the relative positions of the orange and green hole bands are changed at an energy of $E \sim E_F - 0.27$ eV as recognized in the vicinity of the $k_x = 0$ line. For example, in the positive k_y region in Fig. 5.5(c), the green band on the negative k_x side has a larger k_y distance from the BZ center at $k_x = 0$ than the orange one on the positive k_x side. In the case $E < E_F - 0.27$ eV as shown in Fig. 5.5(d), the orange one on the positive k_x side has a larger k_y distance than the green one on the negative k_x side.

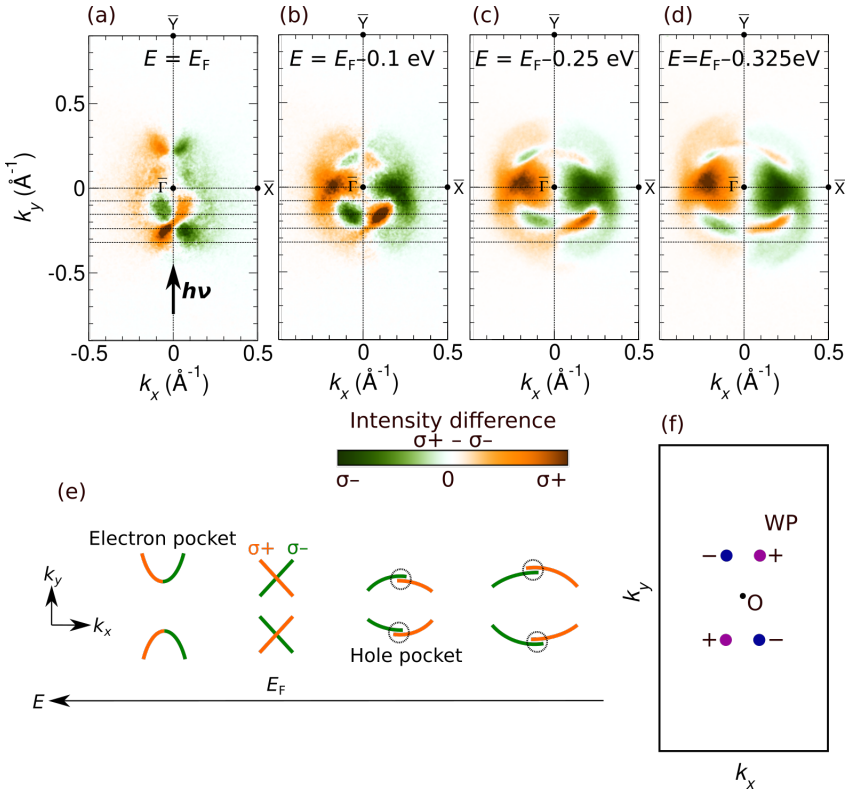

Figure 5.5: Momentum distribution of the circular dichroism measured at a photon energy of $h\nu = 60$ eV. (a-d) Constant-energy maps at $E = E_F$ (a), $E_F - 0.1$ eV (b), $E_F - 0.25$ eV (c), $E_F - 0.325$ eV (d). Plotted intensities indicate the difference of photoemission intensities for right- ($\sigma+$) and left- ($\sigma-$) circularly polarized light according to the color code. (e) Schematic band-structure development as a function of binding energy. (f) Configuration of the Weyl points in momentum space. In $1T_d$-$MoTe_2$, the Weyl points are located at $k_z = 0$. Purple and dark blue colors indicate the opposite chirality of the Weyl points.

A schematic evolution of the corresponding band features as a function of the binding energy is summarized in Fig. 5.5(e). Electron pockets are located above E_F (left). Moving down in energy towards E_F, electron and hole pockets touch each other, corresponding to the crossings (second schematic from left) that we observed in Fig. 5.5(a). At deeper binding energies the crossing point again opens and the constant energy contour shows the hole pockets. The relative position of the green and orange hole bands are changed, as indicated by black dotted circles.

Figures 5.6(a-e) show the band-dispersion maps plotted along cuts parallel to the $\overline{X} - \overline{\Gamma} - \overline{X}$ direction (see horizontal dotted lines in Figs. 5.5(a-d).) The CDAD here reveals more details of the development of the Weyl cones, indicated by black dotted lines as a guide to the eye in Fig. 5.6(d), as compared to the sum of the photoemisson intensities in Fig. 5.3. In particular we observe that the pair of Weyl cones exhibits a strong CDAD signal, whereas the sign is reversed between the two cones. As described in Sec. 3.4.2, the CDAD couples to chiral systems and probes the orbital part of the

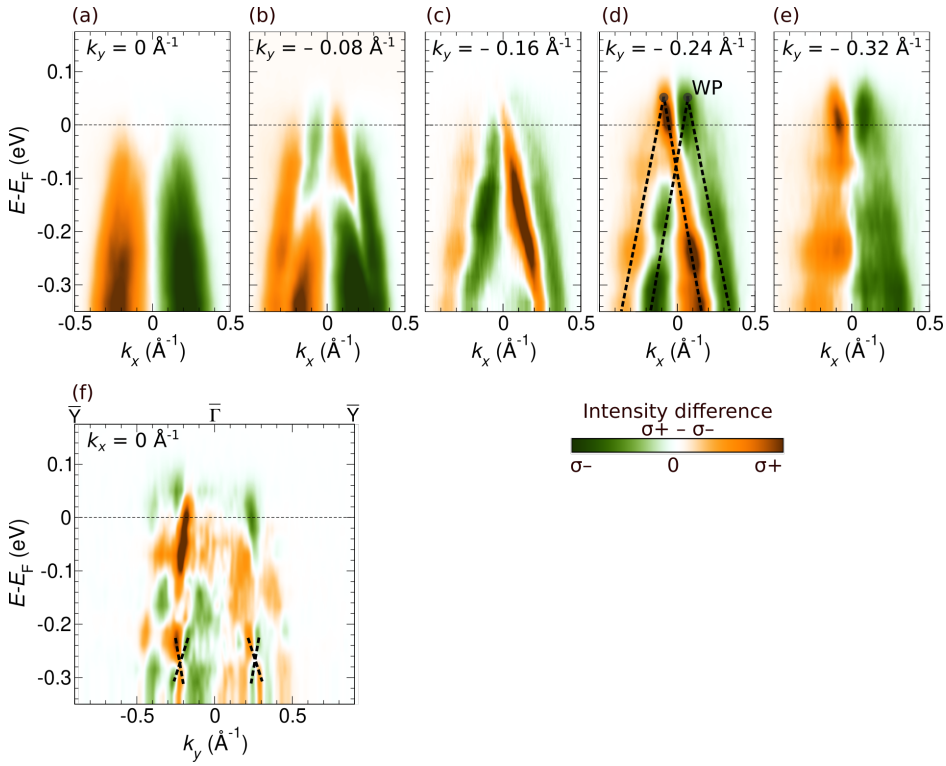

Figure 5.6: Band-dispersion maps of the circular dichroism measured at a photon energy of $h\nu = 60$ eV at $k_y = 0\,\text{Å}^{-1}$ (a), $-0.08\,\text{Å}^{-1}$ (b), $-0.16\,\text{Å}^{-1}$ (c), $-0.24\,\text{Å}^{-1}$ (d), $-0.32\,\text{Å}^{-1}$ (e), and $k_x = 0\,\text{Å}^{-1}$ (f)

wave function. The CADA is also related to the orbital angular momentum. As demonstrated in the type-I Weyl semimetal TaAs in Fig. 3.15, the orbital angular momentum is correlated with the Berry curvature field describing the Weyl points. The Weyl points of $1T_d$-$MoTe_2$ are located close to the $k_x = 0$ line where geometry contributions to the CDAD minimize. The CDAD signal here strongly reflects the chirality of the electronic structure, in particular, the chiral charge of the respective Weyl points, which is connected with the Berry curvature. Therefore, the pair of Weyl cones exhibiting a strong CDAD with reversed sign indicates the opposite chirality of the respective Weyl points. This experimental geometry is best suited to get access to the chiral charge of the Weyl points.

For reference, the configuration of the Weyl points in momentum space and their chirality are indicated in Fig. 5.5(f) (For details of the Weyl-point location and chiraliy in general see Fig. 2.6 and Sec. 2.4.1). The CDAD fingerprint allows to determine the Weyl-point energy to be located +50 meV above E_F. The Weyl-point location in energy is in good agreement with a previous report [84, 91]. From our experimental results we could identify a certain scenario with a total of 4 Weyl points [84, 91]. Note that the CDAD of the Weyl point on the other k_y side, i.e., Weyl points at $(k_x, k_y) = (+,+)$ and $(+,-)$ exhibits the same sign, but the chirality should be reversed as indicated in Fig. 5.5(f). This is because the CDAD is constrained by the experimental geometry. A more detailed discussion in comparison with calculation will follow in Sec. 7.4.

The features related to the Weyl cone depend on the photon energy, which is evident for the bulk Weyl cone. In particular, the spectral weight of surface states could be enhanced using UV light as in Sr_2RuO_4 [183] and Bi_2Se_3 [158]. Here, we chose the photon energy such that the section probed by the photon energy through the bulk BZ corresponds to the high-symmetry point $k_z = 0$ and coincides with the bulk Weyl point.

At $k_x = 0$ in Fig. 5.6(f), we observe cone-like bands with crossing points at $E \sim E_F - 0.27$ eV indicated by black dotted lines. The behavior of this band corresponds to a change of the relative positions of the green and orange colored hole bands in the vicinity of the $k_x = 0$ line. As mentioned before, a CDAD that would arise from a broken mirror symmetry in the photoemission geometry vanishes at the $k_x = 0$ line. Therefore, the observed CDAD at $k_x = 0$ probes an intrinsic chirality of the wave functions. The observed cone-like band might therefore be a signature of chiral cones. The cone can not be observed by the sum of the photoemision intensity in Fig. 5.3(f), but only observed by the CDAD. Correspondingly, the splitting of the hole pockets at $k_x = 0$ in the momentum section can not be observed by the sum of the photoemision intensity in Figs. 5.2(c, d). In contrast, we observed the splitting as a change of the relative positions of the green and orange colored hole bands in Figs. 5.5(c, d). The CDAD provides more information and can only visualize these states at $k_x = 0$. The presence of the possible chiral cones here has not been reported, and so far not predicted and discussed in theory. The relationship between these states and the Weyl physics are interesting and can be an open question.

5.4 Spin texture

Some first-principles-calculation and spin-resolved photoemission studies suggest that Fermi arcs exhibit spin-momentum-locked spin textures on the type-I Weyl semimetals (Ta, Nb)(As, P) [184–186] and the type-II Weyl semimetal WTe_2 [187], similar to the chiral edges states of topological insulators (see Secs. 2.2.3 and 2.3.2). Other studies on the type-II Weyl semimetal $MoTe_2$ have indeed reported the existence of spin-polarized bulk and trivial surface states [89, 90, 92], but not yet resolved the spin texture of the Weyl cones and the Fermi arc.

Figure 5.7 shows the spin-resolved Fermi-surface contour measured at a photon energy of $h\nu$ = 52 eV. Using s-polarized light, shown in Fig. 5.7(a), the observed spin texture shows a single crossing of spin-up (red) and spin-down (blue) states. The measured spin polarization is always given with respect to the positive k_y axis. This spin texture corresponds well to the observed CDAD texture from Fig. 5.5(a), which is here also displayed on the right hand side of Fig. 5.7(a) as a reference. For p-polarized light, shown in Fig. 5.7(b), the observed spin texture shows additional details. In particular, the "X"-shaped contours of the Weyl cone states appear as double lines, where a spin-down (blue) state is located slightly left of a spin-up (red) state. The sketch on the right hand side of Fig. 5.7(b) summarizes the observed Fermi-surface contour in the $k_y > 0$ region as a guide to the eye. The $k_{\parallel}$ separation of the spin-split states that we observe here is too small to be resolved in a spin-integrated measurement, e.g., in Fig. 5.1(e).

The spin splitting of the Weyl cone states is caused by a combination of SOC and the broken inversion symmetry describe in Sec. 2.3.1. As explained in Secs. 2.2.1 and 2.4.3, if the Dirac semimetals break space-inversion symmetry, a spin degenerate Dirac cone splits into a pair of spin-split Weyl cones with the opposite chiral charge. Thus, spin texture of the Weyl cones can be related to the chiral charge of the Weyl points. Therefore, we conclude that the observed reversed spin polarization to the two cones in the half BZ can be explained by the opposite topological chiral charge of a pair of the Weyl points.

Our observation of different spin textures for measurements taken with p-polarized light versus s-polarized light, where no spin-splitting of the "X"-shaped contour is observed, can be explained by optical selection rules. As described in Sec. 3.4.1, p- and s- polarized light selectively probe contributions to the Weyl cone states of even and odd orbitals, respectively. As shown in Figs. 3.11(b, c) photoemission distribution in the type-I Weyl semimetal TaP exhibits rich intensity variations between p- and s-polarization [154]. In contrast, we can not see a significant difference of spin-integrated photoemission intensities between p- and s-polarization in $1T_d$-$MoTe_2$. However, we observed different spin textures between p- and s-polarization. This is the similar case in topological surface states of Bi_2Se_3 [156, 157, 160], i.e, there is not a significant difference of spin-integrated photoemission intensities except for asymmetry of intensities due to the LDAD, but the different spin textures excited by p- and s-polarization. Therefore, we conclude that even and odd orbitals of the Weyl cones probed by p- and s-polarized light, respectively, possess the different spin texture.

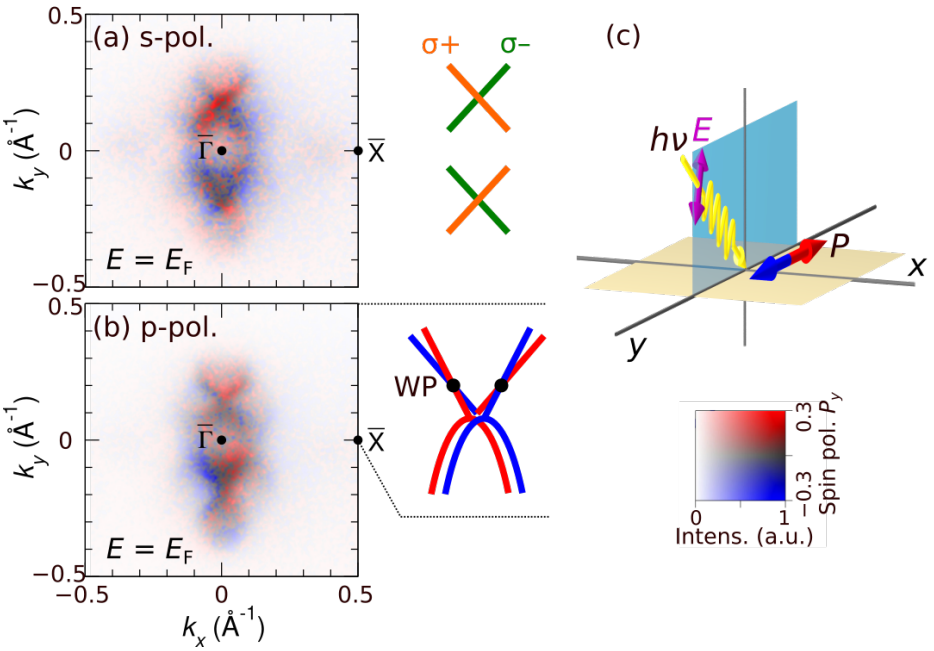

Figure 5.7: Spin texture of the Weyl cones. Spin-resolved Fermi-surface contour measured using s-(a) and p-(b) polarized light at a photon energy of $h\nu = 52$ eV. Sketches on the right hand side summarize the observed Fermi surface features in (k_x, k_y) as a guide to the eye. A sketch in panel (a) shows the observed CDAD texture from Fig. 5.5(a) by using the same green and orange color code as in Fig. 5.5. In panel (b), a sketch is shown in the $k_y > 0$ upper half region. (c) Photoemission experimental geometry. A purple arrow indicates the electric field vector ($\boldsymbol{E}$) for p-polarized light. Spin-resolved intensities are encoded using the 2D colour code: red and blue intensities indicate spin-up and spin-down photoelectrons with a spin quantization axis along the k_y direction.

For p-polarization, we observed the chiraliy-reflecting spin texture of the Weyl cones.

Here, we discuss the relationship between spin texture and the CDAD. In the case of the type-I Weyl semimetal TaAs, the spin-split states carry parallel orbital angular momentum, while antiparallel spin angular momentum as shown in Figs. 3.15(a, b) [173]. Comparison between results of the CDAD and spin texture excited by p-polarization suggests the different texture of the P_y spin angular momentum and the orbital angular momentum probed by the CDAD on the spin-spilt adjacent states of the Weyl cones. The P_y spin texture related to odd orbitals probed by s-polarization seems to show a coincidence of the orbital angular momentum proved by the CDAD.

There is an additional asymmetry of photoemission intensities and spin polarization between the top and bottom half of the Fermi-surface image, observed for p-polarized

light due to the LDAD. We have already seen the LDAD effect for spin-integrated results in Sec. 5.2. Similar to the topological surface states in Bi_2Se_3 as shown in Fig. 3.12 [158], we observe here the LDAD effect for the spin polarized states.

5.5 Summary

Taking into account crystal and experimental symmetries, we discussed symmetry of the observed band structures for two different experimental geometries. We experimentally clarified circular dichroism and spin texture of the Weyl cones for the first time in type-II Weyl semimetals. We captured a pair of chiral Weyl cones in energy and momentum space exhibiting a strong circular dichroism with reversed sign, giving evidence for a opposite chiral charge of the respective Weyl points. We observed a signature of chiral cones below the Fermi level with the intrinsic chirality of the wave functions probed by the circular dichroism, which has not been reported so far. A pair of spin-split Weyl cones, caused by spin-orbit coupling and broken inversion symmetry of the $1T_d$ crystal structure, was found to exhibit a reversed spin texture when probed by p-polarized light. The spin texture can be explained by the opposite topological charge. The observed spin texture of the Weyl cones excited with s-polarized light corresponds well to its circular-dichroism texture.

6 Chiral topological semimetal CoSi

6.1 Sample preparation

High-quality single crystals were grown by the modified Bridgman method with the help of an optical floating-zone furnace as described in Ref. [188, 189] and polished on the (100) surface as shown in Fig. 6.1(a). The size of the crystal is 8mm × 8mm × 8mm and the size of the polished surface is 4mm. On the basis of collaboration with National Taiwan University, Dr. Yu-Hsun Chu and Dr. Guo-Jiun Shu at Prof. Fang-Cheng Chou's group synthesized the crystals and the surface preparation was performed together with Mr. Kui-Hon Ou Yang, Ms. Yi-Hsin Shen, Mr. Chien Jing, and Dr. Yu-Hsu Chu at NanoMagnetism laboratory (Prof. Minn-Tsong Lin's group). Since the Co and Si atoms are strongly bonded by multiple covalent bonds in three dimensions and the high symmetry surfaces are not cleavage planes, we performed Ar^+ sputtering and annealing in the preparation chamber of the NanoESCA beamline in order to get a clean sample surface instated of cleaving the sample. Although the sputter process usually leads to clean surfaces, the quality of as-sputtered surfaces is disordered and far from being single crystalline. Nevertheless, single crystallinity can be restored by annealing the surface after sputtering. Klein et al. compared FeSi(100) surfaces prepared by cleaving, and sputtering and annealing, reporting that the cleaved surface contained a mixture of various crystalline directions, which might not be a good surface for photoemission studies [190]. Takane et al. cleaved CoSi crystals more than 50 times, and in a very few cases they succeeded in cleaving them and in observing the band dispersion [116]. The advantage of preparation by sputtering and annealing is to easily reproduce a clean surface every time. To evaluate the quality of the sample surface and to confirm the crystal orientation, we measured low energy electron diffraction (LEED). Based on LEED patterns, we rotated the sample on the sample holder to align the sample with respect to the microscope coordinate. Referring to the cleaning procedure of the transition-metal monosilicides FeSi [190, 191] and MnSi [192], we explored the best condition for the *in situ* surface preparation of CoSi. Here, we have obtained the best results as follows:

- Ar^+ sputtering with an energy of 2 keV
- Annealing at $T \sim 680°C$ for 40 min

After more than ten cleaning cycles, we observed sharp LEED spots and clear band dispersions (see Fig. 6.2). The observed LEED spots are arranged in a square-like (1 × 1) pattern consistent with the symmetries expected for the (100) surface termination of CoSi.

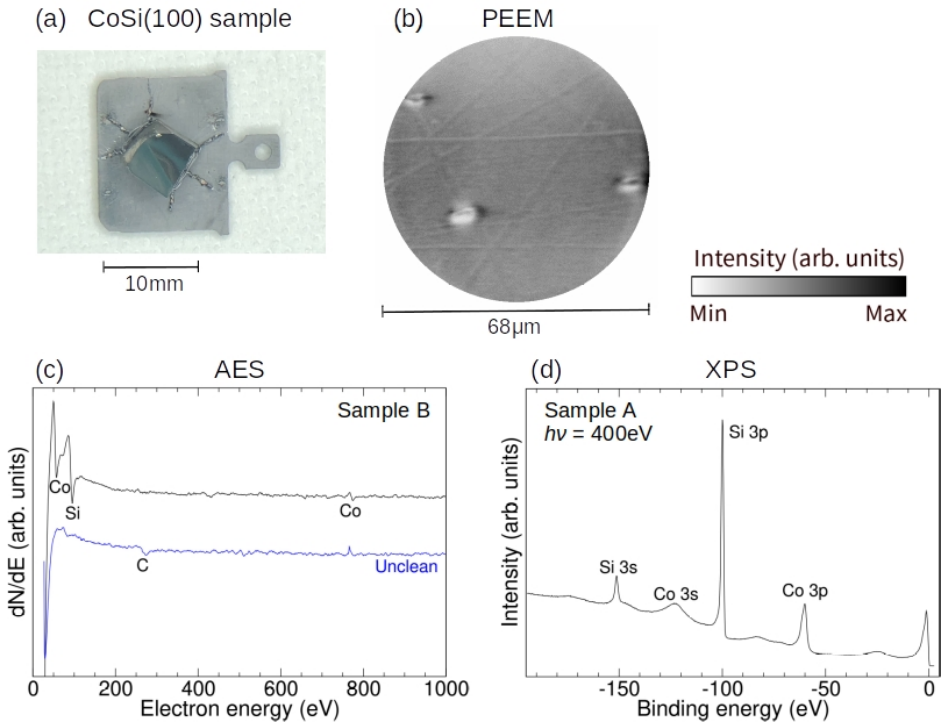

Figure 6.1: Characterization of the sample surface on CoSi(100). (a) Polished CoSi(100) crystal on the sample plate. (b) PEEM image illuminated with a mercury lamp showing defects and polishing scratches. (c) Auger electron spectroscopy (AES). An unclean sample without degas, sputtering, and annealing indicated by a blue line shows a clear C auger peak. A sample after a few cycles of the cleaning procedure indicated by a black line shows clear Co and Si peaks. (d) X-ray photoemission spectra (XPS) after the cleaning procedure obtained with a photon energy of $h\nu = 400$ eV.

As shown in Fig. 6.1(c), Auger electron spectroscopy (AES) before degas after introducing a sample into a vacuum in the preparation chamber of the NanoESCA beamline from the air, denoted by an "unclean" sample (blue line), detects a C auger peak as a major contamination. After a few cycles of the cleaning procedure, AES (black line) shows clear Co and Si peaks, revealing a clean surface. These results are similar to the AES of FeSi [193]. X-ray photoemission spectra (XPS) also shows clear core level peaks of Co and Si. A PEEM image [Fig. 6.1(b)] shows defects and polishing scratches. Before the momentum microscope measurements, the best sample region was selected by using PEEM.

We measured two different samples as shown in Fig. 6.2. LEED patterns show

sharper spots on sample B [Fig. 6.2(b)] than sample A [Fig. 6.2(a)]. Reflecting the sharpness of the LEED spots, measured Fermi surfaces show sharper bands of sample B [Fig. 6.2(d)] than A [Fig. 6.2(c)]. Interestingly, we found that the propagation

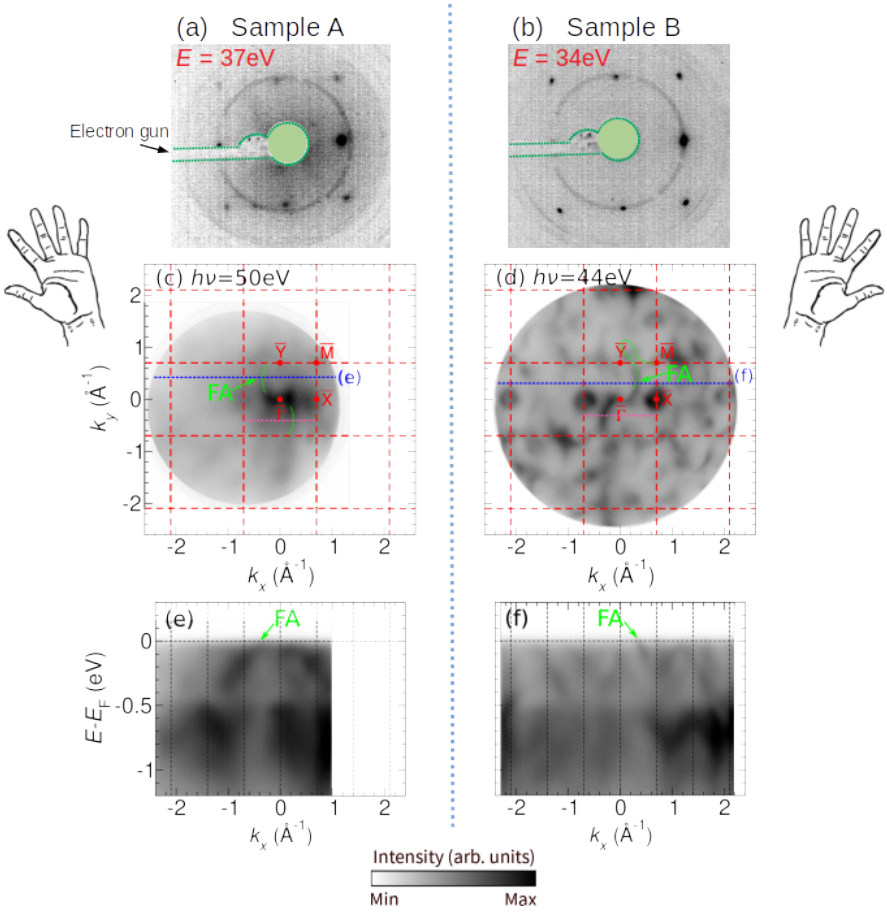

Figure 6.2: Measurement of two different samples with opposite structural chirality. (a, b) LEED patterns measured with an electron beam energy of 37 eV (sample A), 34 eV (sample B) show sharper spots on sample B than sample A. (c, d) Measured Fermi surfaces at a photon energy of $h\nu = 50$ eV (sample A), 44 eV (sample B) using p-polarized light show sharper bands of sample B than A. We apply the Chern-number analysis to blue and pink dotted lines. (e, f) Energy-momentum diagrams along cuts indicated by blue dotted lines in panels (c, d) show the dispersion of the Fermi arc (FA) indicated by green arrows. A reversal of the Fermi-arc velocities between both samples implies a different handedness of the chiral crystals.

direction of the Fermi arcs (FA) is reversed. For sample A, the FA extends from the $(k_x, k_y) = (-1, 1)$ direction to the BZ center on the top half of the BZ, while from the $(k_x, k_y) = (1, 1)$ direction to the BZ center for sample B. To analyze the topological nature of the surface states, we applied the criteria described in Sec. 2.2.3. We now count chiral edge modes passing through E_F along cuts indicated by blue dotted lines in Figs. 6.2(c, d). For sample A, one right-moving chiral edge is found within the 1st BZ indicated by a green arrow, implying Chern number $C = +1$ for the 2D subsystem. While for sample B, one left-moving Fermi arc implies $C = -1$. In the same way, we can obtain $C = -1(+1)$ for the 2D subsystem at the negative k_y as indicated by pink dotted lines for sample A (B). Therefore, when the 2D slice is swept from negative k_y to positive k_y, the Chern number should changes by $+2(-2)$ for sample A (B), corresponding to presence of topological chiral charge $C = +2(-2)$ at the BZ center for sample A (B). Based on the discussion described in Sec. 2.5.3, a reversal of the Fermi-arc velocities and the corresponding opposite sign of Chern numbers between sample A and B suggests the different handedness of chiral crystals. Unlike the results of PdGa shown in Fig. 2.13 [120], the handedness of the crystal structure can not be distinguished by LEED here for CoSi. The LEED pattern of sample A indeed shows multiple domains confirmed by changing the beam position, while that of sample B shows a single domain in a large region. Considering the lower quality of the LEED spots and the observed bands, and appearance of multiple domains on sample A, one of the enantiomers with one handedness might be unstable and not be able to be synthesized with as high quality as sample B. A recent study reported band dispersions of two enantiomers with opposite handedness for CoSi, though the quality of dispersions with both enantiomers is slightly different [194]. For the high-resolution momentum microscope experiment, we measured sample B.

6.2 Photon-energy dependence

To identify bulk and surface states, we performed photon-energy-dependent measurements. Figure 6.3 shows measured Fermi-surface cuts at the photo energies $h\nu =$ 36 eV, 44 eV, 56 eV with p-polarized light. One can clearly observe the Fermi arc extending from the BZ corner to the BZ center for all photon energies. One can also see a circular electron pocket centered at the $\overline{\mathrm{X}}$ point for all photon energies. These photon-energy-independent features belong to surface states. Thus, we name the electron pocket the surface electron (SE) pocket. One can find that photoemission intensity increases around the BZ center with increasing photon energy. As described in Fig. 2.11(e) and in Sec. 2.5.3, a star-shaped hole pocket develops in the 3D BZ and exists around the Γ point. We then conclude that intensity around the BZ center reflects the hole pocket. A section at $h\nu = 36$ eV cuts through the X points, suggesting almost no intensity. A section at $h\nu = 44$ eV partially cuts through the hole pocket between the X and Γ points. A section at $h\nu = 56$ eV cuts through the center of the hole pocket at the Γ point. Since the star-shaped hole pocket corresponds to a flat band composing the unconventional fermion, as seen in the next section, we name it

bulk flat (BF) band.

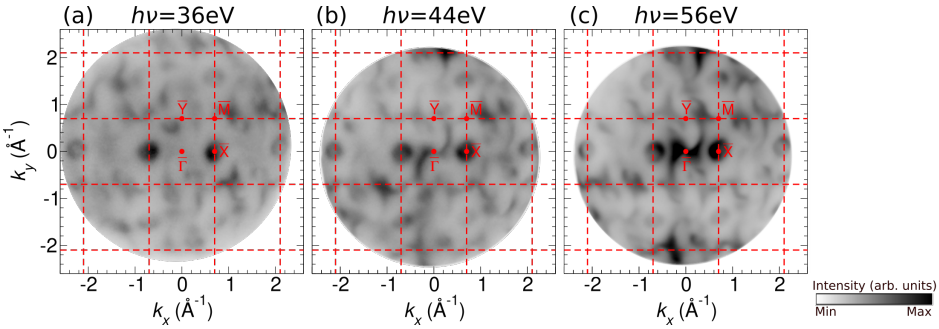

Figure 6.3: Fermi-surface cuts measured at the photon energies $h\nu$ = 36 eV (a), 44 eV (b), 56 eV (c) with p-polarized light.

6.3 Dichroism and orbital contribution in the band structure

We focus on the band structure at the high-symmetry Γ point, where the unconventional fermion is predicted, and uncover a polarization-dependent band structure for the first time. Figures 6.4 and 6.5 show energy development of momentum maps excited with p- and s-polarized light at a photon energy of $h\nu$ = 56 eV, respectively. At $E = E_F$ the BF band is pronounced with p-polarization indicated by an orange arrow, while being less pronounced with s-polarization. At $E = E_F - 0.05$ eV, some parts of the BF band is found to be suppressed with p-polarization indicated by a transparent orange arrow with BD but enhanced with s-polarization. The elliptic contour of the BD band centered at the $\overline{\Gamma}$ point becomes bigger towards deeper biding energies. Different parts of the elliptic contour are pronounced with different polarizations clearly seen at $E = E_F - 0.3$ eV. Considering that different light polarization probes different orbital symmetries descried in Sec. 3.4.1, this suggests the orbital symmetry of the BF and BD band abruptly changes even within the same state.

Our observation clearly shows the band structure of the FA indicated by green dotted lines in Fig. 6.4 as a guide to the eye. The top right FA extending from the BZ center rotates clockwise with increasing binding energy as indicated by a blue arrow in Fig. 6.8(a), providing evidence for the helicoid arc. This helicoid arc realizes van Hove singularity (VHS), namely the singularity in the electronic structure as recently predicted and experimentally observed in Ref. [125]. As summarized in Figs. 6.8(a-d), different parts of the helicoid arc rotating clockwise (blue arrow) and counterclockwise (red arrow) approach each other and touch at a generic momentum at $E = E_{VHS} = E_F - 0.05$ eV, and then are separated into two parts. Overall shape of the FA is consistent rather with the calculation in Ref. [125] than Fig. 2.12. Conditions

of surface calculations in CoSi strongly affect the shape of the FA and whether the SE band appears [109, 111, 112, 114, 117, 125]. Further precise surface calculation is needed to clarify the FA and surface states.

Figures 6.6 and 6.7 show photoemission intensities obtained with $I_R + I_L$ and $I_R - I_L$ (circular dichroism (CDAD)) at a photon energy of $h\nu = 56$ eV, respectively. The BF band exhibits a strong CDAD, which visualizes the shape of the star hole pocket clearly. The top left star is enhanced with right circularly polarized light (orange color code), whereas the bottom right star with left circularly polarized light (green color code). Careful inspection of the CDAD reveals that the BF band and the BD band indeed merge near E_F. For instance, the orange top left star extends from the positive k_x with a smaller radius (right part) via the positive k_y to the negative k_x with a larger radius (main part, i.e, the BF band), i.e., forms a half-arc-like feature around the upper side of the BZ center. The green bottom right star forms a half-arc-like feature

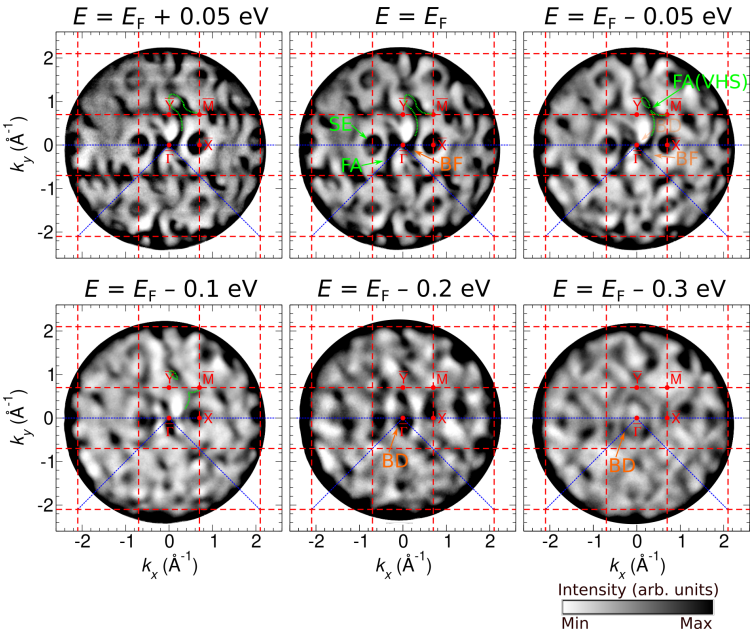

Figure 6.4: Energy development of momentum distribution of photoemission intensity measured at a photo energy of $h\nu = 56$ eV (Γ point) with p-polarized light. High symmetry points of the surface Brillouin zone are indicated by the corresponding red labels. Blue dotted line indicate sections for energy-momentum diagrams displayed in Fig. 6.10. BD: Bulk Dirac band. BF: Bulk flat band (corresponding to the star-shaped hole pocket). SE: Surface electron pocket. FA: Fermi arc. FA(VHS): Position of the van Hove singularity (VHS). Green dotted lines indicate the FA as a guide to the eye. Orange and green arrows indicate bulk and surface bands, respectively.

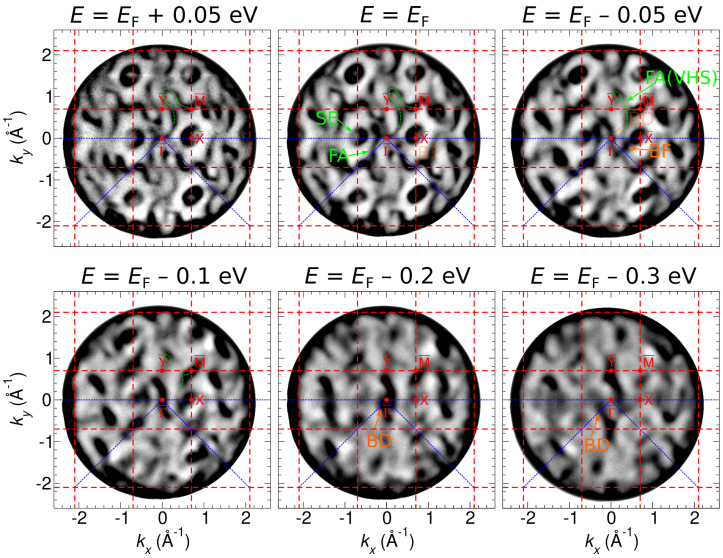

Figure 6.5: Momentum distribution of photoemission intensity obtained with s-polarized light. Symbols as in Fig. 6.4.

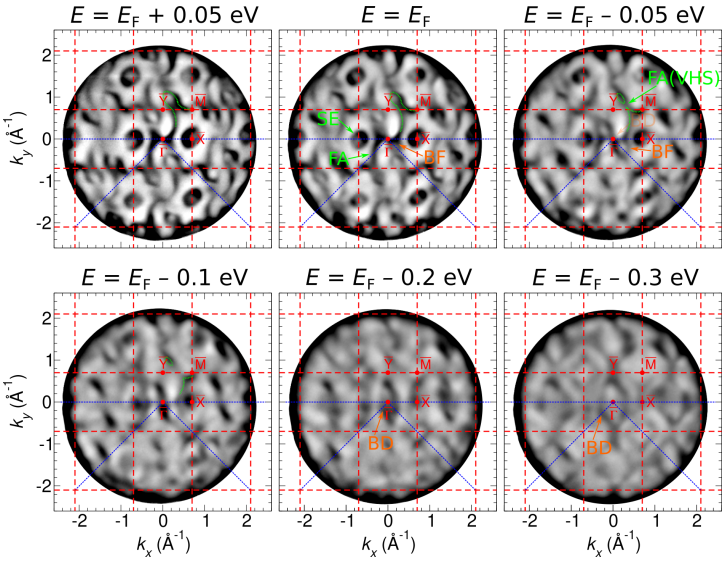

Figure 6.6: Momentum distribution of photoemission intensity $I_R + I_L$ obtained with right- and left-polarized light. Symbols as in Fig. 6.4.

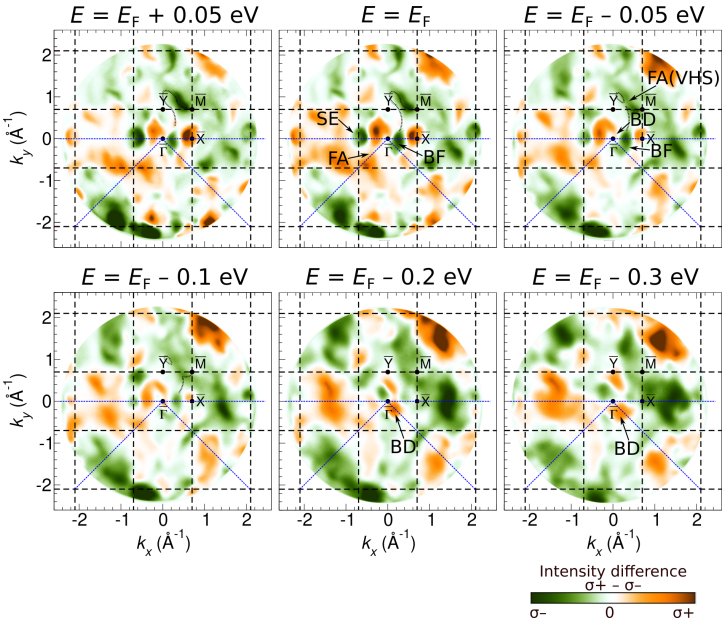

Figure 6.7: Momentum distribution of photoemission intensity $I_R - I_L$ showing circular dichroism. Symbols as in Fig. 6.4.

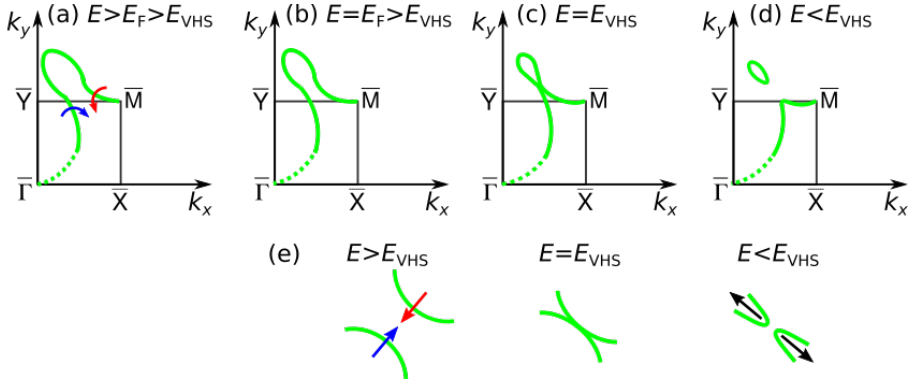

Figure 6.8: van Hove singularity of the helicoid Fermi arc in CoSi. (a-d) Energy development of the helicoid Fermi arc observed in our study. (e) Cartoon illustration of the helicoid arc. As a function of binding energy, two helicoid arc move closer together, and then touch at a singularity energy $E = E_{VHS}$, and finally move away with a different connectivity. Red, blue and black arrows indicate the moving direction of the helicoid arc.

around the lower side of the BZ center. The right part of the orange star and the left part of the green star composes a small ring centered at the $\overline{\Gamma}$ point, i.e., the BD band. The elliptic contour of the BD band seems to be separated by orange and green bands clearly seen at $E = E_F - 0.3$ eV. We have already observed the abrupt intensity change of the BD band excited with p- and s-polarized light. Here, the abrupt change of the CDAD sign again suggests that the orbital character of the BD band abruptly changes even within the same state. Nevertheless, the $I_R + I_L$ map [Fig. 6.6] exhibits almost even intensity for the state. This is because circularly polarized light can probe all orbital symmetries and the $I_R + I_L$ map compensates the asymmetry of the intensity. The FA exhibits finite intensity for p- and s-polarization, while a weak CDAD compared to the BF band. We suppose that the spin angular momentum is coupled to the orbital angular momentum here due to SOC, though we do not see the spin-split FA within our experimental resolution. As shown in Fig. 2.12(b), the spin-spilt FAs carry a mutually opposite spin. As described in Sec. 3.4.2, the CDAD can probe the orbital angular momentum. In our measurement, the FA appears to be degenerate in terms of the spin and orbital angular momentum, which may result in a weak CDAD of the FA.

In order to access a question of whether the CDAD depends on a handedness of the chiral crystals, we performed the CDAD with two samples with opposite handedness as shown in Fig. 6.9. The SE bands centered at the $\overline{X}$ point exhibit the same CDAD sign with both samples, i.e., orange signal at the positive k_x side and green signal at the negative k_x side. The SE band is a trivial surface state, and exhibits a mirror-symmetric band shape which does not reflect chirality. On the other hand, not only a bulk-derived feature around the $\overline{\Gamma}$ point is mirrored due to the opposite handedness of the chiral crystals, but also its CDAD sign is reversed between both samples. This bulk band breaks a mirror symmetry for the band shape, reflecting pronounced chirality. Even though the quality of sample A is not as good as sample B, this measurement gives possible conclusions that the CDAD sign of trivial surface states or/and not chiral-reflected bands is independent of the structural handedness,

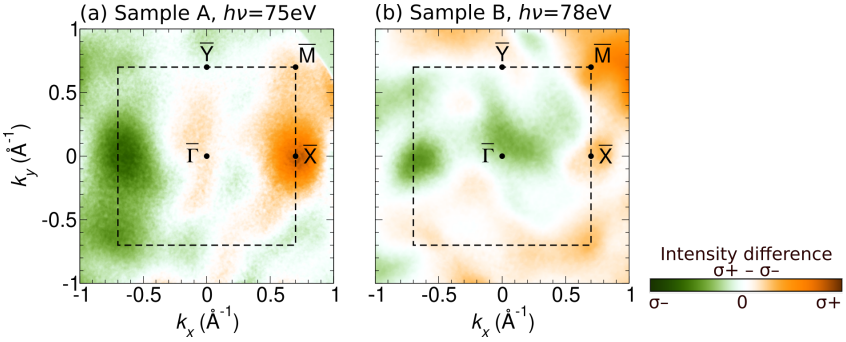

Figure 6.9: Circular dichroism of two samples with a different handedness of the chiral crystals. (a) Sample A. (b) Sample B.

while that of bulk states or/and chiral-reflected bands depends on the structural handedness.

Figure 6.10 show band-dispersion maps excited with differently polarized light, indicating photoemission intensities obtained with p-polarized light (a, e), s-polarized light (b, f), $I_R + I_L$ (c, g), $I_R - I_L$ (CDAD) (d ,h). Figures 6.10(a-d) and 6.10(e-h) indicate energy-momentum diagrams along the $\overline{X} - \overline{\Gamma} - \overline{X}$ and the $\overline{M} - \overline{\Gamma} - \overline{M}$ directions, respectively. The corresponding sections are indicated by blue dotted lines in Fig. 6.4. An excellent agreement between experiment and calculated bulk bands taken from Ref. [112] (dark blue lines) for the BD and BF bands provides evidence for the presence of the unconventional fermion, consistent with previous experimental [114, 116, 117] and theoretical [109, 111, 112] studies. We can now confirm that the star-shaped hole pocket forms the bulk flat (BF) band in the energy-momentum section. One can see that the dispersion of the SE band is centered at the $\overline{X}$ point. The BF band is sensitive to p-polarization compared to s-polarization and exhibits a strong CDAD. The BD cone and BF band are found to always exhibit the opposite CDAD signal. For instance, at the positive k_x side on the right hand side, the BD cone exhibits orange signal, while the BF band green signal. One can

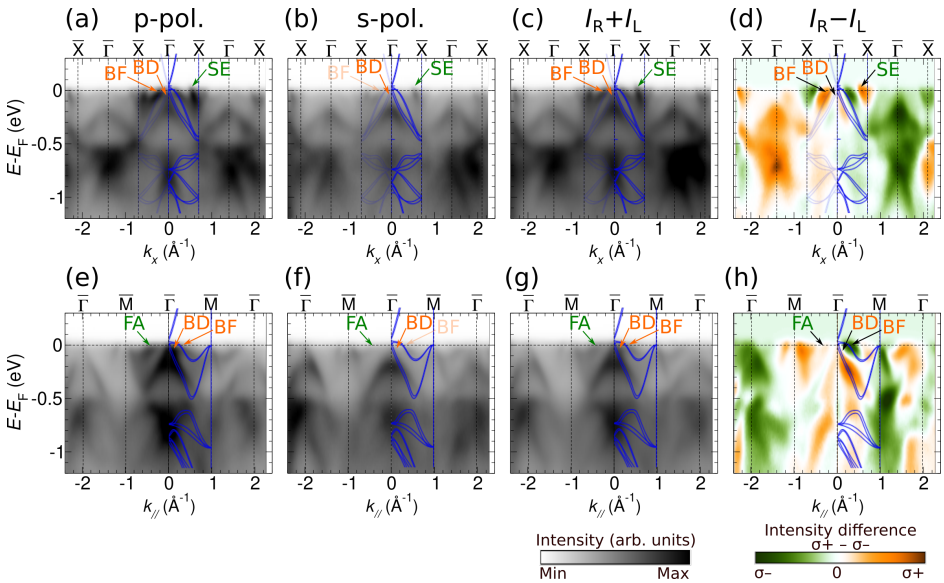

Figure 6.10: Band-dispersion maps excited with differently polarized light at a photon energy of $h\nu = 56$ eV. Photoemission intensities obtained with p-polarized light (a, e), s-polarized light (b, f), $I_R + I_L$ (c g), $I_R - I_L$ (circular dichroism) (d, h). Directions of energy-momentum diagram along $\overline{X} - \overline{\Gamma} - \overline{X}$ (a-d) and $\overline{M} - \overline{\Gamma} - \overline{M}$ (e-h) are indicated by blue dotted lines in Fig. 6.4. Dark blue lines indicate calculated bulk bands taken from Ref. [112].

also see the dispersion of the FA, exhibiting finite intensity for p- and s-polarization, while a weak CDAD, in contrast to the BF band. The behavior of these polarization-dependent bands is consistent with the observed momentum maps shown in Figs. 6.4-6.7. Based on criteria described in Sec. 3.4.1, the BF band sensitive to p-polarization mainly consists of even orbitals. We saw the previous application of polarization-dependent measurements to the type-I Weyl semimetals in Secs. 3.4.1 and 3.4.2. As in the type-I Weyl semimetals, different response of these bands to light polarizations indicates their different orbital character. Results obtained with p- and s-polarized light together with calculated bands projected onto different orbitals [Fig. 3.11(d)] and the CDAD together with calculated bands projected onto the orbital angular momentum [Fig. 3.15(a)] clarified the full orbital texture of topologically non-trivial bands in the type-I Weyl semimetals. We need such theoretical support to fully understand our observation. We will make a more detailed discussion regarding the orbital texture and its link to the band structure topology in Sec. 7.4.

6.4 Summary

We succeeded in obtaining a clean CoSi(100) surface by sputtering and annealing. Compared to the frequently used cleavage, this procedure leads to reproducible surface quality. We characterized two samples by electron diffraction, and determined the handedness of the chiral crystals and accordingly the Chern number in connection with the Fermi velocity of the observed Fermi arc. By performing photon-energy dependent measurements, we identify bulk states, e.g., the bulk Dirac (BD) cone and the bulk flat (BF) band that compose an unconventional higher-topological-charge fermion. We also identify surface states, e.g., the Fermi arc (FA). We clarified the van Hove singularity of the helicoid Fermi arc. We revealed the polarization dependence of these bands for the first time in chiral topological semimetals. Since differently polarized light probes orbital characters, rich photoemission-intensity variations for different states and even within the same states suggest rich orbital textures. The bulk flat band is sensitive to p-polarization, suggesting that it mainly consists of even orbitals. The bulk Dirac cone and the bulk flat band exhibit a strong circular dichroism with an opposite signal, while the Fermi arc exhibit a weak circular dichroism. The abrupt intensity change of the bulk Dirac cone and the bulk flat band suggests that the orbital character of these bands abruptly changes even within the same state. Overall, different response of these bands to polarizations is attributed to their different orbital character. The circular-dichroism measurements with different samples with the opposite structural handedness give evidence that the sign of the circular dichroism of the bulk states with a chiral band-dispersion shape is reversed between chiral crystals of an opposite handedness.

7 Discussion

7.1 Overview

As summarized in Table 7.1, we studied the type-II Dirac semimetal $NiTe_2$, the type-II Weyl semimetal $MoTe_2$, and the chiral topological semiemtal CoSi, where different topological phases, encoded by the Chern number, emerge depending on the crystal

	$NiTe_2$	$1T_d$-$MoTe_2$	CoSi
	Type-II Dirac semimetal	Type-II Weyl semimetal	Chiral topological semimetal
Crystal structure	Preserved space-inversion symmetry	Broken space-inversion symmetry	Chiral
Chern number	0	±1	±2 (±4)
Spin texture	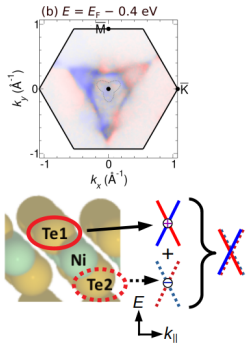	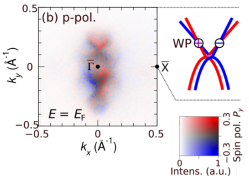	
Orbital texture		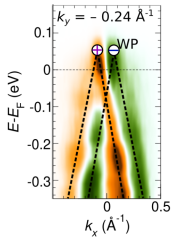	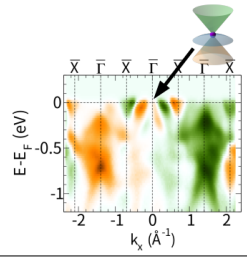

Table 7.1: Unconventional topological semimetals studied in this thesis.

structure. The lower symmetries are, the higher the Chen number is that can be realized. We experimentally deduced the Chern number from the number of Fermi arcs based on the bulk-boundary correspondence described in Sec. 2.2.3. In $MoTe_2$, we found the Chern number $C = \pm 1$ manifested as one Fermi arc connecting one pair of Weyl points. In the case of CoSi, terminated points of two long Fermi arcs share one Weyl point, suggesting the Chern number $C = \pm 2$ (For details of the Chern number analysis see Fig. 6.2 and Sec. 6.1).

Symmetries also affect the spin degree of band structures in connection with spin-orbit coupling, in general. As described in Sec. 2.3.1, all bulk bands must be spin degenerate in non-magnetic space-inversion symmetric materials, e.g., $NiTe_2$, even with SOC. Nevertheless, we observed spin polarized bulk bands in $NiTe_2$ as shown in Sec. 4.4 due to the lower symmetry of the surface probed by surface sensitive VUV light, later discussed in detail in Sec. 7.2. If space-inversion symmetry is broken, e.g., in the case of $MoTe_2$ and CoSi, bulk bands can be spin polarized in inclusion of SOC. In $MoTe_2$, this manifests in an observed spin polarization of the bulk bands as shown in Sec. 5.4. In CoSi, however, we did not observe spin-split bands, which were predicted theoretically as outlined in Sec. 2.5.3, within our experimental resolution. We thus conclude that CoSi possesses a quite weak SOC, consistent with previous reports [114, 116, 117]. SOC play a crucial role to realize a Weyl-semimetal phase in $MoTe_2$ and a Dirac-semimetal phase in $NiTe_2$. In contrast, the chiral topological semimetal CoSi does not necessarily require SOC to realize a topological phase.

Up to now, we have seen that symmetries affect, in general, the spin degree of freedom of the electronic states, and topological phases encoded by the Chern number. Band structure topology is characterized by the Berry curvature field and the Chern number (see Sec. 2.2.2), which are closely related to the orbital texture as descried in Sec. 3.4. Our motivation is to understand the spin and orbital texture of topological non-trivial bands. In the following sections, with the help of thin film band structure calculation and symmetry arguments, we further strengthen our conclusion and discuss the relationship between spin- and orbital-dependent band structures and topology, especially, the topological chiral charge.

7.2 Spin texture of the Dirac and Weyl cones

In this section, we connect the observed spin textures of the Dirac cone in $NiTe_2$ and Weyl cones in $MoTe_2$. As described in Sec. 5.4, a pair of Weyl cones in $MoTe_2$ was found to exhibit a reversed spin texture, where the spin splitting is caused by combination of SOC and the broken inversion symmetry of the $1T_d$ crystal structure in the bulk. We would like to compare our experimental results with theoretical calculations performed in collaboration with Dr. Philipp Rüßmann as shown in Fig. 7.1. Density functional theory (DFT) calculations were carried out for an eight layer thick film of $MoTe_2$ in the same way as described for the case of $NiTe_2$ in Sec. 4.2. Further details on the calculation setup can be found in Ref. [92]. Figures 7.1 (a, b) show the calculated spin-polarized Fermi-surface contour and the band-dispersion map at

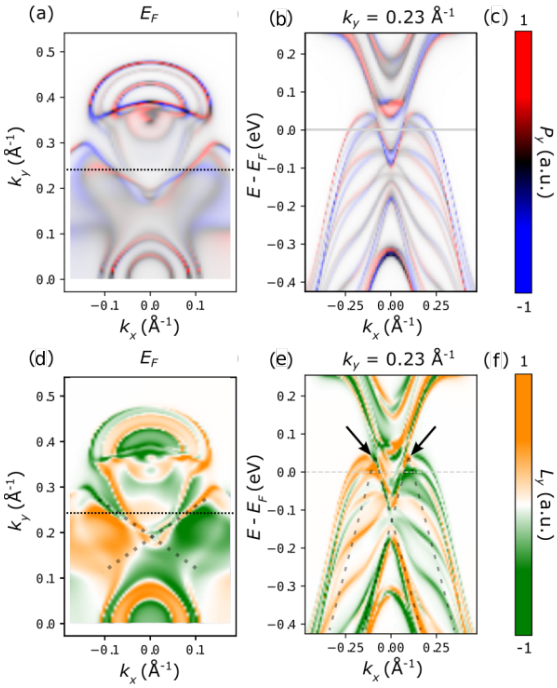

Figure 7.1: Calculated spin polarization and orbital angular momentum. The spin polarization P_y (a, b) and the orbital angular momentum L_y (d, e) plotted on Fermi surfaces (a, d) and band dispersions (b, e) is integrated over the central two $MoTe_2$ layers of the eight layer film to account for the bulk-like character. The color scales of P_y and L_y are given in (c) and (f), respectively. The dashed grey lines in panel (d) and the arrows in panel (e) serve as guides to the eye and indicate the position of the Weyl points.

k_y = 0.23 Å^{-1} cutting through the WPs, respectively. The calculated spin polarization in Fig. 7.1 indicates the bulk-like character integrated over the central 2 layers of a 8-layer thick $MoTe_2$ film. As in the experiments, the spin polarization along the k_y direction is shown. Careful inspection of the boundary between the electron- and hole-pockets in the calculated Fermi surface [Fig. 7.1(a)] reveals a spin texture similar to our experimental result excited by p-polarized light in Fig. 5.7(b). The good agreement of the measurements with the calculation clarified that this experiment mainly probes bulk-like states. Furthermore, our calculation confirms the spin-splitting of the Weyl cone states, that we have observed experimentally by p-polarized light. We can therefore conclude that the observed spin texture of even orbitals, probed by p-polarized light in Fig. 5.7(b), closely corresponds to the ground state spin texture of $MoTe_2$.

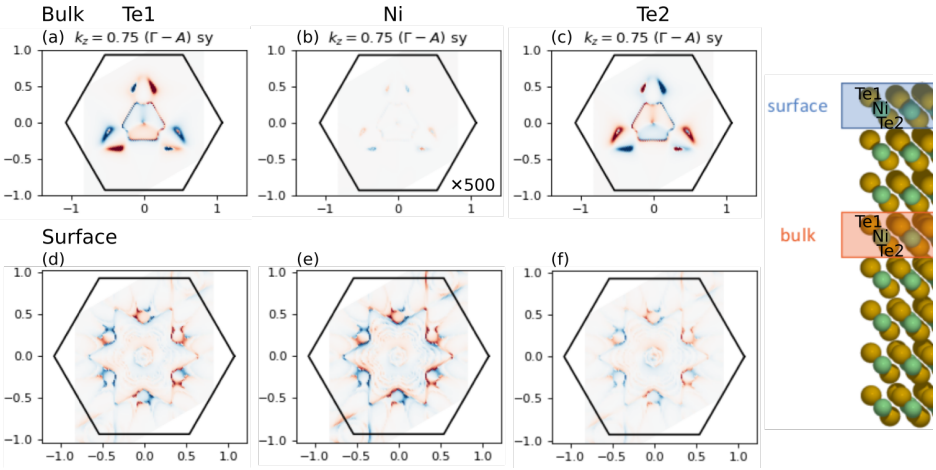

Figure 7.2: Calculated layer-resolved spin polarization. y-component of spin polarization on the bulk Fermi surface at $k_z = 0.75\frac{\pi}{c}$ (a-c) and on the surface Fermi surface (d-f) in the top Te (Te1) (a, d), the Ni (b, e), and the bottom Te (Te2) (c, f) atoms are indicated. Plotted spin polarization in the Ni layer for bulk (b) is multiplied by a factor of 500. An inset on the right hand side shows each atom composing $NiTe_2$. In the bulk, the Te1 and Te2 layers exhibit opposite spin contribution and spin polarization vanishes in the Ni layer. At the surface, all layers exhibit the same spin sign.

In $NiTe_2$, we observed a non-vanishing spin polarization in the bulk as described in Sec. 4.4. However, all bulk bands must be spin degenerate in non-magnetic materials, which naturally preserves time-reversal symmetry, with space-inversion symmetry due to the Kramers theorem described in Sec. 2.3.1. As shown in Fig. 7.2, we performed layer-resolved calculations. In the bulk [Fig. 7.2(a-c)], we found that (i) contribution to the spin from the top Te layer (Te1) and the bottom Te layer (Te2) is opposite. (ii) Spin polarization from the Ni layer is negligible.

This can be generalized as follows. Even in crystals with inversion symmetry, local atomic site asymmetries rather than the global symmetry induce a local "hidden" spin polarization [195]. Such a local spin polarization arises in two separate sectors forming the inversion partners, e.g., the top and bottom Te layers in $NiTe_2$. The inversion partners with opposite spin polarization are degenerate in energy, which compensates the total spin polarization. In $NiTe_2$, the Te layers have compensating spin polarization and in Ni spin polarization vanishes since it is located in the inversion center [195, 196]. In sharp contrast to the bulk, layer-resolved spin polarization at the surface shows different behavior and all layers exhibit the same spin sign as shown in Fig. 7.2(d-f).

Considering the lattice constant $c = 5.2699$Å [80] and the escape depth of $5 - 10$ Å of photoelectrons excited by VUV light (see Sec. 3.1.4), we assume that the first two Te-Ni-Te trilayers can be probed. There is a decay in the probing depth which means

that in this stack of layers Vac-Te_1^{top}-Ni_1-Te_1^{bottom}-Te_2^{top}-Ni_2-Te_2^{bottom}-... one sees a stronger contribution from Te_1^{top} than Te_1^{bottom}, i.e, the observed spin of the emitted photoelectrons does not cancel exactly. Then one sees smaller contributions from the second Te_2^{top}-Ni_2-Te_2^{bottom} trilayer, where the signal coming from Te_2^{top} would again be larger than from Te_2^{bottom}. As already seen in Sec. 4.3, we indeed observed the three-fold symmetric B1 and BD bands at $h\nu = 67$ eV, which is a clear signature of the bulk states. Our experiment suggests that bulk states could be enhanced, while surface states could be suppressed due to the low photoemission cross section at this photo energy as in $MoTe_2$. Therefore, we conclude that we observe a "hidden" spin texture originating from the top Te layer in the bulk. In the framework of topology, the degenerate Dirac cone in $NiTe_2$ is formed by a superposition of two Dirac cones coming from the top and bottom Te layers whose spin polarizations are opposite.

In $MoTe_2$, broken inversion symmetry already in the bulk gives rise to spin-split Weyl cones and pairs of non-degenerate chiral charges $C = \pm 1$. We conclude that a reversed spin texture to pairs of Weyl cones is explained by the opposite topological charge as described in Sec. 5.4, since the spin texture of the Weyl cones can be related to the chiral charge of the Weyl points. As in $MoTe_2$, the opposite spin polarization coming from the top and bottom Te layers in $NiTe_2$ is considered to reflect an opposite topological charge $C = \pm 1$. In the bulk, not only the spin but also the topological charge are compensated, corresponding to the topological charge $C = 0$ in Dirac semimetals.

In conclusion, we find the same scenario for $NiTe_2$ and $MoTe_2$: a pair of Weyl cones with opposite chirality exhibits a reversed spin polarization. Depending on the symmetry of the crystal structure, the cones are degenerate in k space for inversion-symmetric $NiTe_2$ and separated for $MoTe_2$ due to broken inversion symmetry. This finding might apply to other topological quantum materials.

7.3 Symmetry-reflected spin texture in transition-metal dichalcogenides

In this section, we discuss the observed spin texture in connection with symmetries. Although TMDCs of the form MX_2 posses a similar layered crystal structure consisting of a stacking of X-M-X trilayers (see Fig. 2.8), different crystal structures lead to different physical properties. Spin-polarization of bulk bands in $MoTe_2$ is caused by a broken space-inversion symmetry in the bulk, while a "hidden" spin polarization in $NiTe_2$ can be observed by lifting the inversion symmetry at the surface. Such a hidden spin polarization has been also observed in semimetallic $2H$–WSe_2 [197] and MoS_2 [198], which preserve inversion symmetry. In this case each atom located in the neighboring trilayer compensates the total spin polarization, while in $1T$–$NiTe_2$ and $PtSe_2$ [196] different Te (Se) atoms within the trilayer compensate the total spin polarization. This difference can be explained by a symmetry argument: in $1T$–$NiTe_2$, by space inversion ($r \rightarrow -r$) the top and bottom Te atoms within the trilayer can be

mapped onto each other, where the top and bottom Te atoms form inversion partners (see Sec. 2.4.5). In the case of $2H$–MoS_2 and WSe_2, each atom can be mapped onto that in the next inequivalent trilayer by space inversion. Therefore, each atom in the neighboring trilayer forms an inversion partner and possesses an opposite spin contribution.

Here, we would like to emphasize that the hidden spin texture is distinct from topological and trivial surface states and Rashba states from a symmetry point of view. The hidden spin texture in $1T$-$NiTe_2$, $2H$-MoS_2 and WSe_2 is bulk states and originates from local atomic site asymmetry in the bulk crystal and can be only seen by probing a finite region e.g., the surface. This means that the probed region is not space-inversion symmetric, allowing the observation of the "hidden" spin polarization. However, in the sum over all layers the total spin polarization vanishes. Topological and trivial surface states and Rashba state are a direct consequence of the lower symmetry at the surface. In this context, these states represent a similar situation as the hidden spin texture. For instance, Rashba states at metallic surface are caused by broken space-inversion symmetry at the surface even in bulk inversion-symmetric metals [199]. However, since these states only exist at the surface, the total spin polarization does not vanish. Indeed, according to the layer-resolved spin polarization at the surface in $NiTe_2$ (Fig. 7.2(d-f)), all layers exhibit the same spin sign.

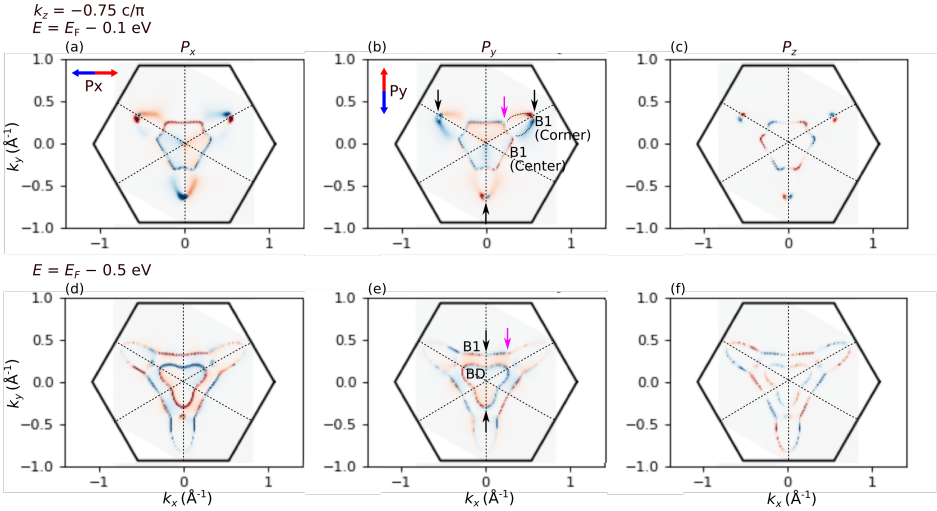

Figure 7.3: Calculated P_x (a, d), P_y (b, e), P_z (c, f) spin polarization. Constant-energy maps at $E = E_F - 0.1$ eV (a-c), $E_F - 0.5$ eV (d-f). P_x, P_y, P_z change sign at the mirror planes on the BD and B1 bands e.g., marked by black arrows and at positions where corner-side parts (B1(Corner)) of the triangle-like B1 band merge with a center part (B1(Center)) as the binding energy is increased, e.g, indicated by purple arrows. Three mirror planes are indicated by black dotted lines.

Here, we summarize symmetries of the observed spin textures in $MoTe_2$ and $NiTe_2$. The observed spin texture is constrained by crystal and time-reversal symmetries. We consider that the spin is an axial vector, i.e., after a mirror operation the spin vector should be flipped. Since $1T_d$-$MoTe_2$ possesses one mirror plane and no rotational symmetry as shown in Fig. 5.4, P_z spin polarization was reported in Ref. [92]. Since $NiTe_2$ possesses a 3-fold rotational symmetry with 3 mirror planes (see Fig. 2.10(b) and Sec. 2.4.5), our calculation shows a 3D spin polarization. For instance, in the case of W(110), no P_z spin polarization is allowed due to a two-fold surface symmetry and time-reversal symmetry [200].

Now we take a closer look at the 3D spin texture in $NiTe_2$. Figure 7.3 shows the calculated P_x, P_y, P_z spin polarization. One can find that P_x, P_y, P_z change sign at the three mirror planes, e.g., marked by black arrows, on the BD and B1 bands and at additional positions between the mirror planes on the B1 band e.g., indicated by purple arrows. For instance, the in-plane spin vector rotates almost 180 degrees on the position indicated by the black arrow as clearly seen in Fig. 4.7(f). The B1 band is actually separated into corner-side parts of the triangle-like band indicated by a dotted

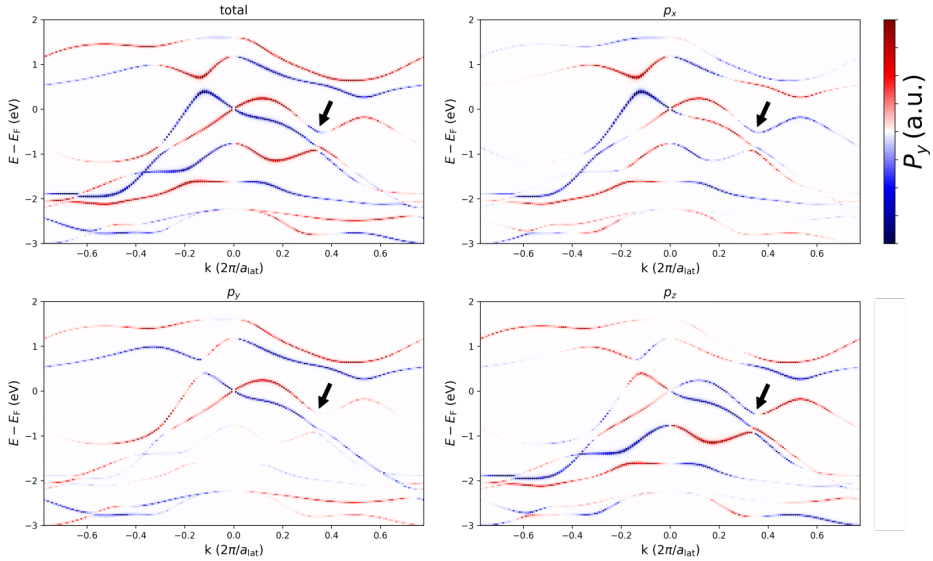

Figure 7.4: Bulk band structure along $\overline{M}-\overline{\Gamma}-\overline{M}'$. The red-white-blue color scale indicates the y-component of the spin polarization in the top Te layer. The four panels indicate the orbital integrated (total) spin polarization $P_y(E,\mathbf{k}) = -\frac{1}{\pi}\mathrm{Im}\mathrm{Tr}\left[\sigma_y G(E,\mathbf{k})\right]$ (in arb. units) as well as the contributions coming from the p_x, p_y and p_z states, respectively. The black arrow highlights a change in the spin polarization direction due to overlapping and partially cancelling contributions from the p_x, p_y, and p_z contributions.

line labeled B1(Corner) and a center part labeled B1(Center) in Fig. 7.3(b). These two parts merge as the binding energy is increased. This merging point corresponds to the spin sign-change position indicated by the purple arrows.

In order to consider the origin of such a complex spin texture, we calculated the orbital-dependent spin polarization. Since the density of states near the Fermi level is dominated by Te p orbitals, we display the spin components projected onto p_x, p_y, and p_z orbitals in the top Te layer in Fig. 7.4. One can see that the bands projected onto different orbitals exhibit a different behavior of spin polarization. In the case of topological surface states in Bi_2Se_3, P_y (P_x) changes sign at the same momentum points $k_x = 0$ ($k_y = 0$) even for different orbitals as described in Fig. 3.12. Unlike Bi_2Se_3, in $NiTe_2$ P_y changes sign at different momentum points for different orbitals. Consequently, the orbital-integrated (total) spin polarization results in a change in the spin polarization direction highlighted by the black arrow due to overlapping and partially cancelling contributions from the p_x, p_y, and p_z contributions. This explains why a complex spin texture arises in $NiTe_2$.

Overall, in this section we have seen that spin polarized and "hidden" spin polarized states arise in connection with the inversion symmetry of a crystal and the spin texture is constrained by crystal and time-reversal symmetries, which is consistent with our observations

7.4 Orbital texture of topological bands

Interaction with circularly polarized light, in general, reflects the chirality of matter. Coupling of chiral Weyl states to an electromagnetic field causes the chiral anomaly as described in Sec. 2.4.2. In the context of optical responses, the correlation between circularly polarized light and the intrinsic chirality of the Weyl states drives an unidirectional photocurrent in response to the respective light helicity [56–58, 123, 124]. In photoemission experiments, the observation of the circular dichroism therefore provides a probe for electronic chirality.

In $MoTe_2$, a pair of Weyl cones exhibits a strong circular dichroism with reversed sign, which reflects the opposite chirality of its wave function as shown in Sec. 5.3. For a deeper understanding of the observed CDAD, we have also calculated the orbital angular momentum L_y in the Fermi surface, shown in Figs. 7.1(d, e). As described in Sec. 3.4.2, it has been shown that the CDAD probes the orbital angular momentum of the wave function. The CDAD can be shown to be approximately proportional to the projection of the orbital angular momentum $\boldsymbol{L}$ on the light propagation direction [166, 169, 173]. A recent study further demonstrates that momentum mapping of the orbital angular momentum reflects the chirality of the Weyl points in a Weyl semimetal [173]. In our experimental geometry, where the light incidence is along the y direction, the observed CDAD is sensitive to the L_y component of the orbital angular momentum.

The orbital momentum of the wave functions on the Fermi level in Fig. 7.1(d) shows a rich texture with sign changes at the positions of the Weyl points. This shows the

correlation between the chirality of the Weyl points and the orbital texture of the electronic structure around them [173]. Considering possible matrix element effects we find a good agreement of the calculated values with our measurements that show a crossing of the changing chirality around $k_y = 0.2\,\text{Å}^{-1}$ (highlighted by dotted lines). Figure 7.1(e) shows an energy-momentum section along the $\overline{\Gamma} - \overline{\text{X}}$ direction. The dispersion of the measured CDAD near the Weyl points (indicated by dashed lines in Fig. 5.6(d)) agrees well with the calculated L_y values (see dashed lines in Fig. 7.1(e)). This observation further supports our conclusion that strong CDAD with reversed sign reflects the opposite chiral charge of the respective Weyl points.

In the case of CoSi, as described in Sec. 6.3, the bulk Dirac cone (BD) and the bulk flat band (BF) that compose an unconventional higher-topological-charge fermion exhibit a strong CDAD with an opposite signal. This suggests that the BD and BF states carry an opposite chiral orbital angular momentum. The CDAD sign of bulk states with a chiral band-dispersion shape is reversed between chiral crystals of a different handedness, suggesting that these states carry an opposite chiral orbital angular momentum. This also shows that the chiral orbital angular momentum is linked to the crystal structure. Thus, the chiral electronic wave functions observed in CoSi reflect structural chirality as well as chiral quasiparticle states. Based on our observation in CoSi as well as $MoTe_2$, the CDAD provides a direct fingerprint of chiral quasiparticle states.

In contrast, the Fermi arc in CoSi exhibits a weak CDAD, and does not carry a large orbital angular momentum. This can be explained when the spin angular momentum is coupled to the orbital angular momentum. The spin-split Fermi arcs carry a mutually opposite spin as shown in Fig. 2.12(b). However, we did not observe the spin-split Fermi arc within our experimental resolution. Thus, the Fermi arc appears to be degenerate in terms of the spin and orbital angular momentum in our measurement (For a detailed description see Sec. 6.3).

As seen in Sec. 5.3, in $MoTe_2$, we observed a signature of a chiral cone below the Fermi level at the $k_x = 0$ line. In the (k_x, k_y) constant-energy contour, this appears as a relative positions of two hole bands with the positive and negative CDAD sign (For details see Fig. 5.5(e).) Since a CDAD due to the asymmetric photoemission geometry should vanish at the $k_x = 0$ line, these states purely reflect an intrinsic chirality of the wave functions (For details see Secs. 3.4.2 and 5.3). These states, which have not been reported so far, can not be reproduced by our calculation and may be only visualized by the CDAD. Whether these states are part of the Weyl topology are still under investigation. We need further theoretical support to conclude this question.

As seen in Fig. 7.1, the calculated P_y and L_y in $MoTe_2$ show different textures. This observation is similar to the type-I Weyl semimetal TaAs [173] [see Figs. 3.15(a, b)]. However, as demonstrated in Fig. 5.7(a), the observed spin texture of the Weyl cone corresponds well to its CDAD texture for s-polarized light. This suggests a correlation between the P_y spin texture related to odd orbitals, probed by s-polarization, and the L_y orbital angular momentum, probed by the CDAD.

As introduced in Sec. 3.4, differently polarized light probes different components orbital of the initial state wave functions. Rich photoemission-intensity variations for

different states and even within the same states in CoSi are observed with differently polarized light. This suggests rich orbital textures. The bulk Dirac cone and the bulk flat band, and the Fermi arc respond all differently to polarizations, suggesting a different orbital character of their bands. As described in Sec. 3.4.1, the different response of the Fermi arc and the bulk-like state in the type-I Weyl semimetal TaP to p- and s-polarization suggests their different orbital characters [154]. In particular, a reversal of the linear dichroism between the Fermi arc and the bulk-like state indicates pronounced switches in the orbital texture, which distinguishes these bands. From our work on CoSi together with the previous study of TaP, we conclude that different topologically non-trivial bands are characterized by their different orbital characters.

A study of TaAs [173] (see Sec. 3.4.2) and our work on $MoTe_2$ confirmed the sign of the Chern number, either plus or minus, by relating it to the orbital angular momentum probed by circular dichroism. We believe that our results of a rich orbital texture in CoSi may experimentally deduce the Chern number of the unconventional fermion, since the orbital texture is closely related to the Berry curvature field [173] described in Sec. 3.4.2. For instance, the abrupt change of the CDAD in the BD band suggests that the orbital angular momentum of this band abruptly changes even within the same state, which is not observed in TaAs or $MoTe_2$. This may be related to the Berry curvature field describing a higher-topological charge. Further theoretical support is needed to fully resolve the orbital texture of CoSi.

8 Conclusion and outlook

We studied the type-II Dirac semimetal $NiTe_2$, the type-II Weyl semimetal $MoTe_2$, and the chiral topological semiemtal CoSi, where different topological phases emerge depending on the crystal structure. We discussed the relationship between spin- and orbital-dependent band structure, symmetry, and topology.

In the type-II Dirac semimetal $NiTe_2$, a spin polarization of bulk states is not allowed for inversion-symmetric materials. An observed "hidden" spin polarization of the bulk Dirac cone originates from the top Te atom of a Te-Ni-Te trilayer, namely, one of the inversion partners. This is because inversion symmetry is broken at the surface when surface sensitive VUV light predominantly probes the top few layers. This is interpreted as a concept where the degenerate Dirac cone in $NiTe_2$ is formed by a superposition of two Dirac cones originating from the top and bottom Te layers whose spin polarizations are opposite. We also give evidence for a helical spin-polarized additional surface Dirac cone below the Fermi level, as in topological insulators.

In the type-II Weyl semimetal $MoTe_2$, we captured a pair of chiral Weyl cones exhibiting a strong circular dichroism with reversed sign, which gives evidence for opposite chiral charges of the respective Weyl points. The observed circular-dichroism texture is further supported by the calculated orbital angular momentum. A pair of spin-split Weyl cones, caused by spin-orbit coupling and broken inversion symmetry, was found to exhibit a opposite spin texture when probed by p-polarized light. The spin texture of the Weyl cones can be explained by the opposite topological charge.

We succeeded in obtaining a clean surface of the chiral topological semimetal CoSi(100) by sputtering and annealing. Compared to the frequently used cleavage, this procedure leads to reproducible surface quality. We determined a handedness of two chiral crystals and accordingly their chiral charge by associating them with the Fermi velocity of the observed Fermi arc. The sign of the circular dichroism of the bulk states with a chiral band dispersion is reversed between chiral crystals of an opposite handedness. We revealed a polarization dependence of the bands forming a higher-charge fermion as well as the Fermi arc. The different response of these bands to light polarizations indicates their different orbital character, attributed to their band structure topology.

In conclusion, the spin texture is strongly influenced by the crystal structure, in general. Furthermore, we clarified that the spin texture of Dirac and Weyl cones can reflect their topological charge: a pair of Weyl cones with opposite chirality exhibits a reversed spin polarization. Depending on the symmetry of the crystal structure, the cones are degenerate in k space for inversion-symmetric $NiTe_2$ and separated for $MoTe_2$ due to broken inversion symmetry. The circular dichroism probes the orbital angular momentum of the electronic wave functions that are linked to chiral

quasiparticle states and structural chirality.

Our experimental works in collaboration with theory stimulate further studies. We showed calculated orbital-dependent spin-polarized band structures in $NiTe_2$. In the future, we would like to perform spin-resolved measurements with differently polarized light such that the spin of specific orbitals can be probed. This will further extend our knowledge of the relationship between the spin and orbital texture of the bulk Dirac cones, which is currently limited to the surface Dirac cone in topological insulators. In order to fully understand the observed polarization-dependent band structures in CoSi, we need band structure calculations projected onto different orbitals. In this way, we can further discuss the relationship between orbital texture and band structure topology, which may provide a fingerprint of its higher-charge fermion. As shown in Fig. 2.12, the width of the spin-split Fermi arcs are small due to weak SOC in CoSi. It was therefore not possible to resolve the splitting within our experimental resolution. Stronger SOC gives rise to a larger width of the spin-split Fermi arcs, which can be resolved experimentally. In order to clarify the spin texture of the Fermi arc in chiral topological semimetals, we would like to perform spin-resolved measurement on strong SOC materials PtGa [120] and PtGa [121].

As we have seen, symmetries play an important role to realize topological quantum materials and lower symmetries can give rise to new exotic topological quantum materials. In this thesis, we studied these materials in terms of the crystal structure in 3D. This aspect can be further extended by realizing lower symmetries in different ways. Low dimensionality such as atomic-layer topological quantum materials can be interesting [201]. Breaking of time-reversal symmetry can be another way to realize lower symmetries. Time-reversal-symmetry breaking in magnetic topological quantum materials [202] can interesting, where magnetism and chirality can meet topology. Since light breaks time-reversal symmetry, light-induced topological quantum materials can be another candidate [203]. These future studies together with our current works will contribute to extending a full picture of topological quantum materials in connection with symmetries, exploring new materials and phenomena, and a deeper understanding of electronic structure as well as spin- and orbital-related phenomena.

Bibliography

[1] P. A. M. Dirac, "The quantum theory of the electron", Proc. R. Soc. London A. **117**, 610 (1928) (cit. on pp. 1, 5).

[2] H. Weyl, "Gravitation and the electron", Proc. Natl. Acad. Sci. U. S. A. **15**, 323 (1929) (cit. on pp. 1, 5).

[3] M. Z. Hasan and C. L. Kane, "Colloquium: Topological insulators", Rev. Mod. Phys. **82**, 3045 (2010) (cit. on pp. 1, 7).

[4] B. Q. Lv, T. Qian, and H. Ding, "Experimental perspective on three-dimensional topological semimetals", Rev. Mod. Phys. **93**, 025002 (2021) (cit. on pp. 1, 7, 15–17, 24).

[5] D. J. Thouless, M. Kohmoto, M. P. Nightingale, and M. den Nijs, "Quantized Hall Conductance in a Two-Dimensional Periodic Potential", Phys. Rev. Lett. **49**, 405 (1982) (cit. on pp. 1, 9, 10).

[6] C. Tusche, A. Krasyuk, and J. Kirschner, "Spin resolved bandstructure imaging with a high resolution momentum microscope", Ultramicroscopy **159**, 520 (2015) (cit. on pp. 2, 37, 39, 41).

[7] S. Suga and C. Tusche, "Photoelectron spectroscopy in a wide $h\nu$ region from 6eV to 8keV with full momentum and spin resolution", J. Electron. Spectrosc. Relat. Phenom. **200**, 119 (2015) (cit. on pp. 2, 29, 39, 41).

[8] G. Schönhense, "Circular dichroism and spin polarization in photoemission from adsorbates and non-magnetic solids", Phys. Scr. **1990**, 255 (1990) (cit. on pp. 2, 48, 50).

[9] J. Ma, K. Deng, L. Zheng, S. Wu, Z. Liu, S. Zhou, and D. Sun, "Experimental progress on layered topological semimetals", 2D Mater. **6**, 032001 (2019) (cit. on pp. 2, 19).

[10] G. Chang, B. J. Wieder, F. Schindler, D. S. Sanchez, I. Belopolski, S.-M. Huang, B. Singh, D. Wu, T.-R. Chang, T. Neupert, X. Su-Yang, H. Lin, and M. Z. Hasan, "Topological quantum properties of chiral crystals", Nat. Mater. **17**, 978 (2018) (cit. on pp. 2, 24, 25, 28).

[11] A. A. Soluyanov, D. Gresch, Z. Wang, Q. Wu, M. Troyer, X. Dai, and B. A. Bernevig, "Type-II Weyl semimetals", Nature **527**, 495 (2015) (cit. on pp. 2, 18, 19).

[12] B. Bradlyn, J. Cano, Z. Wang, M. G. Vergniory, C. Felser, R. J. Cava, and B. A. Bernevig, "Beyond Dirac and Weyl fermions: Unconventional quasiparticles in conventional crystals", Science **353**, 6299 (2016) (cit. on pp. 2, 23).

[13] Y. Ando, "Topological Insulator Materials", J. Phys. Soc. Jpn. **82**, 102001 (2013) (cit. on p. 7).

[14] A. Burkov, "Topological semimetals", Nat. Mater. **15**, 1145 (2016) (cit. on p. 7).

[15] N. P. Armitage, E. J. Mele, and A. Vishwanath, "Weyl and Dirac semimetals in three-dimensional solids", Rev. Mod. Phys. **90**, 015001 (2018) (cit. on pp. 7, 15, 16, 46).

[16] H. Zhang, C.-X. Liu, X.-L. Qi, X. Dai, Z. Fang, and S.-C. Zhang, "Topological insulators in Bi_2Se_3, Bi_2Te_3 and Sb_2Te_3 with a single Dirac cone on the surface", Nat. Phys. **5**, 438 (2009) (cit. on pp. 8, 15).

[17] S. Murakami, "Phase transition between the quantum spin Hall and insulator phases in 3D: emergence of a topological gapless phase", New J. Phys. **9**, 356 (2007) (cit. on p. 8).

[18] M. V. Berry, "Quantal phase factors accompanying adiabatic changes", Proceedings of the Royal Society of London. A. Mathematical and Physical Sciences **392**, 45 (1984) (cit. on p. 9).

[19] D. Xiao, M.-C. Chang, and Q. Niu, "Berry phase effects on electronic properties", Rev. Mod. Phys. **82**, 1959 (2010) (cit. on p. 9).

[20] M. Kohmoto, "Topological invariant and the quantization of the Hall conductance", Ann. Phys. (NY) **160**, 343 (1985) (cit. on p. 10).

[21] R. Kubo, "Statistical-Mechanical Theory of Irreversible Processes. I. General Theory and Simple Applications to Magnetic and Conduction Problems", J. Phys. Soc. Jpn. **12**, 570 (1957) (cit. on p. 10).

[22] K. v. Klitzing, G. Dorda, and M. Pepper, "New Method for High-Accuracy Determination of the Fine-Structure Constant Based on Quantized Hall Resistance", Phys. Rev. Lett. **45**, 494 (1980) (cit. on p. 10).

[23] R. B. Laughlin, "Quantized Hall conductivity in two dimensions", Phys. Rev. B **23**, 5632 (1981) (cit. on p. 10).

[24] B. I. Halperin, "Quantized Hall conductance, current-carrying edge states, and the existence of extended states in a two-dimensional disordered potential", Phys. Rev. B **25**, 2185 (1982) (cit. on p. 10).

[25] Y. Hatsugai, "Topological aspects of the quantum Hall effect", J. Phys.: Condens. Matter **9**, 2507 (1997) (cit. on p. 10).

[26] F. D. M. Haldane, "Model for a Quantum Hall Effect without Landau Levels: Condensed-Matter Realization of the "Parity Anomaly"", Phys. Rev. Lett. **61**, 2015 (1988) (cit. on p. 10).

[27] I. Belopolski, S.-Y. Xu, D. S. Sanchez, G. Chang, C. Guo, M. Neupane, H. Zheng, C.-C. Lee, S.-M. Huang, G. Bian, N. Alidoust, T.-R. Chang, B. Wang, X. Zhang, A. Bansil, H.-T. Jeng, H. Lin, S. Jia, and M. Z. Hasan, "Criteria for Directly Detecting Topological Fermi Arcs in Weyl Semimetals", Phys. Rev. Lett. **116**, 066802 (2016) (cit. on p. 11).

[28] L. Fu and C. L. Kane, "Topological insulators with inversion symmetry", Phys. Rev. B **76**, 045302 (2007) (cit. on pp. 13–15).

[29] C. L. Kane and E. J. Mele, "Z_2 Topological Order and the Quantum Spin Hall Effect", Phys. Rev. Lett. **95**, 146802 (2005) (cit. on pp. 13, 14).

[30] C. L. Kane and E. J. Mele, "Quantum Spin Hall Effect in Graphene", Phys. Rev. Lett. **95**, 226801 (2005) (cit. on p. 13).

[31] B. A. Bernevig and S.-C. Zhang, "Quantum Spin Hall Effect", Phys. Rev. Lett. **96**, 106802 (2006) (cit. on p. 13).

[32] L. Fu and C. L. Kane, "Time reversal polarization and a Z_2 adiabatic spin pump", Phys. Rev. B **74**, 195312 (2006) (cit. on pp. 14, 15).

[33] L. Fu, C. L. Kane, and E. J. Mele, "Topological Insulators in Three Dimensions", Phys. Rev. Lett. **98**, 106803 (2007) (cit. on p. 14).

[34] P. Roushan, J. Seo, C. V. Parker, Y. S. Hor, D. Hsieh, D. Qian, A. Richardella, M. Z. Hasan, R. J. Cava, and A. Yazdani, "Topological surface states protected from backscattering by chiral spin texture", Nature **460**, 1106 (2009) (cit. on p. 15).

[35] D. Hsieh, D. Qian, L. Wray, Y. Xia, Y. S. Hor, R. J. Cava, and M. Z. Hasan, "A topological Dirac insulator in a quantum spin Hall phase", Nature **452**, 970 (2008) (cit. on p. 15).

[36] D. Hsieh, Y. Xia, D. Qian, L. Wray, J. Dil, F. Meier, J. Osterwalder, L. Patthey, J. Checkelsky, N. P. Ong, A. Fedorov, H.-H. Lin, A. Bansil, D. Grauer, Y. Hor, R. Cava, and M. Z. Hasan, "A tunable topological insulator in the spin helical Dirac transport regime", Nature **460**, 1101 (2009) (cit. on pp. 15, 46).

[37] H. Nielsen and M. Ninomiya, "Absence of neutrinos on a lattice: (I). Proof by homotopy theory", Nucl. Phys. B **185**, 20 (1981) (cit. on p. 15).

[38] H. Nielsen and M. Ninomiya, "Absence of neutrinos on a lattice: (II). Intuitive topological proof", Nucl. Phys. B **193**, 173 (1981) (cit. on p. 15).

[39] M. Hirayama, R. Okugawa, and S. Murakami, "Topological Semimetals Studied by Ab Initio Calculations", J. Phys. Soc. Jpn. **87**, 041002 (2018) (cit. on pp. 15, 16).

[40] X. Wan, A. M. Turner, A. Vishwanath, and S. Y. Savrasov, "Topological semimetal and Fermi-arc surface states in the electronic structure of pyrochlore iridates", Phys. Rev. B **83**, 205101 (2011) (cit. on p. 16).

[41] K.-Y. Yang, Y.-M. Lu, and Y. Ran, "Quantum Hall effects in a Weyl semimetal: Possible application in pyrochlore iridates", Phys. Rev. B **84**, 075129 (2011) (cit. on pp. 16, 17).

[42] G. Xu, H. Weng, Z. Wang, X. Dai, and Z. Fang, "Chern Semimetal and the Quantized Anomalous Hall Effect in $HgCr_2Se_4$", Phys. Rev. Lett. **107**, 186806 (2011) (cit. on pp. 16, 17).

[43] F. D. M. Haldane, "Attachment of Surface "Fermi Arcs" to the Bulk Fermi Surface: "Fermi-Level Plumbing" in Topological Metals", arXiv:1401.0529 (2014) (cit. on p. 16).

[44] R. Okugawa and S. Murakami, "Dispersion of Fermi arcs in Weyl semimetals and their evolutions to Dirac cones", Phys. Rev. B **89**, 235315 (2014) (cit. on p. 16).

[45] C. Fang, L. Lu, J. Liu, and L. Fu, "Topological semimetals with helicoid surface states", Nat. Phys. **12**, 936 (2016) (cit. on p. 16).

[46] S.-M. Huang, S.-Y. Xu, I. Belopolski, C.-C. Lee, G. Chang, B. Wang, N. Alidoust, G. Bian, M. Neupane, C. Zhang, S. Jia, A. Bansil, H. Lin, and M. Z. Hasan, "A Weyl Fermion semimetal with surface Fermi arcs in the transition metal monopnictide TaAs class", Nat. Commun. **6**, 7373 (2015) (cit. on pp. 16, 45).

[47] H. Weng, C. Fang, Z. Fang, B. A. Bernevig, and X. Dai, "Weyl Semimetal Phase in Noncentrosymmetric Transition-Metal Monophosphides", Phys. Rev. X **5**, 011029 (2015) (cit. on pp. 16, 45).

[48] S.-Y. Xu, I. Belopolski, N. Alidoust, M. Neupane, G. Bian, C. Zhang, R. Sankar, G. Chang, Z. Yuan, C.-C. Lee, S.-M. Huang, H. Zheng, J. Ma, D. Sanchez, B. Wang, A. Bansil, F. Chou, P. Shibayev, H. Lin, and M. Z. Hasan, "Discovery of a Weyl fermion semimetal and topological Fermi arcs", Science **349**, 613 (2015) (cit. on pp. 16, 45).

[49] M. Z. Hasan, G. Chang, I. Belopolski, G. Bian, S.-Y. Xu, and J.-X. Yin, "Weyl, Dirac and high-fold chiral fermions in topological quantum matter", Nat. Rev. Mater. **6**, 784 (2021) (cit. on pp. 16, 23).

[50] Y.-J. Chen, J.-P. Hanke, M. Hoffmann, G. Bihlmayer, Y. Mokrousov, S. Blügel, C. M. Schneider, and C. Tusche, "Spanning Fermi arcs in a two-dimensional magnet", arXiv:2106.15670 (2021) (cit. on p. 16).

[51] A. Burkov, "Chiral anomaly and transport in Weyl metals", J. Phys.: Condens. Matter **27**, 113201 (2015) (cit. on p. 16).

[52] S. L. Adler, "Axial-Vector Vertex in Spinor Electrodynamics", Phys. Rev. **177**, 2426 (1969) (cit. on p. 16).

[53] J. S. Bell and R. Jackiw, "A PCAC puzzle: $\pi\, 0 \to \gamma\gamma$ in the σ-model", Il Nuovo Cimento A (1965-1970) **60**, 47 (1969) (cit. on p. 16).

[54] H. Nielsen and M. Ninomiya, "The Adler-Bell-Jackiw anomaly and Weyl fermions in a crystal", Phys. Lett. B **130**, 389 (1983) (cit. on p. 16).

[55] A. A. Burkov, "Anomalous Hall Effect in Weyl Metals", Phys. Rev. Lett. **113**, 187202 (2014) (cit. on p. 17).

[56] C.-K. Chan, N. H. Lindner, G. Refael, and P. A. Lee, "Photocurrents in Weyl semimetals", Phys. Rev. B **95**, 041104 (2017) (cit. on pp. 18, 96).

[57] F. de Juan, A. G. Grushin, T. Morimoto, and J. E. Moore, "Quantized circular photogalvanic effect in Weyl semimetals", Nat. Commun. **8**, 15995 (2017) (cit. on pp. 18, 28, 96).

[58] Q. Ma, S.-Y. Xu, C.-K. Chan, C.-L. Zhang, G. Chang, Y. Lin, W. Xie, T. Palacios, H. Lin, S. Jia, P. Lee, P. Jarillo-Herrero, and N. Gedik, "Direct optical detection of Weyl fermion chirality in a topological semimetal", Nat. Phys. **13**, 842 (2017) (cit. on pp. 18, 96).

[59] S. M. Young, S. Zaheer, J. C. Y. Teo, C. L. Kane, E. J. Mele, and A. M. Rappe, "Dirac Semimetal in Three Dimensions", Phys. Rev. Lett. **108**, 140405 (2012) (cit. on p. 18).

[60] Z. Wang, Y. Sun, X.-Q. Chen, C. Franchini, G. Xu, H. Weng, X. Dai, and Z. Fang, "Dirac semimetal and topological phase transitions in A_3Bi (A = Na, K, Rb)", Phys. Rev. B **85**, 195320 (2012) (cit. on p. 18).

[61] B.-J. Yang and N. Nagaosa, "Classification of stable three-dimensional Dirac semimetals with nontrivial topology", Nat Commun **5**, 4898 (2014) (cit. on pp. 18, 23).

[62] B.-J. Yang, T. Morimoto, and A. Furusaki, "Topological charges of three-dimensional Dirac semimetals with rotation symmetry", Phys. Rev. B **92**, 165120 (2015) (cit. on pp. 18, 23).

[63] Z. K. Liu, B. Zhou, Y. Zhang, Z. J. Wang, H. M. Weng, D. Prabhakaran, S.-K. Mo, Z. X. Shen, Z. Fang, X. Dai, Z. Hussain, and Y. L. Chen, "Discovery of a Three-Dimensional Topological Dirac Semimetal, Na_3Bi", Science **343**, 864 (2014) (cit. on p. 18).

[64] Z. Wang, H. Weng, Q. Wu, X. Dai, and Z. Fang, "Three-dimensional Dirac semimetal and quantum transport in Cd_3As_2", Phys. Rev. B **88**, 125427 (2013) (cit. on p. 18).

[65] M. Neupane, S.-Y. Xu, R. Sankar, N. Alidoust, G. Bian, C. Liu, I. Belopolski, T.-R. Chang, H.-T. Jeng, H. Lin, A. Bansil, F. Chou, and M. Z. Hasan, "Observation of a three-dimensional topological Dirac semimetal phase in high-mobility Cd_3As_2", Nat. Commun. **5**, 3786 (2014) (cit. on p. 18).

[66] J. Xiong, S. K. Kushwaha, T. Liang, J. W. Krizan, M. Hirschberger, W. Wang, R. J. Cava, and N. P. Ong, "Evidence for the chiral anomaly in the Dirac semimetal Na_3Bi", Science **350**, 413 (2015) (cit. on p. 18).

[67] S. Tchoumakov, M. Civelli, and M. O. Goerbig, "Magnetic-Field-Induced Relativistic Properties in Type-I and Type-II Weyl Semimetals", Phys. Rev. Lett. **117**, 086402 (2016) (cit. on p. 19).

[68] Z.-M. Yu, Y. Yao, and S. A. Yang, "Predicted Unusual Magnetoresponse in Type-II Weyl Semimetals", Phys. Rev. Lett. **117**, 077202 (2016) (cit. on p. 19).

[69] S. Manzeli, D. Ovchinnikov, D. Pasquier, O. V. Yazyev, and A. Kis, "2D transition metal dichalcogenides", Nat. Rev. Mater. **2**, 1 (2017) (cit. on p. 19).

[70] G. H. Han, D. L. Duong, D. H. Keum, S. J. Yun, and Y. H. Lee, "van der Waals metallic transition metal dichalcogenides", Chem. Rev. **118**, 6297 (2018) (cit. on p. 19).

[71] H. Huang, S. Zhou, and W. Duan, "Type-II Dirac fermions in the $PtSe_2$ class of transition metal dichalcogenides", Phys. Rev. B **94**, 121117 (2016) (cit. on p. 19).

[72] Y. Li, Y. Xia, S. A. Ekahana, N. Kumar, J. Jiang, L. Yang, C. Chen, C. Liu, B. Yan, C. Felser, G. Li, Z. Liu, and Y. Chen, "Topological origin of the type-II Dirac fermions in $PtSe_2$", Phys. Rev. Mater. **1**, 074202 (2017) (cit. on p. 19).

[73] K. Zhang, M. Yan, H. Zhang, H. Huang, M. Arita, Z. Sun, W. Duan, Y. Wu, and S. Zhou, "Experimental evidence for type-II Dirac semimetal in $PtSe_2$", Phys. Rev. B **96**, 125102 (2017) (cit. on p. 19).

[74] M. S. Bahramy, O. Clark, B.-J. Yang, J. Feng, L. Bawden, J. Riley, I. Marković, F. Mazzola, V. Sunko, S. Cooil, M. Jorge, J. Wells, M. Leandersson, T. Balasubramanian, J. Fujii, I. Vobornik, J. Rault, T. Kim, M. Hoesch, and P. King, "Ubiquitous formation of type-II bulk Dirac cones and topological surface states from a single orbital manifold in transition-metal dichalcogenides", Nat. Mater. **17**, 21 (2018) (cit. on pp. 19, 23, 61).

[75] O. Clark, F. Mazzola, I. Marković, J. Riley, J. Feng, B.-J. Yang, K. Sumida, T. Okuda, J. Fujii, I. Vobornik, T. Kim, K. Okawa, T. Sasagawa, M. S. Bahramy, and P. King, "A general route to form topologically-protected surface and bulk Dirac fermions along high-symmetry lines", Electron. Struct. **1**, 014002 (2019) (cit. on pp. 19, 23, 61, 62).

[76] M. Yan, H. Huang, K. Zhang, E. Wang, W. Yao, K. Deng, G. Wan, H. Zhang, M. Arita, H. Yang, Z. Sun, H. Yao, Y. Wu, S. Fan, W. Duan, and S. Zhou, "Lorentz-violating type-II Dirac fermions in transition metal dichalcogenide $PtTe_2$", Nat. Commun. **8**, 257 (2017) (cit. on p. 19).

[77] H.-J. Noh, J. Jeong, E.-J. Cho, K. Kim, B. I. Min, and B.-G. Park, "Experimental Realization of Type-II Dirac Fermions in a $PdTe_2$ Superconductor", Phys. Rev. Lett. **119**, 016401 (2017) (cit. on p. 19).

[78] F. Fei, X. Bo, R. Wang, B. Wu, J. Jiang, D. Fu, M. Gao, H. Zheng, Y. Chen, X. Wang, H. Bu, F. Song, X. Wan, B. Wang, and G. Wang, "Nontrivial Berry phase and type-II Dirac transport in the layered material $PdTe_2$", Phys. Rev. B **96**, 041201 (2017) (cit. on p. 19).

[79] O. J. Clark, M. J. Neat, K. Okawa, L. Bawden, I. Marković, F. Mazzola, J. Feng, V. Sunko, J. M. Riley, W. Meevasana, J. Fujii, I. Vobornik, T. K. Kim, M. Hoesch, T. Sasagawa, P. Wahl, M. S. Bahramy, and P. D. C. King, "Fermiology and Superconductivity of Topological Surface States in $PdTe_2$", Phys. Rev. Lett. **120**, 156401 (2018) (cit. on p. 19).

[80] C. Xu, B. Li, W.-H. Jiao, W. Zhou, B. Qian, R. Sankar, N. Zhigadlo, Y. Qi, D. Qian, F. Chou, and X. Xu, "Topological Type-II Dirac Fermions Approaching the Fermi Level in a Transition Metal Dichalcogenide $NiTe_2$", Chem. Mater. **30**, 4823 (2018) (cit. on pp. 19, 21, 55, 92).

[81] B. Ghosh, D. Mondal, C.-N. Kuo, C. S. Lue, J. Nayak, J. Fujii, I. Vobornik, A. Politano, and A. Agarwal, "Observation of bulk states and spin-polarized topological surface states in transition metal dichalcogenide Dirac semimetal candidate $NiTe_2$", Phys. Rev. B **100**, 195134 (2019) (cit. on pp. 19, 21, 60, 62).

[82] S. Mukherjee, S. Jung, S. Weber, C. Xu, D. Qian, X. Xu, P. Biswas, T. Kim, L. Chapon, M. Watson, J. Neaton, and C. Cacho, "Fermi-crossing Type-II Dirac fermions and topological surface states in $NiTe_2$", Sci. Rep. **10**, 12957 (2020) (cit. on pp. 19, 21, 22, 60, 62).

[83] Y. Sun, S.-C. Wu, M. N. Ali, C. Felser, and B. Yan, "Prediction of Weyl semimetal in orthorhombic $MoTe_2$", Phys. Rev. B **92**, 161107 (2015) (cit. on pp. 19, 67).

[84] Z. Wang, D. Gresch, A. A. Soluyanov, W. Xie, S. Kushwaha, X. Dai, M. Troyer, R. J. Cava, and B. A. Bernevig, "$MoTe_2$: A Type-II Weyl Topological Metal", Phys. Rev. Lett. **117**, 056805 (2016) (cit. on pp. 19, 67, 72).

[85] T.-R. Chang, S.-Y. Xu, G. Chang, C.-C. Lee, S.-M. Huang, B. Wang, G. Bian, H. Zheng, D. Sanchez, I. Belopolski, N. Alidoust, M. Neupane, A. Bansil, H.-T. Jeng, H. Lin, and M. Z. Hasan, "Prediction of an arc-tunable Weyl Fermion metallic state in $Mo_xW_{1-x}Te_2$", Nat. Commun. **7**, 10639 (2016) (cit. on pp. 19, 67).

[86] K. Deng, G. Wan, P. Deng, K. Zhang, S. Ding, E. Wang, M. Yan, H. Huang, H. Zhang, Z. Xu, J. Denlinger, A. Fedorov, H. Yang, W. Duan, H. Yao, Y. Wu, S. Fan, H. Zhang, X. Chen, and S. Zhou, "Experimental observation of topological Fermi arcs in type-II Weyl semimetal $MoTe_2$", Nat. Phys. **12**, 1105 (2016) (cit. on pp. 19, 67).

[87] A. Tamai, Q. S. Wu, I. Cucchi, F. Y. Bruno, S. Riccò, T. K. Kim, M. Hoesch, C. Barreteau, E. Giannini, C. Besnard, A. A. Soluyanov, and F. Baumberger, "Fermi Arcs and Their Topological Character in the Candidate Type-II Weyl Semimetal $MoTe_2$", Phys. Rev. X **6**, 031021 (2016) (cit. on pp. 19, 66, 67).

[88] J. Jiang, Z. Liu, Y. Sun, Y. Haifeng, C. Rajamathi, Y. Qi, L. Yang, C. Chen, H. Peng, C. Hwang, S. Sun, S.-K. Mo, I. Vobornik, J. Fujii, S. Parkin, C. Felser, B. Yan, and Y. Chen, "Signature of type-II Weyl semimetal phase in $MoTe_2$", Nat. Commun. **8**, 13973 (2017) (cit. on pp. 19, 67).

[89] A. Crepaldi, G. Autès, A. Sterzi, G. Manzoni, M. Zacchigna, F. Cilento, I. Vobornik, J. Fujii, P. Bugnon, A. Magrez, H. Berger, F. Parmigiani, O. V. Yazyev, and M. Grioni, "Persistence of a surface state arc in the topologically trivial phase of $MoTe_2$", Phys. Rev. B **95**, 041408 (2017) (cit. on pp. 19, 67, 73).

[90] M. Sakano, M. S. Bahramy, H. Tsuji, I. Araya, K. Ikeura, H. Sakai, S. Ishiwata, K. Yaji, K. Kuroda, A. Harasawa, S. Shin, and K. Ishizaka, "Observation of spin-polarized bands and domain-dependent Fermi arcs in polar Weyl semimetal $MoTe_2$", Phys. Rev. B **95**, 121101 (2017) (cit. on pp. 19, 67, 73).

[91] P. Rüßmann, A. P. Weber, F. Glott, N. Xu, M. Fanciulli, S. Muff, A. Magrez, P. Bugnon, H. Berger, M. Bode, J. H. Dil, S. Blügel, P. Mavropoulos, and P. Sessi, "Universal scattering response across the type-II Weyl semimetal phase diagram", Phys. Rev. B **97**, 075106 (2018) (cit. on pp. 19, 21, 67, 72).

[92] A. P. Weber, P. Rüßmann, N. Xu, S. Muff, M. Fanciulli, A. Magrez, P. Bugnon, H. Berger, N. C. Plumb, M. Shi, S. Blügel, P. Mavropoulos, and J. H. Dil, "Spin-Resolved Electronic Response to the Phase Transition in $MoTe_2$", Phys. Rev. Lett. **121**, 156401 (2018) (cit. on pp. 19, 66, 67, 73, 90, 95).

[93] S. Singh, J. Kim, K. M. Rabe, and D. Vanderbilt, "Engineering Weyl Phases and Nonlinear Hall Effects in T_d-$MoTe_2$", Phys. Rev. Lett. **125**, 046402 (2020) (cit. on p. 19).

[94] B. E. Brown, "The crystal structures of WTe_2 and high-temperature $MoTe_2$", Acta Crystallogr. **20**, 268 (1966) (cit. on p. 19).

[95] R. Clarke, E. Marseglia, and H. Hughes, "A low-temperature structural phase transition in β-$MoTe_2$", Philos. Mag. B **38**, 121 (1978) (cit. on pp. 19, 68).

[96] X. Qian, J. Liu, L. Fu, and J. Li, "Quantum spin Hall effect in two-dimensional transition metal dichalcogenides", Science **346**, 1344 (2014) (cit. on p. 19).

[97] M. Ali, J. Xiong, S. Flynn, J. Tao, Q. Gibson, L. Schoop, T. Liang, N. Haldolaarachchige, M. Hirschberger, N. Ong, and R. Cava, "Large, non-saturating magnetoresistance in WTe_2", Nature **514**, 205 (2014) (cit. on p. 19).

[98] F. C. Chen, H. Y. Lv, X. Luo, W. J. Lu, Q. L. Pei, G. T. Lin, Y. Y. Han, X. B. Zhu, W. H. Song, and Y. P. Sun, "Extremely large magnetoresistance in the type-II Weyl semimetal $MoTe_2$", Phys. Rev. B **94**, 235154 (2016) (cit. on p. 19).

[99] Y. Wang, E. Liu, H. Liu, Y. Pan, L. Zhang, J. Zeng, Y. Fu, M. Wang, K. Xu, Z. Huang, Z. Wang, H. Lu, D. Xing, B. Wang, X. Wan, and F. Miao, "Gate-tunable negative longitudinal magnetoresistance in the predicted type-II Weyl semimetal WTe_2", Nat. Commun. **7**, 13142 (2016) (cit. on p. 19).

[100] K. Ikeura, H. Sakai, M. S. Bahramy, and S. Ishiwata, "Rich structural phase diagram and thermoelectric properties of layered tellurides $Mo_{1-x}Nb_xTe_2$", APL Mater. **3**, 041514 (2015) (cit. on p. 19).

[101] H. Sakai, K. Ikeura, M. S. Bahramy, N. Ogawa, D. Hashizume, J. Fujioka, Y. Tokura, and S. Ishiwata, "Critical enhancement of thermopower in a chemically tuned polar semimetal $MoTe_2$", Sci. Adv. **2**, e1601378 (2016) (cit. on p. 19).

[102] Y. Qi, P. Naumov, M. Ali, C. Rajamathi, O. Barkalov, Y. Sun, C. Shekhar, S.-C. Wu, V. Süß, M. Schmidt, E. Pippel, P. Werner, R. Hillebrand, T. Förster, E. Kampertt, W. Schnelle, S. Parkin, R. Cava, C. Felser, and S. Medvedev, "Superconductivity in Weyl Semimetal Candidate $MoTe_2$", Nat. Commun. **7**, 11038 (2016) (cit. on p. 19).

[103] H. Takahashi, T. Akiba, K. Imura, T. Shiino, K. Deguchi, N. K. Sato, H. Sakai, M. S. Bahramy, and S. Ishiwata, "Anticorrelation between polar lattice instability and superconductivity in the Weyl semimetal candidate $MoTe_2$", Phys. Rev. B **95**, 100501 (2017) (cit. on p. 19).

[104] S. Mühlbauer, B. Binz, F. Jonietz, C. Pfleiderer, A. Rosch, A. Neubauer, R. Georgii, and P. Böni, "Skyrmion Lattice in a Chiral Magnet", Science **323**, 915 (2009) (cit. on p. 24).

[105] X. Yu, Y. Onose, N. Kanazawa, J. H. Park, J. Han, Y. Matsui, N. Nagaosa, and Y. Tokura, "Real-space observation of a two-dimensional skyrmion crystal", Nature **465**, 901 (2010) (cit. on p. 24).

[106] Y. Tokura and N. Kanazawa, "Magnetic Skyrmion Materials", Chem. Rev. **121**, 2857 (2020) (cit. on p. 24).

[107] S. Grytsiuk, J.-P. Hanke, M. Hoffmann, J. Bouaziz, O. Gomonay, G. Bihlmayer, S. Lounis, Y. Mokrousov, and S. Blügel, "Topological–chiral magnetic interactions driven by emergent orbital magnetism", Nat. Commun. **11**, 511 (2020) (cit. on p. 24).

[108] T. Ou-Yang, Y. Zhuang, B. Ramachandran, W. Chen, G. Shu, C. Hu, F. Chou, and Y. Kuo, "Effect of Co substitution on thermoelectric properties of FeSi", J. Alloy. Compd. **702**, 92 (2017) (cit. on p. 24).

[109] P. Tang, Q. Zhou, and S.-C. Zhang, "Multiple Types of Topological Fermions in Transition Metal Silicides", Phys. Rev. Lett. **119**, 206402 (2017) (cit. on pp. 25, 82, 86).

[110] G. Chang, S.-Y. Xu, B. J. Wieder, D. S. Sanchez, S.-M. Huang, I. Belopolski, T.-R. Chang, S. Zhang, A. Bansil, H. Lin, and M. Z. Hasan, "Unconventional Chiral Fermions and Large Topological Fermi Arcs in RhSi", Phys. Rev. Lett. **119**, 206401 (2017) (cit. on pp. 25, 28).

[111] D. Pshenay-Severin, Y. V. Ivanov, A. Burkov, and A. Burkov, "Band structure and unconventional electronic topology of CoSi", J. Phys.: Condens. Matter **30**, 135501 (2018) (cit. on pp. 25, 26, 82, 86).

[112] D. A. Pshenay-Severin and A. T. Burkov, "Electronic structure of B20 (FeSi-type) transition-metal monosilicides", Materials **12**, 2710 (2019) (cit. on pp. 25, 82, 86).

[113] S. Nikolaev, D. Pshenay-Severin, Y. Ivanov, and A. Burkov, "Effect of deformation on topological properties of cobalt monosilicide", Crystals **11**, 143 (2021) (cit. on p. 25).

[114] Z. Rao, H. Li, T. Zhang, S.-J. Tian, L. Chenghe, B. Fu, C. Tang, L. Wang, Z. Li, W. Fan, J. Li, Y. Huang, H. Lei, Y. Long, C. Fang, H. Weng, Y. Shi, Y. Sun, T. Qian, and H. Ding, "Observation of unconventional chiral fermions with long Fermi arcs in CoSi", Nature **567**, 496 (2019) (cit. on pp. 25, 26, 82, 86, 90).

[115] N. Huber, K. Alpin, G. L. Causer, L. Worch, A. Bauer, G. Benka, M. M. Hirschmann, A. P. Schnyder, C. Pfleiderer, and M. A. Wilde, "Network of topological nodal planes, multifold degeneracies, and Weyl points in CoSi", arXiv:2107.02820 (2021) (cit. on p. 25).

[116] D. Takane, Z. Wang, S. Souma, K. Nakayama, T. Nakamura, H. Oinuma, Y. Nakata, H. Iwasawa, C. Cacho, T. Kim, K. Horiba, H. Kumigashira, T. Takahashi, Y. Ando, and T. Sato, "Observation of Chiral Fermions with a Large Topological Charge and Associated Fermi-Arc Surface States in CoSi", Phys. Rev. Lett. **122**, 076402 (2019) (cit. on pp. 26, 77, 86, 90).

[117] D. S. Sanchez, I. Belopolski, T. A. Cochran, X. Xu, J.-X. Yin, G. Chang, W. Xie, K. Manna, V. Süß, C.-Y. Huang, N. Alidoust, D. Multer, S. Zhang, N. Shumiya, X. Wang, G.-Q. Wang, T.-R. Chang, C. Felser, S.-Y. Xu, and M. Z. Hasan, "Topological chiral crystals with helicoid-arc quantum states", Nature **567**, 500 (2019) (cit. on pp. 26, 82, 86, 90).

[118] N. B. Schröter, D. Pei, M. G. Vergniory, Y. Sun, K. Manna, F. De Juan, J. A. Krieger, V. Süss, M. Schmidt, P. Dudin, B. Bradlyn, T. Kim, T. Schmitt, C. Cacho, C. Felser, V. Strocov, and Y. Chen, "Chiral topological semimetal with multifold band crossings and long Fermi arcs", Nat. Phys. **15**, 759 (2019) (cit. on p. 26).

[119] H. Li, S. Xu, Z.-C. Rao, L.-Q. Zhou, Z.-J. Wang, S.-M. Zhou, S.-J. Tian, S.-Y. Gao, J.-J. Li, Y.-B. Huang, H.-C. Lei, H. Weng, Y.-J. Sun, T.-L. Xia, T. Qian, and H. Ding, "Chiral fermion reversal in chiral crystals", Nat. Commun. **10**, 5505 (2019) (cit. on p. 26).

[120] N. B. M. Schröter, S. Stolz, K. Manna, F. de Juan, M. G. Vergniory, J. A. Krieger, D. Pei, T. Schmitt, P. Dudin, T. K. Kim, C. Cacho, B. Bradlyn, H. Borrmann, M. Schmidt, R. Widmer, V. N. Strocov, and C. Felser, "Observation and control of maximal Chern numbers in a chiral topological semimetal", Science **369**, 179 (2020) (cit. on pp. 26, 27, 80, 100).

[121] M. Yao, K. Manna, Q. Yang, A. Fedorov, V. Voroshnin, B. Schwarze, J. Hornung, S. Chattopadhyay, Z. Sun, S. Guin, J. Wosnitza, H. Borrmann, C. Shekhar, N. Kumar, J. Fink, Y. Sun, and C. Felser, "Observation of giant spin-split Fermi-arc with maximal Chern number in the chiral topological semimetal PtGa", Nat. Commun. **11**, 2033 (2020) (cit. on pp. 26, 100).

[122] F. Flicker, F. de Juan, B. Bradlyn, T. Morimoto, M. G. Vergniory, and A. G. Grushin, "Chiral optical response of multifold fermions", Phys. Rev. B **98**, 155145 (2018) (cit. on p. 28).

[123] D. Rees, K. Manna, B. Lu, T. Morimoto, H. Borrmann, C. Felser, J. E. Moore, D. H. Torchinsky, and J. Orenstein, "Helicity-dependent photocurrents in the chiral Weyl semimetal RhSi", Sci. Adv. **6**, eaba0509 (2020) (cit. on pp. 28, 96).

[124] Z. Ni, K. Wang, Y. Zhang, O. Pozo, B. xu, X. Han, K. Manna, J. Paglione, C. Felser, A. Grushin, F. Juan, E. Mele, and L. Wu, "Giant topological longitudinal circular photo-galvanic effect in the chiral multifold semimetal CoSi", Nat. Commun. **12**, 154 (2021) (cit. on pp. 28, 96).

[125] D. S. Sanchez, T. A. Cochran, I. Belopolski, Z.-J. Cheng, X. P. Yang, Y. Liu, X. Xu, K. Manna, J.-X. Yin, H. Borrmann, A. Chikina, J. Denlinger, V. N. Strocov, C. Felser, S. Jia, G. Chang, and M. Z. Hasan, "Helicoid-arc van Hove singularities in topological chiral crystals", arXiv:2108.13957 (2021) (cit. on pp. 28, 81, 82).

[126] S. Suga, A. Sekiyama, and C. Tusche, "Photoelectron Spectroscopy", Springer Series in Surface Sciences **72** (2021) (cit. on pp. 29, 32, 34, 44, 60).

[127] A. Damascelli, Z. Hussain, and Z.-X. Shen, "Angle-resolved photoemission studies of the cuprate superconductors", Rev. Mod. Phys. **75**, 473 (2003) (cit. on p. 29).

[128] J. A. Sobota, Y. He, and Z.-X. Shen, "Angle-resolved photoemission studies of quantum materials", Rev. Mod. Phys. **93**, 025006 (2021) (cit. on p. 29).

[129] T. Okuda, "Recent trends in spin-resolved photoelectron spectroscopy", J. Phys.: Condens. Matter **29**, 483001 (2017) (cit. on pp. 29, 39).

[130] M. P. Seah and W. A. Dench, "Quantitative electron spectroscopy of surfaces: A standard data base for electron inelastic mean free paths in solids", Surf. Interface Anal. **1**, 2 (1979) (cit. on p. 34).

[131] B. Krömker, M. Escher, D. Funnemann, D. Hartung, H. Engelhard, and J. Kirschner, "Development of a momentum microscope for time resolved band structure imaging", Rev. Sci. Instrum. **79**, 053702 (2008) (cit. on pp. 34, 53).

[132] M. Kotsugi, W. Kuch, F. Offi, L. Chelaru, and J. Kirschner, "Microspectroscopic two-dimensional Fermi surface mapping using a photoelectron emission microscope", Rev. Sci. Instrum. **74**, 2754 (2003) (cit. on p. 37).

[133] F. Hadjarab and J. Erskine, "Image properties of the hemispherical analyzer applied to multichannel energy detection", J. Electron. Spectrosc. Relat. Phenom. **36**, 227 (1985) (cit. on p. 37).

[134] M. Escher, N. Weber, M. Merkel, C. Ziethen, P. Bernhard, G. Schönhense, S. Schmidt, F. Forster, F. Reinert, B. Krömker, and D. Funnemann, "NanoESCA: a novel energy filter for imaging x-ray photoemission spectroscopy", J. Phys.: Condens. Matter **17**, S1329 (2005) (cit. on pp. 37, 53).

[135] C. Tusche, Y.-J. Chen, C. M. Schneider, and J. Kirschner, "Imaging properties of hemispherical electrostatic energy analyzers for high resolution momentum microscopy", Ultramicroscopy **206**, 112815 (2019) (cit. on p. 38).

[136] J. Kessler, "Polarized Electrons", Springer Series on Atomic, Optical, and Plasma Physics **1** (1985) (cit. on pp. 39, 40).

[137] E. Kisker, R. Clauberg, and W. Gudat, "Electron spectrometer for spin-polarized angle-and energy-resolved photoemission from ferromagnets", Rev. Sci. Instrum. **53**, 1137 (1982) (cit. on p. 39).

[138] T. J. Gay and F. Dunning, "Mott electron polarimetry", Rev. Sci. Instrum. **63**, 1635 (1992) (cit. on p. 39).

[139] G.-C. Wang, R. J. Celotta, and D. T. Pierce, "Polarized low-energy-electron diffraction from W(100)", Phys. Rev. B **23**, 1761 (1981) (cit. on p. 39).

[140] J. Kirschner, R. Feder, and J. F. Wendelken, "Electron Spin Polarization in Energy- and Angle-Resolved Photoemission from W(001): Experiment and Theory", Phys. Rev. Lett. **47**, 614 (1981) (cit. on p. 39).

[141] F. Hillebrecht, R. Jungblut, L. Wiebusch, C. Roth, H. Rose, D. Knabben, C. Bethke, N. Weber, S. Manderla, U. Rosowski, and E. Kisker, "High-efficiency spin polarimetry by very-low-energy electron scattering from Fe(100) for spin-resolved photoemission", Rev. Sci. Instrum. **73**, 1229 (2002) (cit. on p. 39).

[142] R. Bertacco, M. Merano, and F. Ciccacci, "Spin dependent electron absorption in Fe(001)-p(1×1)O: A new candidate for a stable and efficient electron polarization analyzer", Appl. Phys. Lett. **72**, 2050 (1998) (cit. on p. 39).

[143] T. Okuda, Y. Takeichi, Y. Maeda, A. Harasawa, I. Matsuda, T. Kinoshita, and A. Kakizaki, "A new spin-polarized photoemission spectrometer with very high efficiency and energy resolution", Rev. Sci. Instrum. **79**, 123117 (2008) (cit. on p. 39).

[144] A. Winkelmann, D. Hartung, H. Engelhard, C.-T. Chiang, and J. Kirschner, "High efficiency electron spin polarization analyzer based on exchange scattering at Fe/W(001)", Rev. Sci. Instrum. **79**, 083303 (2008) (cit. on p. 39).

[145] T. Okuda, K. Miyamaoto, H. Miyahara, K. Kuroda, A. Kimura, H. Namatame, and M. Taniguchi, "Efficient spin resolved spectroscopy observation machine at Hiroshima Synchrotron Radiation Center", Rev. Sci. Instrum. **82**, 103302 (2011) (cit. on p. 39).

[146] M. Kolbe, P. Lushchyk, B. Petereit, H. J. Elmers, G. Schönhense, A. Oelsner, C. Tusche, and J. Kirschner, "Highly Efficient Multichannel Spin-Polarization Detection", Phys. Rev. Lett. **107**, 207601 (2011) (cit. on p. 39).

[147] C. Tusche, M. Ellguth, A. Ünal, C.-T. Chiang, A. Winkelmann, A. Krasyuk, M. Hahn, G. Schönhense, and J. Kirschner, "Spin resolved photoelectron microscopy using a two-dimensional spin-polarizing electron mirror", Appl. Phys. Lett. **99**, 032505 (2011) (cit. on p. 39).

[148] C. Tusche, M. Ellguth, A. Krasyuk, A. Winkelmann, D. Kutnyakhov, P. Lushchyk, K. Medjanik, G. Schönhense, and J. Kirschner, "Quantitative spin polarization analysis in photoelectron emission microscopy with an imaging spin filter", Ultramicroscopy **130**, 70 (2013) (cit. on pp. 39–42, 44).

[149] D. Kutnyakhov, P. Lushchyk, A. Fognini, D. Perriard, M. Kolbe, K. Medjanik, E. Fedchenko, S. Nepijko, H. Elmers, G. Salvatella, C. Stieger, R. Gort, T. Bähler, T. Michlmayer, Y. Acremann, A. Vaterlaus, F. Giebels, H. Gollisch, R. Feder, and G. Schönhense, "Imaging spin filter for electrons based on specular reflection from iridium (001)", Ultramicroscopy **130**, 119 (2013) (cit. on p. 39).

[150] J. Kirschner, F. Giebels, H. Gollisch, and R. Feder, "Spin-polarized electron scattering from pseudomorphic Au on Ir(001)", Phys. Rev. B **88**, 125419 (2013) (cit. on p. 39).

[151] D. Vasilyev, C. Tusche, F. Giebels, H. Gollisch, R. Feder, and J. Kirschner, "Low-energy electron reflection from Au-passivated Ir(001) for application in imaging spin-filters", J. Electron. Spectrosc. Relat. Phenom. **199**, 10 (2015) (cit. on p. 39).

[152] R. Feder, "Spin-polarised low-energy electron diffraction", J. Phys. C: Solid State Phys. **14**, 2049 (1981) (cit. on p. 41).

[153] K. Zakeri, T. Peixoto, Y. Zhang, J. Prokop, and J. Kirschner, "On the preparation of clean tungsten single crystals", Surf. Sci. **604**, L1 (2010) (cit. on p. 42).

[154] C.-H. Min, H. Bentmann, J. N. Neu, P. Eck, S. Moser, T. Figgemeier, M. Ünzelmann, K. Kissner, P. Lutz, R. J. Koch, C. Jozwiak, A. Bostwick, E. Rotenberg, R. Thomale, G. Sangiovanni, T. Siegrist, D. Di Sante, and F. Reinert, "Orbital Fingerprint of Topological Fermi Arcs in the Weyl Semimetal TaP", Phys. Rev. Lett. **122**, 116402 (2019) (cit. on pp. 45, 46, 52, 73, 98).

[155] J. Sánchez-Barriga, A. Varykhalov, J. Braun, S.-Y. Xu, N. Alidoust, O. Kornilov, J. Minár, K. Hummer, G. Springholz, G. Bauer, R. Schumann, L. V. Yashina, H. Ebert, M. Z. Hasan, and O. Rader, "Photoemission of Bi_2Se_3 with Circularly Polarized Light: Probe of Spin Polarization or Means for Spin Manipulation?", Phys. Rev. X **4**, 011046 (2014) (cit. on p. 46).

[156] Z. Xie, S. He, C. Chen, Y. Feng, H. Yi, A. Liang, L. Zhao, D. Mou, J. He, Y. Peng, X. Liu, Y. Liu, G. Liu, X. Dong, L. Yu, J. Zhang, S. Zhang, Z.-m. Wang, F. Zhang, and X. Zhou, "Orbital-selective spin texture and its manipulation in a topological insulator", Nat. Commun. **5**, 3382 (2014) (cit. on pp. 46, 73).

[157] Z.-H. Zhu, C. N. Veenstra, S. Zhdanovich, M. P. Schneider, T. Okuda, K. Miyamoto, S.-Y. Zhu, H. Namatame, M. Taniguchi, M. W. Haverkort, I. S. Elfimov, and A. Damascelli, "Photoelectron Spin-Polarization Control in the Topological Insulator Bi_2Se_3", Phys. Rev. Lett. **112**, 076802 (2014) (cit. on pp. 46, 73).

[158] H. L. Meyerheim and C. Tusche, "Atomic and Electronic Structure of the Clean and Adsorbate Covered (0001) Surface of the Topological Insulator Bi_2Se_3", Phys. Status Solidi RRL **12**, 1870337 (2018) (cit. on pp. 46, 47, 52, 72, 75).

[159] H. Zhang, C.-X. Liu, and S.-C. Zhang, "Spin-Orbital Texture in Topological Insulators", Phys. Rev. Lett. **111**, 066801 (2013) (cit. on pp. 47, 48).

[160] J. H. Dil, "Spin-and angle-resolved photoemission on topological materials", Electron. Struct. **1**, 023001 (2019) (cit. on pp. 46, 48, 73).

[161] H. Maaß, H. Bentmann, C. Seibel, C. Tusche, S. V. Eremeev, T. R. Peixoto, O. E. Tereshchenko, K. A. Kokh, E. V. Chulkov, J. Kirschner, and F. Reinert, "Spin-texture inversion in the giant Rashba semiconductor BiTeI", Nat. Commun. **7**, 11621 (2016) (cit. on p. 47).

[162] K. Kuroda, K. Yaji, M. Nakayama, A. Harasawa, Y. Ishida, S. Watanabe, C.-T. Chen, T. Kondo, F. Komori, and S. Shin, "Coherent control over three-dimensional spin polarization for the spin-orbit coupled surface state of Bi_2Se_3", Phys. Rev. B **94**, 165162 (2016) (cit. on p. 48).

[163] K. Yaji, K. Kuroda, S. Toyohisa, A. Harasawa, Y. Ishida, S. Watanabe, C. Chen, K. Kobayashi, F. Komori, and S. Shin, "Spin-dependent quantum interference in photoemission process from spin-orbit coupled states", Nat. Commun. **8**, 14588 (2017) (cit. on p. 48).

[164] Y. Cao, J. Waugh, X. Zhang, J.-W. Luo, Q. Wang, T. Reber, S. Mo, Z. Xu, A. Yang, J. Schneeloch, G. D. Gu, M. Brahlek, N. Bansal, A. Oh S.and Zunger, and D. S. Dessau, "Mapping the orbital wavefunction of the surface states in three-dimensional topological insulators", Nat. Phys. **9**, 499 (2013) (cit. on p. 48).

[165] O. Fedchenko, K. Medjanik, S. Chernov, D. Kutnyakhov, M. Ellguth, A. Oelsner, B. Schönhense, T. R. Peixoto, P. Lutz, C.-h. Min, F. Reinert, S. Däster, Y. Acremann, J. Viefhaus, W. Wurth, J. Braun, J. Minár, H. Ebert, H. Elmers, and G. Schönhense, "4D texture of circular dichroism in soft-x-ray photoemission from tungsten", New J. Phys. **21**, 013017 (2019) (cit. on pp. 48, 50).

[166] J.-H. Park, C. H. Kim, J.-W. Rhim, and J. H. Han, "Orbital Rashba effect and its detection by circular dichroism angle-resolved photoemission spectroscopy", Phys. Rev. B **85**, 195401 (2012) (cit. on pp. 50, 51, 96).

[167] Y. Liu, G. Bian, T. Miller, and T.-C. Chiang, "Visualizing Electronic Chirality and Berry Phases in Graphene Systems Using Photoemission with Circularly Polarized Light", Phys. Rev. Lett. **107**, 166803 (2011) (cit. on p. 50).

[168] M. Schüler, U. D. Giovannini, H. Hübener, A. Rubio, M. A. Sentef, and P. Werner, "Local Berry curvature signatures in dichroic angle-resolved photoelectron spectroscopy from two-dimensional materials", Sci. Adv. **6**, eaay2730 (2020) (cit. on p. 50).

[169] S. R. Park, J. Han, C. Kim, Y. Y. Koh, C. Kim, H. Lee, H. J. Choi, J. H. Han, K. D. Lee, N. J. Hur, M. Arita, K. Shimada, H. Namatame, and M. Taniguchi, "Chiral Orbital-Angular Momentum in the Surface States of Bi_2Se_3", Phys. Rev. Lett. **108**, 046805 (2012) (cit. on pp. 50, 51, 96).

[170] Y. Wang and N. Gedik, "Circular dichroism in angle-resolved photoemission spectroscopy of topological insulators", Phys. Status Solidi RRL **7**, 64 (2013) (cit. on p. 50).

[171] S. Cho, J.-H. Park, J. Hong, J. Jung, B. S. Kim, G. Han, W. Kyung, Y. Kim, S.-K. Mo, J. D. Denlinger, J. H. Shim, J. H. Han, C. Kim, and S. R. Park, "Experimental Observation of Hidden Berry Curvature in Inversion-Symmetric Bulk $2H-WSe_2$", Phys. Rev. Lett. **121**, 186401 (2018) (cit. on p. 50).

[172] S. Cho, J.-H. Park, S. Huh, J. Hong, W. Kyung, B.-G. Park, J. Denlinger, J. H. Shim, C. Kim, and S. R. Park, "Studying local Berry curvature in $2H-WSe_2$ by circular dichroism photoemission utilizing crystal mirror plane", Sci. Rep. **11**, 1684 (2021) (cit. on p. 50).

[173] M. Ünzelmann, H. Bentmann, T. Figgemeier, P. Eck, J. N. Neu, B. Geldiyev, F. Diekmann, S. Rohlf, J. Buck, M. Hoesch, M. Kalläne, K. Rossnagel, R. Thomale, T. Siegrist, G. Sangiovanni, D. D. Sante, and F. Reinert, "Momentum-space signatures of Berry flux monopoles in the Weyl semimetal TaAs", Nat. Commun. **12**, 3650 (2021) (cit. on pp. 50, 51, 74, 96–98).

[174] N. A. Cherepkov and G. Schönhense, "Linear Dichroism in Photoemission from Oriented Molecules", Europhys. Lett. **24**, 79 (1993) (cit. on pp. 51, 52).

[175] S. Chernov, K. Medjanik, C. Tusche, D. Kutnyakhov, S. Nepijko, A. Oelsner, J. Braun, J. Minár, S. Borek, H. Ebert, H. Elmers, and G. Schönhense, "Anomalous d-like surface resonances on Mo(110) analyzed by time-of-flight momentum microscopy", Ultramicroscopy **159**, 453 (2015) (cit. on p. 51).

[176] C. Wiemann, M. Patt, I. P. Krug, N. B. Weber, M. Escher, M. Merkel, and C. M. Schneider, "A new nanospectroscopy tool with synchrotron radiation: NanoESCA@ Elettra", e-J. Surf. Sci. Nanotechnol. **9**, 395 (2011) (cit. on p. 53).

[177] S. H. Vosko, L. Wilk, and M. Nusair, "Accurate spin-dependent electron liquid correlation energies for local spin density calculations: a critical analysis", Can. J. Phys. **58**, 1200 (1980) (cit. on p. 56).

[178] D. K. H. Ebert and J. Minár, "Calculating condensed matter properties using the KKR-Green's function method—recent developments and applications", Rep. Prog. Phys. **74**, 096501 (2011) (cit. on p. 56).

[179] The Jülich KKR Codes (2021) (cit. on p. 56).

[180] N. Stefanou, H. Akai, and R. Zeller, "An efficient numerical method to calculate shape truncation functions for Wigner-Seitz atomic polyhedra", Comput. Phys. Commun. **60**, 231 (1990) (cit. on p. 56).

[181] N. Stefanou and R. Zeller, "Calculation of shape-truncation functions for Voronoi polyhedra", J. Phys. : Condens. Matter **3**, 7599 (1991) (cit. on p. 56).

[182] K. Ueno and K. Fukushima, "Changes in structure and chemical composition of α-$MoTe_2$ and β-$MoTe_2$ during heating in vacuum conditions", Appl. Phys. Express **8**, 095201 (2015) (cit. on p. 65).

[183] T. Kondo, M. Ochi, M. Nakayama, H. Taniguchi, S. Akebi, K. Kuroda, M. Arita, S. Sakai, H. Namatame, M. Taniguchi, Y. Maeno, R. Arita, and S. Shin, "Orbital-Dependent Band Narrowing Revealed in an Extremely Correlated Hund's Metal Emerging on the Topmost Layer of Sr_2RuO_4", Phys. Rev. Lett. **117**, 247001 (2016) (cit. on p. 72).

[184] Y. Sun, S.-C. Wu, and B. Yan, "Topological surface states and Fermi arcs of the noncentrosymmetric Weyl semimetals TaAs, TaP, NbAs, and NbP", Phys. Rev. B **92**, 115428 (2015) (cit. on p. 73).

[185] B. Q. Lv, S. Muff, T. Qian, Z. D. Song, S. M. Nie, N. Xu, P. Richard, C. E. Matt, N. C. Plumb, L. X. Zhao, G. F. Chen, Z. Fang, X. Dai, J. H. Dil, J. Mesot, M. Shi, H. M. Weng, and H. Ding, "Observation of Fermi-Arc Spin Texture in TaAs", Phys. Rev. Lett. **115**, 217601 (2015) (cit. on p. 73).

[186] S.-Y. Xu, I. Belopolski, D. S. Sanchez, M. Neupane, G. Chang, K. Yaji, Z. Yuan, C. Zhang, K. Kuroda, G. Bian, C. Guo, H. Lu, T.-R. Chang, N. Alidoust, H. Zheng, C.-C. Lee, S.-M. Huang, C.-H. Hsu, H.-T. Jeng, A. Bansil, T. Neupert, F. Komori, T. Kondo, S. Shin, H. Lin, S. Jia, and M. Z. Hasan, "Spin Polarization and Texture of the Fermi Arcs in the Weyl Fermion Semimetal TaAs", Phys. Rev. Lett. **116**, 096801 (2016) (cit. on p. 73).

[187] B. Feng, Y.-H. Chan, Y. Feng, R.-Y. Liu, M.-Y. Chou, K. Kuroda, K. Yaji, A. Harasawa, P. Moras, A. Barinov, W. Malaeb, C. Bareille, T. Kondo, S. Shin, F. Komori, T.-C. Chiang, Y. Shi, and I. Matsuda, "Spin texture in type-II Weyl semimetal WTe_2", Phys. Rev. B **94**, 195134 (2016) (cit. on p. 73).

[188] T. Ou-Yang, G. Shu, C. Hu, and F. Chou, "Dynamic susceptibility study on the skyrmion phase stability of $Fe_{0,7}Co_{0.3}Si$", J. Appl. Phys. **117**, 123903 (2015) (cit. on p. 77).

[189] T. Ou-Yang, G. Shu, C. Hu, and F. Chou, "Preparation of Anomalous Magnetoresistance and Transport Properties of Itinerant Ferromagnet $Fe_{1-x}Co_xSi$", IEEE Trans. Magn. **51**, 1700104 (2015) (cit. on p. 77).

[190] M. Klein, D. Menzel, K. Doll, M. Neef, D. Zur, I. Jursic, J. Schoenes, and F. Reinert, "Photoemission spectroscopy across the semiconductor-to-metal transition in FeSi", New J. Phys. **11**, 023026 (2009) (cit. on p. 77).

[191] G. Castro, J. Alvarez, M. Dávila, M. Asensio, and E. Michel, "Electronic band structure of ϵ-FeSi(100)", J. Phys.: Condens. Matter **9**, 1871 (1997) (cit. on p. 77).

[192] K. Kura, K. Takano, Y. Takeichi, A. Harasawa, T. Okuda, I. Matsuda, and A. Kakizaki, "Weak electron correlation effects observed in angle-resolved photoemission spectra of MnSi (100)", J. Phys. Soc. Jpn. **77**, 024709 (2008) (cit. on p. 77).

[193] G. Castro and A. Ballesteros, "Preferential sputtering of FeSi(100) single crystal surfaces by argon, neon, and krypton ion bombardment", Surf. Sci. **204**, 415 (1988) (cit. on p. 78).

[194] Z. Rao, Q. Hu, S. Tian3, S. Gao, Z. Yuan, C. Tang, W. Fan, J. Huang, Y. Huang, L. Wang, L. Zhang, F. Li, H. Yang, H. Weng, T. Qian, J. Xu, K. Jiang, H. Lei, Y.-J. Sun, and H. Ding, "Charge instability of topological Fermi arcs in chiral crystal CoSi", arXiv:2110.07815 (2021) (cit. on p. 80).

[195] X. Zhang, Q. Liu, J.-W. Luo, A. J. Freeman, and A. Zunger, "Hidden spin polarization in inversion-symmetric bulk crystals", Nat. Phys. **10**, 387 (2014) (cit. on p. 92).

[196] W. Yao, E. Wang, H. Huang, K. Deng, M. Yan, K. Zhang, K. Miyamoto, T. Okuda, L. Li, Y. Wang, H. Gao, C. Liu, W. Duan, and S. Zhou, "Direct observation of spin-layer locking by local Rashba effect in monolayer semiconducting $PtSe_2$ film", Nat. Commun. **8**, 2033 (2017) (cit. on pp. 92, 93).

[197] J. Riley, F. Mazzola, M. Dendzik, M. Michiardi, T. Takayama, L. Bawden, C. Granerød, M. Leandersson, T. Balasubramanian, M. Hoesch, T. Kim, H. Takagi, W. Meevasana, P. Hofmann, M. S. Bahramy, J. Wells, and P. King, "Direct observation of spin-polarized bulk bands in an inversion-symmetric semiconductor", Nat. Phys. **10**, 835 (2014) (cit. on p. 93).

[198] M. Gehlmann, I. Aguilera, G. Bihlmayer, E. Młyńczak, M. Eschbach, S. Döring, P. Gospodarič, S. Cramm, B. Kardynał, L. Plucinski, S. Blügel, and C. Schneider, "Quasi 2D electronic states with high spin-polarization in centrosymmetric MoS_2 bulk crystals", Sci. Rep. **6**, 26197 (2016) (cit. on p. 93).

[199] Y. A. Bychkov and E. I. Rashba, "Oscillatory effects and the magnetic susceptibility of carriers in inversion layers", J. Phys. C: Solid State Phys. **17**, 6039 (1984) (cit. on p. 94).

[200] H. Mirhosseini, M. Flieger, and J. Henk, "Dirac-cone-like surface state in W(110): dispersion, spin texture and photoemission from first principles", New J. Phys. **15**, 033019 (2013) (cit. on p. 95).

[201] L. Kou, Y. Ma, Z. Sun, T. Heine, and C. Chen, "Two-Dimensional Topological Insulators: Progress and Prospects", J. Phys. Chem. Lett. **8**, 1905 (2017) (cit. on p. 100).

[202] B. A. Bernevig, C. Felser, and H. Beidenkopf, "Progress and prospects in magnetic topological materials", Nature **603**, 41 (2022) (cit. on p. 100).

[203] H. Hübener, M. A. Sentef, U. De Giovannini, A. F. Kemper, and A. Rubio, "Creating stable Floquet–Weyl semimetals by laser-driving of 3D Dirac materials", Nat. Commun. **8**, 13940 (2017) (cit. on p. 100).

Acknowledgement

This thesis has been done through the support of many people. First of all, I would like to express my sincere gratitude to Dr. Christian Tusche for all the support. He has guided me to the research project. I am deeply grateful to Prof. Claus Michael Schneider for giving me a great opportunity to work at PGI-6. I also learned a lot from his lecture. I gratefully thank Dr. Ying-Jiun Chen, especially for sharing her knowledge and answering my specific and detailed questions. I sincerely thank Mr. Xin Liang Tan. We spent most of the time together and he helped me a lot, especially, with experiments at Elettra and data analysis. I thank Prof. Shigemasa Suga for his advice not only for research but also for life in Germany, even since when I applied for the position here. I thank these members for their support, advice, discussion for research direction, experiments, analysis, presentation, manuscripts, and thesis.

I thank members of NanoESCA beamline, Dr. Vitaliy Feyer, Dr. Giovanni Zamborlini, Dr. Matteo Jugovac, Ms. Iulia Cojocariu, and Mr. Daniel Baranowski for their experimental support, and good time spent together in Elettra.

I thank Dr. Philipp Rüßmann for his significant contribution to the project on $NiTe_2$ and $MoTe_2$. Many important conclusions in this thesis are based on discussions with him. I thank Dr. Sergii Grytsiuk for his theoretical support and discussions on CoSi, and I would like to further advance the project. I thank Prof. Stefan Blügel for enabling me to join the close collaboration between PGI-1 and PGI-6.

I thank Mr. Kui-Hon Ou Yang, Ms. Yi-Hsin Shen, Mr. Chien Jing, and Dr. Yu-Hsu Chu for making efforts to prepare samples and performing experiments together in Elettra. I thank Dr. Raman Sankar, Dr. Yu-Hsun Chu, Dr. Guo-Jiun Shu, and Prof. Fang-Cheng Chou for providing high-quality $NiTe_2$ and CoSi samples. I thank Prof. Minn-Tsong Lin for coordinating collaboration with National Taiwan University.

I thank Prof. Keiji Ueno and his group at Saitama University for providing high-quality $MoTe_2$ samples as the collaborative project.

I thank Dr. Carsten Wiemann and Ms. Daisy Gogoi for spending daily activities together and advising my seminar and PhD thesis.

I thank Mr. Arnd Bremen, Mr. Waldemar Braun, Mr. Bernd Küpper, Mr. Norbert Schnitzler, and Mr. Heinz Pfeifer for their technical support. I thank Ms. Margret Frey for her support, especially for office work.

It is my great pleasure that I also joined research projects with internal and external collaborators.

I also thank other remembers at PGI-6 and my friends for supporting my life at FZJ and in German.

Finally, I deeply thank my parents and family for continuously supporting my PhD student life.

Band / Volume 257
High-Performance Computing Approach to Hybrid Functionals in the All-Electron DFT Code FLEUR
M. Redies (2022), xi, 109 pp
ISBN: 978-3-95806-639-7

Band / Volume 258
Establishing regulatable expression systems in the acetic acid bacterium *Gluconobacter oxydans* 621H
P. M. Fricke (2022), VIII, 187 pp
ISBN: 978-3-95806-642-7

Band / Volume 259
Density-Functional Perturbation Theory within the All-Electron Full-Potential Linearized Augmented Plane-Wave Method: Application to Phonons
C.-R. Gerhorst (2022), xvi, 317 pp
ISBN: 978-3-95806-649-6

Band / Volume 260
Crystal and Magnetic Structure of CrAs under Extreme Conditions
A. Eich (2022), viii, 235 pp
ISBN: 978-3-95806-655-7

Band / Volume 261
Applications of transcription factor-based biosensors for strain development and evolutionary engineering
R. G. Stella (2022), x, 128 pp
ISBN: 978-3-95806-657-1

Band / Volume 262
Strömungsmechanische Simulation und experimentelle Validierung des kryogenen Wasserstoff-Moderators für die Europäische Spallationsneutronenquelle ESS
Y. Beßler (2022), XXIV, 154, xxxiii pp
ISBN: 978-3-95806-660-1

Band / Volume 263
9th Georgian-German School and Workshop in Basic Science September 12 – 16, 2022 | Kutaisi, Tbilisi | Georgia
A. Kacharava, E. Portius, N. J. Shah, H. Ströher (2022)
ISBN: 978-3-95806-664-9

Band / Volume 264
Self-assembly of Au-Fe_3O_4 dumbbell nanoparticles
N. Nandakumaran (2022), xiv, 234 pp
ISBN: 978-3-95806-666-3

Band / Volume 265
Time-resolved and three-dimensional characterisation of magnetic states in nanoscale materials in the transmission electron microscope
T. Weßels (2023), xx, 211 pp
ISBN: 978-3-95806-685-4

Band / Volume 266
Dissecting iron and heme regulatory networks and adaptation to heme stress in *Corynebacterium glutamicum*
A. Krüger (2023), IV, 274 pp
ISBN: 978-3-95806-686-1

Band / Volume 267
Morphological and functional characterization of layer 5 neurons in rat medial prefrontal cortex, their synaptic microcircuitry and serotonin modulation
R. Rama (2023), 116 pp
ISBN: 978-3-95806-688-5

Band / Volume 268
Magnetic and transport studies of the parent and Fe doped Hexagonal-Mn_3Ge Weyl semimetal
V. Rai (2023), xviii, 156 pp
ISBN: 978-3-95806-695-3

Band / Volume 269
The complex inositol metabolism of *Corynebacterium glutamicum* and its application for the production of rare inositols
P. Ramp (2023), VI, 161 pp
ISBN: 978-3-95806-699-1

Band / Volume 270
Spin- and orbital-dependent band structure of unconventional topological semimetals
K. Hagiwara (2023), v, 115 pp
ISBN: 978-3-95806-701-1

Weitere ***Schriften des Verlags im Forschungszentrum Jülich*** unter
http://wwwzb1.fz-juelich.de/verlagextern1/index.asp

Schlüsseltechnologien / Key Technologies
Band / Volume 270
ISBN 978-3-95806-701-1

Mitglied der Helmholtz-Gemeinschaft

JÜLICH
Forschungszentrum